

UTRECHT UNIVERSITY

GRADUATE SCHOOL OF NATURAL SCIENCES

INSTITUTE FOR THEORETICAL PHYSICS

---

# Probing Ultralight Bosons around Black Holes with Numerical Relativity

---

Alexandra WERNERSSON

September 2020-July 2021

MASTER'S THESIS

UNDER THE SUPERVISION OF

Dr. Tanja HINDERER



Utrecht University





## Abstract

One of the greatest mysteries of our current understanding of the Universe is the nature of dark matter. There are several dark matter candidates of various masses but a prominent type of dark matter is *axion dark matter*. In this thesis we study a type of axion dark matter known as *Ultralight Bosons* with numerical relativity. These particles are thought to form clouds around black holes through the *superradiance process*. The main novelty of this thesis is that we may investigate the effects of clouds of ultralight bosons around black holes numerically in a regime unexplored by perturbative methods. For our numerical setup we utilize a C++ library called *KADATH* to solve the initial value problem in the XCTS approach. We perform a variety of tests of the code robustness and solve numerical degeneracy problems at the black hole horizon. Finally, we obtain results of the free bosonic field profile around the black hole. Furthermore, we obtain results of new physical effects from the inclusion of self-interactions and backreaction.

# Acknowledgements

First and foremost, I would like to thank my supervisor Dr. Tanja Hinderer for presenting me with the opportunity to work on this interesting project. Her knowledge and creative input have pushed the project forward and her support within and outside of the project has been great help.

Secondly, I would like to thank my collaborators Christoffel Doorman and Dr. Horng Sheng Chia. Christoffel, with his numerical expertise and ambition for the project he has aided me several times during the progress of our work. Horng Sheng, with his deep knowledge of theoretical physics and high work moral he has inspired us to consider interesting physical effects of boson clouds and presented us with the correct physical interpretation of our results.

Lastly, I would like to acknowledge Dr. Umut Gursoy and thank him for reading my thesis and for inspiring me to add a section on axions in string theory.

# Contents

<b>Introduction</b>	<b>5</b>
<b>1 Ultralight bosons</b>	<b>7</b>
1.1 The existence of Ultralight Bosons	7
1.2 Superradiance	9
1.3 Gravitational atoms and their energy spectra	10
1.3.1 Energy spectra of gravitational atoms	12
1.4 Self-interacting scalar fields	13
1.4.1 Bosonova - a non-perturbative effect	14
1.5 Superradiance in a binary system	15
1.5.1 Gravitational perturbations	15
1.6 Gravitational wave signatures	16
1.6.1 Annihilation	16
1.6.2 Signals in the binary	17
1.6.3 The role of numerical relativity	20
<b>2 Equations in the 3+1 formalism</b>	<b>21</b>
2.1 History of the Hamiltonian formalism	21
2.2 Geometry of spacetime	22
2.3 Foliation kinematics	24
2.3.1 Coordinate adaption to the foliation	26
2.4 A introduction to General Relativity	28
2.5 The 3+1 formalism	29
2.5.1 Decomposition of the energy-momentum tensor	30
2.5.2 Projection of the Einstein equation	30
2.6 Scalar field equations in the 3+1 formalism	33
2.6.1 Stationary solution	33
2.6.2 The energy-momentum tensor	34
2.7 The initial data problem	35
2.7.1 Conformal decomposition of the constraints	35
2.7.2 Conformal decomposition of the constraint equations	36
2.7.3 Conformal decomposition of the Klein-Gordon equations	37
2.8 The extended conformal thin sandwich (XCTS)	38
2.8.1 XCTS approach to a static black hole	39

<i>CONTENTS</i>	4
2.9 An introduction to black holes in General Relativity . . . . .	39
2.10 Gauge invariant quantities . . . . .	43
<b>3 Kadath</b>	<b>44</b>
3.1 Spectral methods . . . . .	44
3.2 An introduction to <b>KADATH</b> . . . . .	45
<b>4 Numerical results</b>	<b>49</b>
4.1 Numerical setup . . . . .	49
4.2 Initial obstacles . . . . .	50
4.2.1 Degeneracy problems at the horizon . . . . .	50
4.2.2 A resolution study . . . . .	51
4.3 Bosonic field profile for a non-interacting scalar field . . . . .	52
4.3.1 Sensitivity to changes in the eigenfrequency . . . . .	52
4.4 Boson field with self-interactions . . . . .	53
4.5 Preliminary results of the backreaction . . . . .	55
4.5.1 Results step 1: Solving for the background . . . . .	56
4.5.2 Results step 2: Solving for the field . . . . .	58
4.6 Preliminary results of backreaction with a self-interacting field . . . . .	59
<b>5 Conclusions</b>	<b>61</b>
<b>Appendices</b>	<b>63</b>
<b>A Appendix A</b>	<b>64</b>
A.0.1 Conformal decomposition of various quantities . . . . .	65
A.0.2 Lie derivatives . . . . .	65
<b>B Appendix B</b>	<b>66</b>
B.1 Scalar field equations . . . . .	66
B.2 Background . . . . .	66
B.3 Imaginary fields . . . . .	67
B.3.1 Matter equations . . . . .	67
<b>C Appendix C</b>	<b>69</b>
<b>D Appendix D</b>	<b>80</b>
<b>E Appendix E</b>	<b>82</b>



# Introduction

The Standard Model of particle physics have provided great insights of how all known particles and forces of nature interact, with the exception of gravity. It has successfully explained experimental results and predicted a wide variety of physical phenomena. However, even if it is currently the best description of the subatomic world it is also incomplete. The Standard Model does not explain several pieces of evidence of new physics. A particular strong evidence of new physics beyond the Standard Model is the existence of *dark matter*. Dark matter makes up most of the matter density in the universe but little is known about it. Therefore, studying different types of dark matter candidates is an attractive topic to this day. A particularly well-motivated dark matter candidate is *axion dark matter*. The axion is a hypothetical particle that arises in several extensions of the Standard Model. Furthermore, a plethora of ultralight axions and axion-like-particles (ALPs) have also been shown to arise in compactifications of extra spatial dimensions in string theory [4]. A key feature of Axions and ALPs is that they interact very weakly or not at all with the other known forces in the Standard Model. Therefore, they are often referred to as belonging to a *dark sector* which cannot be probed by usual particle collider experiments. In order to detect new types of dark matter we must think creatively and explore other types of colliders that may aid in the detection of more elusive dark matter candidates.

A new way to detect dark matter is found in an energy extracting process presented by Zel'dovich in 1971. The idea is that a rotating object such as a cylinder with rotational velocity of  $\Omega$  will amplify an incoming wave with frequency  $\omega$ . The requirement for this amplification process is that the instability  $\frac{\omega}{m} < \Omega$  is satisfied. The incoming wave will extract the rotational energy from the rotating object until the instability is saturated. The process from Zel'dovich was coined *superradiance*. Superradiance is thought to occur in nature around rotating black holes for bosons of any spin such as photons and gravitons. In particular, it is thought to occur for ultralight axion particles with mass of  $\mu \in \{10^{-20}, 10^{-10}\}$  eV. For these values of  $\mu$  the superradiance process will amplify the field and create a boson cloud around the black hole.

On the 14th of September 2015 a new era of multimessenger astronomy was born. LIGO made the first observation in history of gravitational waves and with it a new window into the universe was opened. Gravitational waves are often referred to as 'ripples in spacetime'. The waves travel undisturbed through spacetime and carry vital information about the energetic events from which they emerged. So far, LIGO has only been able to detect binary mergers of BH-BH, NS-NS and recently BH-NS [6]-[7]. However, there are other types of gravitational



waves that has yet to be discovered. One type is *continuous gravitational waves* (CGW). CGW are thought to be produced by massive spinning objects such as neutron stars. Any type of bumps or imperfections in the spherical shape of the star will generate continuous gravitational waves of the same frequency and amplitude [8]. Continuous waves are yet to be discovered and interestingly the aforementioned boson cloud is another source of CGWs. Annihilations of bosons and level transitions which naturally occurs in the cloud are two sources of continuous gravitational waves. The search for the CGW is another interesting property of boson cloud around single black holes. From the LIGO O2 data, a small constraint on the boson mass has already been provided [9].

Although boson clouds around single black holes are interesting in their own regard, a natural question to ask is: What happens in a binary in which one black hole components is hosting a cloud? It turns out that a binary companion will greatly increase the dynamics and observational impact of the cloud [11]. However, the validity of the perturbative approximation broke down at the most interesting regime. In order to fully understand and predict the phenomena of boson clouds around black holes, one must solve the fully non-perturbative Einstein equations and scalar field equations, which is only possible in numerical relativity.

In this thesis we aim to go beyond the perturbative limitations and study the effects of boson clouds around black holes in a completely unexplored regime. Furthermore, we are interested in the new physical effects provided by self-interactions and backreaction. To this end we utilize the 3+1 decomposition of Einstein's equation and scalar field equations which have been derived in [38]. As the name suggest, the 3+1 formalism splits spacetime into three-dimensional spatial slices that evolve forward in the one-dimensional time direction. The problem reduces to an initial data problem which we solve in the XCTS approach. To this end, we utilize an open source C++ library called KADATH.

The work done in this thesis is part of an ongoing project. Some of the results presented will be finalized after the deadline of the thesis has passed. Numerical subtleties and possible future directions will be discussed in the final chapters.

# Chapter 1

## Ultralight bosons

In this chapter I will introduce the concept of axions and axion-like-particles from beyond the standard model theories. In particular, I will focus on a type of dark matter known as *ultralight bosons*. In section 1.2 I will explain in more detail how this type of dark matter may form clouds around black holes through the superradiance process. The resulting system of a black hole with a boson cloud is often referred to as a *gravitational atom* to which section 1.3 is dedicated to. Throughout the chapter I will discuss the energy spectra and properties of gravitational atoms for both single and binary black holes. In section ?? and ?? I will review the current and future observational prospects of boson clouds around black holes.

### 1.1 The existence of Ultralight Bosons

It is not only dark matter that the Standard Model has yet to explain. A famous problem which has been known since the early days of quantum chromodynamics (QCD) is the strong CP-problem. The CP problem emerges by realizing that one can add a CP violating interaction term to the QCD action

$$S_\theta = \frac{\theta}{32\pi^2} \int d^4x \epsilon^{\mu\nu\lambda\rho} \text{Tr} G_{\mu\nu} G_{\lambda\rho}. \quad (1.1)$$

Where  $\theta$  is the coupling parameter that multiplies the QCD instanton number. The instanton<sup>1</sup> number is an integer implying that  $\theta$  is an angular parameter. For fermions, the actual physical parameter is denoted as  $\bar{\theta}$ , which is the sum of  $\theta$  and the overall phases of the quark mass matrix

$$\bar{\theta} = \theta + \arg \det m_q. \quad (1.2)$$

$\bar{\theta}$  is constrained by the neutron electric dipole moment which has an experimental limit of  $d_n < 2.9 \times 10^{-22} e \text{ cm}$  [10]. This limit puts a stringent bound on  $\bar{\theta}$  to be tiny  $|\bar{\theta}| \lesssim 10^{-10}$ . The CP problem is the inability of the Standard Model to explain the seemingly unnatural tininess of  $\bar{\theta}$ . The CP problem, similar to its famous cousins - The cosmological constant, the mass hierarchy problem, etc - require extreme fine-tuning of  $\theta$  and  $\arg \det m_q$  to produce the tiny  $\bar{\theta}$  required from observations. However, unlike the cosmological constant and mass hierarchy problem,  $\bar{\theta}$  being small is not a requirement for the existence of life. As a consequence, the

---

<sup>1</sup>An instanton is a classical solution to equations of motion with a finite, non-zero action [3].

smallness of  $\bar{\theta}$  encourages a new dynamical mechanism.

An attractive solution to the CP problem emerges from the *Peccei-Quinn theory*, postulated in 1977. From the PQ theory a hypothetical elementary particle known as the *QCD axion* arises. The QCD axion,  $\phi_a$ , is directly related to the aforementioned QCD action which now reads

$$S_\theta = \frac{1}{32\pi^2 f_a} \int d^4x \phi_a^{\mu\nu\lambda\rho} \text{Tr} G_{\mu\nu} G_{\lambda\rho}. \quad (1.3)$$

At the classical level  $S_\theta$  is invariant under the *Peccei-Quinn symmetry*,  $\phi_a \rightarrow \phi_a + \text{const}$ . Therefore, the QCD axion is the Nambu-Goldstone boson that arises as a result of a spontaneous global symmetry breaking. However, QCD instanton effects will lead to an explicit symmetry breaking, generating a periodic potential for the axion. Consequently, the axion vacuum expectation value (vev) adjusts itself such that  $\bar{\theta}$  is cancelled. Thereby solving the CP problem. Many of the axions properties are determined by the size of the symmetry breaking scale,  $f_a$ <sup>2</sup>. Notably, the mass that the QCD axion acquires as a result of the symmetry breaking

$$m_a \approx 6 \cdot 10^{-10} \text{eV} \left( \frac{10^{16} \text{GeV}}{f_a} \right). \quad (1.4)$$

Values of  $f_a$  have been constrained from laboratory searches and astrophysical demands[12]. If  $f_a$  is below  $10^9$  GeV then the axion would couple too strongly and too many axions would be produced in astrophysical environments, red giants would be cooled too rapidly for example [5]. Furthermore, if  $f_a$  is too large ( $f_a \gg 10^{12}$  GeV) i.e. if the axion coupling is too weak then too much axion dark matter is created in the early universe relative to what is visible today. In fact, the high symmetry breaking scale ensures that the Compton wavelength of the axion matches the size of stellar mass black holes. Therefore, the axions may affect their dynamics making black holes observations an attractive probe of the axion's parameter space [3].

Although the axion provides a dynamical solution to the strong CP problem, at the effective field theory level it does not seem as natural to have a "fake" global PQ symmetry that is only broken explicitly by QCD effects. Therefore, it is only reasonable to ask if axions arise naturally in the most developed quantum theory of gravity - string theory [5].

## Axions in String Theory

Pseudoscalar fields with axion-like properties arise generically in string theory compactifications<sup>3</sup>. Comprehensive reviews of how axions emerge in string theory compactifications can be found in [3]-[5], [12]<sup>4</sup>. The string theory compactification produces a plethora of light axions often referred to in literature as the *axiverse*. These axions are characterized by their mass  $\mu$  and decay constant  $f_a$ . Unlike the QCD axion,  $\mu$  and  $f_a$  are not related via (1.4). Therefore, some axions in string theory are referred to as axion-like particles (ALPs) whose masses are less constrained and independent of their couplings to other particles [2]. Both axions and

<sup>2</sup>Analogous to how low energy pion interactions are determined by the pion decay constant  $f_\pi$ .

<sup>3</sup>Compactification is the act of linking the higher dimensions in string theory to our four dimensional physical world.

<sup>4</sup>This thesis will not focus on string theory and I only review their properties here.

axion-like particles are promising dark matter candidates whose masses and decay constants are constrained from astrophysics and experimental results as discussed earlier. A popular type of ALPs are *Ultralight bosons*. These bosons only interact gravitationally and their masses are constrained from *black hole superradiance*. For ultralight bosons whose mass is in the range of  $\mu \in [10^{-20}, 10^{-10}]$  eV, their Compton wavelength will be of the size of astrophysical length scales and may trigger instabilities around black holes [13]. These instabilities have the potential of producing observational signatures in current and future gravitational wave detectors. In the sections below I will explain the process of forming boson condensates around black holes from superradiance, their properties and potential gravitational wave signatures [11].

## 1.2 Superradiance

In 1969 Penrose proposed a method on how to extract energy from a rotating black hole. The method is known as the *Penrose process* and is a simple idea: A person armed with a large rock starts outside of the ergosphere<sup>5</sup> of a black hole. When the (person+rock) system leaps towards the black hole and enters the ergosphere a clever method can be used. The person uses the law of conservation of momentum and throws the rock into the black hole. Penrose showed that the person is able to follow a trajectory and emerge out of the ergosphere with more energy than they entered with. The energy gained has been extracted from the black hole by decreasing its angular momentum<sup>6</sup>.

In 1971 Yakov Zel'dovich realized that a cylinder, made of absorbing material and rotating about its axis, had the potential of amplifying the modes of scalar or electromagnetic radiation that approached it, provided that the following condition is fulfilled:

$$\omega < m\Omega. \tag{1.5}$$

Where  $\omega$  is the frequency of the incoming wave,  $m$  is the azimuthal quantum number and  $\Omega$  is the rotational frequency of the cylinder. Zel'dovich later realized that when allowing for quantum physics, there may also be spontaneous emission in the (1.5) regime and concluded that a spinning(Kerr) black hole could show both amplification and spontaneous emission provided (1.5) is satisfied. The outgoing waves will then have increased their amplitude, thereby extracting energy in the spirit of the Penrose process [3].

### Black hole superradiance

Black hole superradiance is a phenomenon thought to occur in nature and has attracted more attention since the gravitational wave discovery in 2015. In this section we shall outline the most important relations and properties of this process.

---

<sup>5</sup>The *ergosphere* of a spinning black hole is defined as the region between the stationary limit surface and outer event horizon through which it is possible to enter and leave but not stay stationary, see [17] p.264

<sup>6</sup>For a more detailed review see [17] and Section 2.9.

Consider a black hole of mass,  $M$  and spin  $J = aM$ , with a bosonic field and frequency  $\omega$ . From (1.5) we obtain the instability condition:

$$\boxed{\frac{\omega}{m} < \Omega_H = \frac{a}{2Mr_+}}, \quad (1.6)$$

where  $r_+$  is the size of the event horizon. As long as (1.6) is fulfilled, bosons of any mass and spin may trigger black hole superradiance. The mass however, plays the crucial role of a *reflecting barrier* from which the bosonic wave can be reflected back to the black hole and extract energy from it continuously. Energy proceeds to be extracted and the black hole's spin and mass are reduced until the instability (1.6) is saturated. The final state is an Einstein-Bose condensate of ultralight bosons, gravitationally bounded to the black hole which has obtained a significantly lower spin and mass. <sup>7</sup>

**Note:** Regarding the spin of the boson, focus is aimed at scalar bosons for two reasons. 1) Unlike for vector and tensor fields, the Kerr metric is separable in Boyer-Lindquist coordinates for the scalar case. 2) Ultralight scalar bosons arise naturally from several extensions of the standard model and the Kerr-Scalar system thereby becomes particularly motivated [11].

### 1.3 Gravitational atoms and their energy spectra

As stated in the previous section the black hole may obtain a cloud of ultralight bosons gravitationally bound to it if the instability condition (1.6) is fulfilled. The configuration of a black hole with a boson cloud is in fact known as a *gravitational atom* to which this section is dedicated to.

The Klein-Gordon equation for a scalar field  $\Psi(t, \mathbf{r})$  with mass  $\mu$  in a Kerr background is given by,

$$(g^{\alpha\beta} \nabla_\alpha \nabla_\beta - \mu^2) \Psi = 0, \quad (1.7)$$

where  $g^{\alpha\beta}$  is the Kerr metric and  $\nabla_a$  the corresponding co-variant derivative. As will soon become evident, the solutions of (1.7) are remarkably similar to that of an hydrogen atom. Therefore, we preset the following ansatz of a complex scalar field,

$$\Psi(t, \mathbf{r}) = \frac{1}{\sqrt{2\mu}} \psi(t, \mathbf{r}) e^{-i\mu t}. \quad (1.8)$$

Inserting this ansatz in (1.7) and only keeping leading terms in  $r^{-1}$  leads to a Schrödinger like equation [15]

$$i \frac{\partial}{\partial t} \psi(t, \mathbf{r}) = \left( -\frac{1}{2\mu} \nabla^2 - \frac{\alpha}{r} \right) \psi(t, \mathbf{r}). \quad (1.9)$$

In the above equation we have introduced the key-parameter  $\alpha$  defined as

$$\boxed{\alpha \equiv \frac{GM\mu}{\hbar c} \approx 0.002 \left( \frac{M}{3M_\odot} \right) \left( \frac{\mu}{10^{-12} \text{eV}} \right)}. \quad (1.10)$$

<sup>7</sup>This is often referred to as the 'black hole bomb' in literature [14].

Note that  $\alpha$  is in fact defined as the ratio of the gravitational radius of black hole,  $r_g \equiv GM/r^2$  and the reduced Compton wavelength of the scalar field,  $\lambda_c = \hbar/(\mu c)$ .  $\alpha$  is the key parameter governing the superradiance process. As will become evident, it serves a similar role as the fine-structure constant in QED. In the sense that  $\alpha$  defines the cloud's energy spectra, size and other properties.

As noted above, (1.9) has the same form as the Schrödinger equation for a hydrogen atom. Therefore, the bound-state solutions for a scalar cloud can be given by the principal quantum numbers  $\{n, l, m\}$ .  $n$  is the energy level,  $l$  is the orbital quantum number and  $m$  the azimuthal angular momentum quantum number. The stationary eigenstates for the cloud are given by the hydrogenic eigenfunctions,

$$\psi_{nml}(t, \mathbf{r}) \approx e^{-i(\omega - \mu)t} \bar{R}_{nl}(r) Y_{lm}(\theta, \phi). \quad (1.11)$$

The occupied states are what we refer to as 'clouds' whose eigenfrequencies are given by

$$\omega_{nml} \equiv E + i\Gamma \equiv \mu \sqrt{1 - \frac{\alpha^2}{\nu^2}}. \quad (1.12)$$

Here,  $E$  corresponds to the energy and the imaginary part to the instability rates  $\Gamma$ . At leading order, the real part of  $\nu$  is replaced by the energy level number  $n$ . Therefore, the eigenfrequency can be approximated at leading order to

$$\omega_{nlm} \approx \mu \left( 1 - \frac{\alpha^2}{2n^2} \right). \quad (1.13)$$

Furthermore, for  $\alpha \ll 1$  the instability rate  $\Gamma$  can be approximated through a formula known as 'Detweiler's approximation'

$$\Gamma_{nml} = \frac{2r_+}{M} C_{nml}(\alpha) (m\Omega_H - \omega) \alpha^{4l+m}, \quad (1.14)$$

where

$$C_{nml}(\alpha) = \frac{2^{4l+1}(n+l)}{n^{2l+1}(n-l-1)!} \left[ \frac{l!}{(2l)!(2l+1)!} \right] \prod_{j=1}^l [j^2(1 - \tilde{a}^2) + (\tilde{a}m - 2\tilde{r}_+\alpha)^2] \quad (1.15)$$

where the  $\tilde{a}, \tilde{r}_+$  are the rescalings  $\tilde{a} = a/M$  and  $\tilde{r}_+ = r_+/M$ . Despite (1.14) was obtained for  $\alpha \ll 1$  it has been shown to work reasonably in comparison to numerical results for  $\alpha < 0.5$ , see Fig. 28 in [42].

$\Gamma_{nml}$  is strongly dependent on the angular quantum number  $l$  meaning that the fastest growing modes have  $l = m = 1$ . In practice the fastest growing mode is |211), the 2p state, which is considered to be the initial condition of the cloud.

### 1.3.1 Energy spectra of gravitational atoms

Because the solutions of the scalar field can be written in terms of the hydrogenic wavefunctions (1.11) the configuration of a black hole hosting a cloud is known as a gravitational atom. We will now go over the energy spectra for the gravitational atom. Firstly, we need to turn our attention to the Klein-Gordon equation. For the radial part of the Klein-Gordon equation, (1.7), the solutions we are looking for are *quasi-bound state solutions*, in other words, purely in-going at the horizon and vanishing at infinity,

$$R \propto \begin{cases} (r - r_+)^{iP_+}, & \text{as } r \rightarrow r_+ \\ \exp(-\sqrt{1 - \omega^2}r), & \text{as } r \rightarrow \infty, \end{cases}$$

where  $P_{\pm} = \frac{\alpha(\bar{a}m - 2r_{\pm}\omega)}{r_+ - r_-}$ . This is in fact an eigenvalue problem meaning that the inner and outer boundary conditions can only be solved for specific values of the eigenfrequency  $\omega$ . Unfortunately, closed-form solutions for  $\omega$  doesn't exist. The approximation (1.13) is only valid in the perturbative regime in which  $\alpha \ll 1$ .

In fact the equation of motion for the radial function turns out to be similar to the time-independent Schrödinger equation for a Hydrogen atom.

$$\left[ -\frac{1}{2r^2} \frac{d}{dr} \left( r^2 \frac{d}{dr} \right) - \frac{\alpha}{r} + \frac{l(l+1)}{2r^2} + \frac{1 - \omega^2}{2} \right] R_0^{\text{far}} = 0 \quad (1.16)$$

In (1.16) the first term corresponds to the kinetic energy, the  $1/r$  is analogous to the Coulomb potential with the gravitational coupling constant  $\alpha$ , the  $1/r^2$  term is the centri-fugal barrier with the orbital angular momentum number  $l$ . Lastly, the final term illustrates the exponential behaviour of the quasi-bound states as  $r \rightarrow \infty$ . Due to the resemblance of the Hydrogen case one expects the energy spectrum of all modes to be Bohr-like. We therefore consider the radial wavefunction solutions for the Bohr case below:

$$R_{nl}(r) = \sqrt{\left(\frac{2}{na_0}\right)^3 \frac{(n-l-1)!}{2n(n+l)!}} e^{-\frac{r}{na_0}} \left(\frac{2r}{na_0}\right)^l L_{n-l-1}^{2l+1}\left(\frac{2r}{na_0}\right) \quad (1.17)$$

where the  $L_{n-l-1}^{2l+1}$  are the associated *Laguerre polynomials* defined as:

$$L_n^k = \frac{e^x x^{-k}}{n!} \frac{d^n}{dx^n} (e^{-x} x^{n+k}) \quad (1.18)$$

For a 1s state we have the quantum numbers  $\{n, l, m\} = \{1, 0, 0\}$ . From (1.17) we get:

$$R_{1s} = \sqrt{\left(\frac{2}{a_0}\right)^3 \frac{0!}{2!}} e^{-\frac{r}{a_0}} \left(\frac{2r}{a_0}\right)^0 L_0^1\left(\frac{2r}{a_0}\right) = \frac{2}{\sqrt{a_0}} e^{-\frac{r}{a_0}}. \quad (1.19)$$

In the same way we obtain the 2p state from the quantum numbers  $\{n, l, m\} = \{2, 1, 1\}$

$$R_{2p} = \sqrt{\left(\frac{2}{2a_0}\right)^3 \frac{0!}{2!}} e^{-\frac{r}{2a_0}} \left(\frac{r}{a_0}\right)^1 L_0^3\left(\frac{r}{a_0}\right) = \frac{1}{\sqrt{2a_0}} \frac{2r}{a_0} e^{-\frac{r}{2a_0}}. \quad (1.20)$$

One may of course push this analysis to higher orders in  $\alpha$  and uncover a large part of the energy spectrum which can be illustrated as in Figure (1.1) [15].

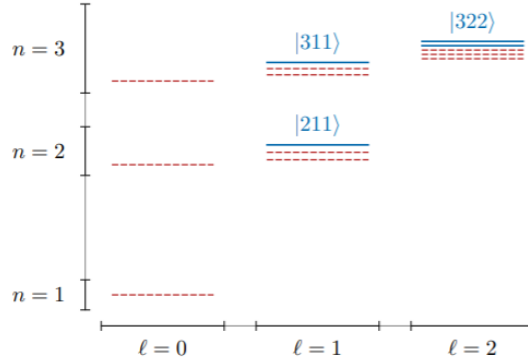


**Figure 1.1:** An illustration of the energy spectrum for states denoted as  $|nlm\rangle$ [15].

## 1.4 Self-interacting scalar fields

It is well-motivated by theory that the scalar fields considered possess self-interactions [21]. The Lagrangian for a self-interacting scalar field with a quartic coupling  $\lambda$  on a fixed background is given by

$$\mathcal{L} = -\frac{1}{2}(D_\mu\varphi)(D^\mu\varphi) - \frac{1}{2}\mu^2\varphi^2 + \frac{1}{4!}\lambda\varphi^4. \quad (1.21)$$

A quartic interaction is the simplest non-gravitational interaction for a scalar particle and motivated for axions due to the periodic potential that emerges from the symmetry breaking, see section 1. The strength of the interaction may have different sign depending on whether the interaction is attractive:  $\lambda > 0$  or negative:  $\lambda < 0$ . From (4.4) we obtain the equation of motion

$$(D^2 - \mu^2)\varphi = -\frac{\lambda}{6}\varphi^3 \quad (1.22)$$

For small enough couplings, self-interaction effects are negligible and the superradiance evolves as in a purely gravitational case. However, the large field amplitude as a result of superradiance may compensate for  $\lambda$  since the occupation number  $N$  can reach exponentially large values. In this case the quartic self-interaction may alter the dynamics of superradiance significantly. There are three possible scenarios to lose energy with the inclusion of quartic self-interactions namely,

- A Relativistic scalar emission
- B Non-relativistic scalar emission
- C Bound state interactions

As an example, I discuss the first one below.



### Relativistic emission of the hydrogenic levels

As mentioned previously, the  $l = 1$  (2p state) is expected to be the fastest growing mode. Generally speaking, it is the non-relativistic, hydrogenic wavefunctions that will dominate the evolution of the superradiance. Therefore, it is convenient to introduce a non-relativistic reduction,

$$\varphi = \frac{1}{\sqrt{2\mu}}(\psi e^{-i\mu t} + \text{c.c}). \quad (1.23)$$

Where  $\psi$  is a complex scalar field whose norm is the occupation number  $N \approx \int dV |\psi|^2$ . (1.23) aids in creating a visual representation for the  $\lambda$ -induced interactions. Consider the terms of

$$\frac{\lambda}{4!} \varphi^4 = \frac{\lambda}{96\mu^2} (\psi e^{-i\mu t} + \psi^* e^{-i\mu t})^4 \quad (1.24)$$

If the complex field  $\psi = \sum \alpha_i \psi_i$  is expanded in some basis  $\{\psi_i\}$ , one can draw a Feynman diagram in which the  $\psi_i$  corresponds to legs on the left-hand side and  $\psi_i^*$  to the legs on the right-hand-side of the diagram. As an example, the hydrogenic  $|211\rangle$  level will source a relativistic emission corresponding to the diagram in Fig. 2.4 Because of the fact that the relevant

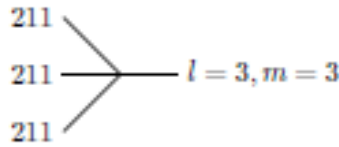


**Figure 1.2:** A relativistic emission of the hydrogenic  $|211\rangle$  level [21].

terms in the Lagrangian correspond to the ones involving  $\psi_{211}^3$ , which source an  $l = m = 3$  relativistic mode [21].

**Note:** As the cloud grows, the gravitational wave signals from axion annihilation increases and reaches a maximum as the superradiant instability condition is saturated. Thereafter, the  $l = 2$  level starts populating but at a slower rate. With self-interactions included, this does not occur immediately [21].

#### 1.4.1 Bosenova - a non-perturbative effect

In the previous section, the scalar field is assumed to be well-approximated by the combination of hydrogenic bound states and a quartic self-interaction which leads to slow transfers of energy between these bound states. However, for large enough field amplitudes this image breaks down. Furthermore, for large field amplitudes and attractive interactions, the hydrogenic state would become unstable and collapse in a *bosenova*.

As the superradiance progress, the number of axions increases and thereby the effect of attractive self-interactions. At this point the shape of the cloud changes and is no longer described by the unperturbed hydrogenic wavefunctions. A dramatic effect occurs if the size of the cloud keeps growing, which is what is known as the *Bosenova*. The effect was experimentally observed in a trapped Bose-Einstein condensate with attractive self-interactions. As the mass

of the cloud reaches beyond some critical value, the quantum pressure of the axion field will be smaller than the attractive force of the cloud's self-interaction and thereby collapses. The energy of a static cloud has the following dependence on its size  $r$ ,

$$V(R) \approx N \frac{l(l+1)+1}{2\mu_a r^2} - N \frac{\alpha}{r} + \frac{N^2}{32\pi f_a^2 r^3}. \quad (1.25)$$

It is evident that for large occupation numbers  $N$ , the last term will dominate over the repulsion term due to quantum pressure and the cloud will collapse.

## 1.5 Superradiance in a binary system

The case of a boson cloud around a single black hole has been studied in various papers. Even more interesting phenomena is thought to occur in a binary system of two black holes, where one of the BHs is endowed with a boson cloud. This is the kind of system we turn to next.

### 1.5.1 Gravitational perturbations

The inclusion of a binary black hole companion will naturally cause a gravitational perturbation,  $\delta g_{\mu\nu}$ , to our previously unperturbed Kerr metric  $g^{(0)}$  resulting in a new metric  $g_{\mu\nu} = g_{\mu\nu}^{(0)} + \delta g_{\mu\nu}$ . The metric perturbation  $\delta g_{\mu\nu}$  arises from two sources: 1) The contribution to the gravitational potential from the mass,  $M_*$ , of the companion. 2) The response of the black hole+cloud to tidal deformations. Aside from gravitational perturbations to the metric, a binary companion may also induce *mass transfer* between the cloud and companion. This occurs when the characteristic Bohr radius,  $r_c$ , becomes larger than the Lagrange point  $L_1$ <sup>8</sup> of the two objects. The surface which has the same gravitational potential as  $L_1$  is called the *Roche lobe* [11]. **MAybe not the best ending of a section**

### Level mixings

An important consequence of the companion's gravitational perturbation is *level mixings*. In other words, there will exist an overlap between the modes  $|\psi_i\rangle = |n_i l_i m_i\rangle$  and  $|\psi_j\rangle = |n_j l_j m_j\rangle$ , where the full wavefunction of the cloud is written as  $|\psi_i\rangle = \sum_i c_i(t) |\psi_i\rangle$ .<sup>9</sup> With the inclusion of a companion that generates an additional gravitational potential,  $V_*$ ,

$$V_*(t, \bar{r}) = \frac{1}{2} \mu \delta g_{00} = -\frac{M_* \mu}{R_*} \sum_{l_* \geq 2} \sum_{|m_*| \leq l_*} \frac{4\pi}{2l_* + 1} \left( \frac{\bar{r}}{R_*} \right)^{l_*} Y_{l_* m_*}^*(\Theta_*, \Phi_*) Y_{l_* m_*}(\bar{\theta}, \bar{\phi}). \quad (1.26)$$

we have the level mixing in terms of the coefficients  $c_i$  of the wavefunctions

$$i \frac{dc_i}{dt} = \sum_j \langle \psi_i | V_* | \psi_j \rangle c_j. \quad (1.27)$$

<sup>8</sup>At Lagrange point the attractive gravitational pull precisely cancels the centrifugal force required for a small object to move with them. In other words, objects sent to a Lagrange point tend to stay put there, see [24].

<sup>9</sup>Here the subscript  $i$  is a short-hand notation for  $nml$

In Appendix D I go over the level mixings in a more well-defined way. In Appendix D I also show how *resonances* may occur in the binary system due to the level mixing of the growing mode  $|211\rangle$  to one of the decaying ones. The resonance may be of the *Hyperfine* or *Bohr* type depending on if the orbits of the binary are co-rotating or counter-rotating respectively. In both instances the resonance occurs when the energy difference between the growing and decaying mode matches the orbital frequency  $\Omega$  of the binary. The resonance frequencies  $f_{res}$  are a characteristic feature of the binary system with a boson cloud and may be observable with current and future gravitational wave detectors, as we discuss in the next section.

## 1.6 Gravitational wave signatures

Gravitational waves are one of the most important predictions of Einstein's theory of general relativity. Their detection and interpretation have required three decades of remarkable progress in analytical and numerical computations. For Ultralight bosons, there are several characteristic gravitational wave signatures that will be emitted from the cloud. One may say that these emissions are what make these systems into indirect particle detectors. In the following sections I will go through the various signals and their observational prospects. I will end the section with an outlook on the role of numerical relativity for gravitational wave observations.

### 1.6.1 Annihilation

In the case for scalar fields, the high occupation number due to superradiance will lead to self-annihilation of ultralight bosons into gravitational waves. The primary source of these signals will be the signals from the dominant level,  $|211\rangle \times |211\rangle \rightarrow \text{GW}$ , since the higher overtones are suppressed at small  $\alpha$  due to their larger angular momentum via  $P_{GW}^{l,l'} \propto \alpha^{16+2(l+l')}$ , where  $l$  and  $l'$  are the angular momentum number of the two levels [21].

The dominant level will emit quasi-monochromatic *continuous* gravitational wave signals with an initial frequency of,

$$f \approx \frac{\mu}{\hbar\pi} \approx 645 \text{ Hz} \left( \frac{10M_\odot}{M} \right) \left( \frac{\alpha_i}{0.1} \right) \quad (1.28)$$

and initial strain amplitude

$$h_0 \approx 8 \times 10^{-28} \left( \frac{M_i}{10M_\odot} \right) \left( \frac{\alpha_i}{0.1} \right)^7 \left( \frac{\text{Mpc}}{D_L} \right) \left( \frac{\chi_i - \chi_f}{0.1} \right), \quad (1.29)$$

where  $D_L$  is the cloud's luminosity distance,  $\chi_i$  the initial black hole spin and  $\chi_f$  the *final* black hole spin related to  $\alpha_f$ , the final  $\alpha$ , calculated for the final black hole mass,

$$\chi_f = \frac{4\alpha_f m}{4\alpha_f^2 + m^2}. \quad (1.30)$$

For  $\alpha_i \geq 0.1$ , the approximation breaks down and (1.29) will give an overestimated GW power. Therefore, in [25] the strain amplitude has been estimated more accurately by using numerical results from [33] and using LIGO's conventional  $h_+$ ,  $h_x$  CW polarizations.

Since the emission of gravitational waves will remove energy and momentum from the cloud, its mass will gradually decrease over time and the signal frequency will evolve over time. Initially, the signal frequency in (1.28) will increase with the time-derivative, with respect to the proper time,

$$\dot{f} \approx 3 \times 10^{-14} \text{Hz/s} \left( \frac{M_i}{10M_\odot} \right)^2 \left( \frac{\alpha_i}{0.1} \right)^{19} (\chi_i - \chi_f)^2. \quad (1.31)$$

This increasing frequency is characteristic of the boson cloud and separates it from other CW sources such as nonaxisymmetric spinning neutron stars.

The decreasing cloud mass will also lead to a decrease in the GW amplitude which evolves as,

$$h(t) \propto h_0(1 + t/\tau_{GW})^{-1}, \quad (1.32)$$

with the initial  $h_0$  determined numerically and  $\tau_{GW}$  is the characteristic time-scale

$$\tau_{GW} \approx 6.5 \times 10^4 \text{yr} \left( \frac{M_i}{10M_\odot} \right) \left( \frac{0.1}{\alpha_i} \right)^{15} \frac{1}{(\chi_i - \chi_f)}. \quad (1.33)$$

[25]

## Multibanding

The emission of continuous gravitational waves from the cloud could be detected by detectors on the ground and in space. In [25] the strategy of *multibanding* as a way to detect ultralight bosons is discussed. Multibanding is the method of utilizing both space-based and ground-based gravitational wave detectors together as a way of finding and probing ultralight bosons in this case. As an example, detectors on the ground are sensitive to frequency band of  $[1, 10^3]$  Hz, suitable to probe bosons with masses  $[10^{-12}, 10^{-14}]$ . Although LISA would not be sensitive to bosons in this mass range, the black hole hosting the cloud could lie in a binary which falls in the LISA band  $[10^{-3}, 1]$  Hz. In other words, the GWs emitted from the binary inspiral would be detectable by LISA. From the inspiral signal one could infer the sky location and orientation as well as the expected signal frequency and frequency derivative of the continuous GWs. Thereby LISA would drastically simplify the search for continuous GWs by providing ground based detectors such as the Cosmic Explorer (CE) or the Einstein Telescope (ET) with crucial information and enable a follow-up on the ultralight bosons [25].

### 1.6.2 Signals in the binary

As we have discussed in section 1.5, the cloud will experience a Hyperfine (Bohr) resonance in its energy levels as an affect of having a binary companion in a corotating (counterrotating) orbit. The resonance will lead to a depletion of the cloud through one of its decaying modes. The depletion is characterized by the ratio of the mass of the binary companion and the black hole hosting the cloud. If the resonance frequency fall into the band of future detectors, it will

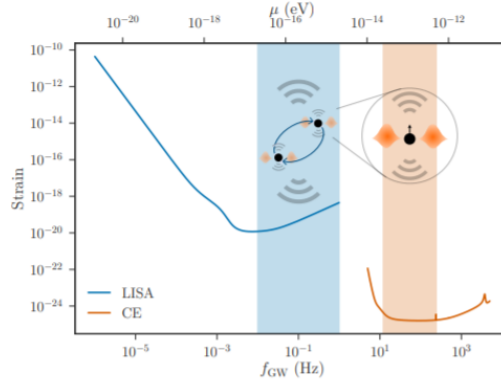


**Figure 1.3:** Strain vs  $f_{GW}$  for ultralight bosons in binary systems. The solid curves show the expected amplitude spectral densities of LISA (blue) and the cosmic explorer (orange) [25].

become a distinctive feature of the GW signal. The frequency is given by

$$f_{res} = \begin{cases} 7.2\text{mHz} \frac{1}{1+4\alpha^2} \left(\frac{\alpha}{0.1}\right)^7 \left(\frac{3M_\odot}{M}\right), & \text{Hyperfine} \\ 0.75\text{mHz} \left(\frac{\alpha}{0.1}\right)^3 \left(\frac{3M_\odot}{M}\right), & \text{Bohr} \end{cases} \quad (1.34)$$

$f_{res}$  has been plotted in Fig. 1.4 for physically motivated values of  $\alpha$  and  $M$ . The current ground-based detectors have a frequency range of 10 Hz-10KHz meaning that the resonant frequencies shown in Fig. 1.4 are too low to be observed. The most promising detector for probing ultralight bosons is therefore the future space-based LISA detector which has detection band in the mHz.

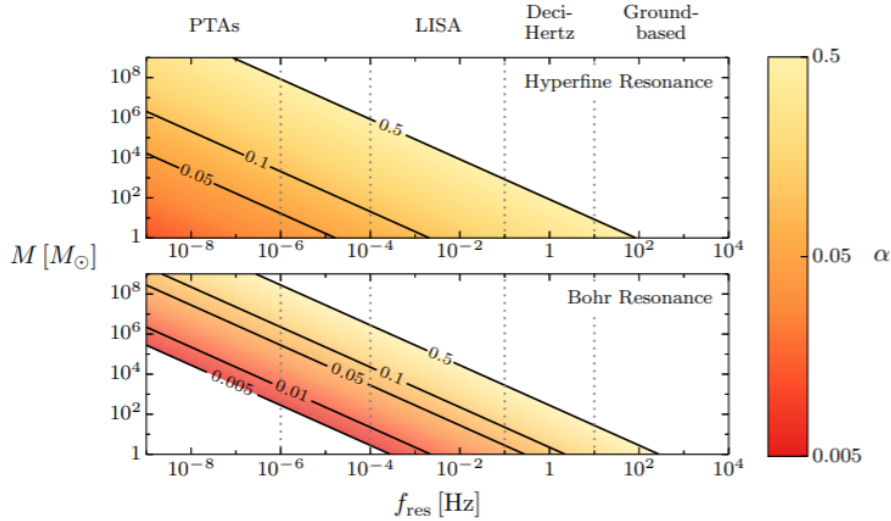


**Figure 1.4:** Resonance frequency  $f_{res}$  for physically motivated values of  $\alpha$  and  $M$ .

## More on observational prospects

In a recent paper [22] the contribution of boson clouds to the stochastic gravitational wave background (SGWB) have been studied in detail. In particular, the impact of higher modes ( $m > 0$ ) on the SGWB have been estimated. The SGWB is formed from the incoherent superposition of unresolved GWs from a population of BHs. In previous work the detectability of boson clouds in LIGO mainly with  $m = 1$  have been considered. In [22] it was shown that systems with  $m \geq 1$  do have instability timescales shorter than the age of the universe. To highlight the importance of the  $m > 1$  modes I have included a plot from [22] that shows the computation with only  $m = 1$  (dotted lines) and with the inclusion of all modes  $m \geq 1$  (solid lines). In Fig. 1.5 it is evident that higher  $m$ -modes are in particular important for  $\mu \geq 10^{-12}$

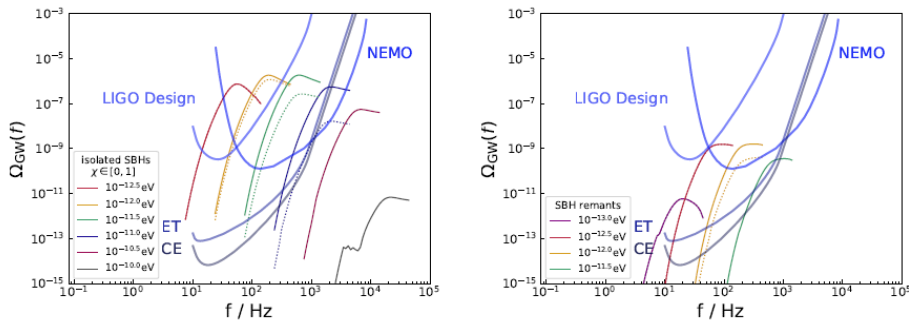


**Figure 1.5:** Computation of the SGWB when including only the  $m = 1$  mode, dotted lines, and including all  $m \geq 1$  modes, solid lines. Left image: SGWB from scalar clouds formed around spinning BHs with initial spin distribution  $\chi_i \in [0, 1]$  for BHs formed in isolation. Right image: Same as left but for BHs formed through binary BH mergers. The other lines represent the power-law integrated sensitivity curves for LIGO/NEMO/CE/ET at their design sensitivity.

eV, in agreement with [23]. However, for  $\mu \lesssim 10^{-12.5}$  eV the  $m > 1$  modes are negligible i.e. the solid and dotted lines in Fig. 1.5 are indistinguishable. On the other hand, for  $\mu \gtrsim 10^{-11}$  eV the background is entirely due to the  $m > 1$  modes. These results are especially important for future GW detectors as is evident in the left image of Fig. 1.5, the SGWB for such bosons could only be detected by detectors like NEMO, ET or CE.

## Caveats

In all of the papers that have considered the gravitational wave emission boson clouds, both for single and binary black holes, have a few caveats. Our main interest lies in *self-interactions* and *backreaction*. As was discussed in section 4.4, ultralight bosons may very well possess self-interactions. Self-interaction effects have yet to be considered in the search for gravitational waves. This is understandable because the analytical curves for bosons with self-interactions have yet to be obtained. Furthermore, the effect of backreaction is often neglected. Backreaction is the effect of an object on other objects/fields by their mutual interaction. Thus considering backreaction effects would help make predictions for current and future GW observations.

### 1.6.3 The role of numerical relativity

As the name suggests, approximate methods fail at regimes where the non-linear and strong field effects of general relativity are of out most importance. At this stage numerical simulations become essential to obtain solutions of the full Einstein equation's. A primary application is naturally the two-body problem which is approximated in Newtonian gravity as two point masses orbiting about each other. In General Relativity however, these orbits decay and the two objects spiral inwards whilst emitting gravitational waves. Gravitational waves are propagation variations of the metric tensor and effort of the gravitation physics community is to separate them from coordinate effects. In the current observations, accurate waveforms may start in the weak-field limit for the initial inspiral, where gravitational waves can be modelled as a perturbation around the background metric,  $g_{\mu\nu} = \eta_{\mu\nu} + h_{\mu\nu}$ , and including the results from numerical relativity. In order to create accurate gravitational waveform templates ready to be used by detectors, numerical relativity is crucial for the merger phase of the inspiral.

### Conclusion

Ordinary particle detectors are blind to the "dark sectors" in which particles couple weakly to SM ones. A creative way of detecting these particles is to utilize the natural phenomenon of BH superradiance which will produce a copious amount of sufficiently light particles. In a binary, the inclusion of a cloud will leave characteristic imprints on the gravitational wave emissions such as their masses and spins. These hypothetical systems may therefore be efficient as *gravitational colliders*. A crucial ingredient to detect and constrain the properties of ultralight bosons is numerical relativity. In the next chapter I will explain the mathematical foundation of numerical relativity, how astrophysical problems are dealt with in the numerical formalism as well as setup of our numerical code.

## Chapter 2

# Equations in the 3+1 formalism

In this chapter we will go through the mathematical description of the 3+1 formalism and thereby the foundation of numerical relativity. I will begin with a brief history of the Hamiltonian (3+1) formalism. In section 2.2 I will go over the necessary concepts from differential geometry to fully understand the 3+1 formalism. In section 2.7 I will discuss the initial data problem and a numerical method known as *the extended conformal thin sandwich method*. At the end of the chapter, the reader should be well-versed in the mathematical background to numerical relativity as well as how one can solve astrophysical systems numerically.

### 2.1 History of the Hamiltonian formalism

In the Hamiltonian formulation, Einstein's field equations can be understood as a dynamical system. It is often said that in General Relativity, spacetime becomes dynamical. This statement is meant to say that a field, which is subject to local laws of propagation and coupling, contains the information of the geometric structure of spacetime. This is not to be interpreted as spacetime as a *whole* evolves. Spacetime simply *is*. However, it does seem somewhat intuitive that the four-dimensional spacetime can itself be seen as an evolution of three-dimensional space. There are several redundancies to this construction, due to the fact that different evolutions of space can represent the same spacetime. However, because the resulting spacetime should satisfy Einstein's equation there must also be well-defined restrictions to the space's evolution. The main difficulty is then to write mathematical expressions to the redundancies in the construction as well as the constraint of evolution for this representation of spacetime as space's history. This results in describing Einstein's field equations as a *constrained Hamiltonian system* [28].

The foundation of the Hamiltonian formulation of general relativity is the so called *3+1 decomposition* of Einstein equations. The 3+1 decomposition originates from work done already in the 1920s. However, a stepping stone emerged in 1952 when Yvonne Choquet-Bruhat was able to show that the Cauchy problem arising from the 3+1 decomposition had a locally unique solution. One of the first people who studied how to put Einstein's equation in Hamiltonian form was Dirac. Dirac's work was then complemented by Richard Arnowitt, Stanley Deser, and Charles Misner. Their extensive work coined the term *the ADM formalism* in 1959 which



today is the most well-known Hamiltonian formulation of general relativity.

In the 1970s the 3+1 formalism became the primary application for numerical relativity. In the 1980s and 1990s the numerical codes increased in complexity from only being able to handle 1D spherical symmetric systems to be able 3D systems with no symmetries at all. Today, the main motivation for the expansion of numerical relativity is the development of current and future gravitational wave detectors. Both ground- (LIGO, VIRGO, GEO600, TAMA) and spacebased (LISA) [27].

## 2.2 Geometry of spacetime

### Manifolds

One of the the most fundamental concepts in in general relativity is the notion of *manifolds*. I will try to define and give an intuitive picture of these objects without using too many concepts from topology.

First of all we will remind the reader of the concept of an *open ball*. An open ball of radius  $r$  in  $\mathbb{R}^n$ , is the collection of points,  $y = (y_1, \dots, y_n)$  a distance  $r$  from its center  $x$ ,

$$B_r(x) = \{y : |y - x| < r\}. \quad (2.1)$$

Moreover, an *open set* in  $\mathbb{R}^n$  is any set which can be described as a union of open balls. With these objects we may give a more formal definition of a manifold:

*Definition 3.1:* An  $n$ -dimensional,  $\mathcal{C}^\infty$ , real manifold  $\mathcal{M}$ , is a set with a collection of subsets  $\{O_\alpha\}$  which satisfy the following three properties:

1. Each  $p \in \mathcal{M}$  lies in at least on of the  $O_\alpha \iff$  the  $\{O_\alpha\}$  cover  $\mathcal{M}$ .
2. For each  $\alpha$  there is a bijective map <sup>1</sup>,  $\psi_\alpha : O_\alpha \rightarrow U_\alpha$ , where  $U_\alpha$  is a subset of  $\mathbb{R}^n$ .
3. If any two sets  $O_\alpha, O_\beta$  overlap,  $O_{\alpha\beta} \neq \emptyset$ , one may consider the map  $\psi_\beta \circ \psi_\alpha^{-1}$  which takes points from  $\psi_\alpha [O_\alpha O_\beta] \subset U_\alpha$  to points in  $\psi_\beta [O_\alpha O_\beta] \subset U_\beta$ . Where  $U_\alpha, U_\beta \subset \mathbb{R}^n$  are open and  $\psi_\alpha$  is  $\mathcal{C}^\infty$ .

Furthermore, it is convenient to also include an additional requirement that the collection of charts  $\{\psi_\alpha\}$  and subsets  $\{O_\alpha\}$  is maximal. So that a new manifold cannot be defined simply by adding or subtracting a coordinate system [16].

For a more intuitive understanding of manifolds one may consider the most trivial example of a manifold namely the Euclidean space  $\mathbb{R}^n$ .  $\mathbb{R}^n$  can be covered by a single chart  $O = \mathbb{R}^n$  with  $\psi =$ identity map. In fact, an easier to remember 'definition' is that a manifold is a topological space which locally looks like the Euclidean space  $\mathbb{R}^n$ .

---

<sup>1</sup>A mathematician will call  $\psi_\alpha$  a *chart* whereas a physicist would call it a *coordinate system*. These terms are often used interchangeably in general relativity textbooks [16]

## Vector spaces

The reader is without doubt already familiar with vector spaces. In non-relativistic physics and even special relativity, space or spacetime is assumed to have the structure of a flat three or four dimensional vector space. Moreover, the rules for adding and scalar multiplying spatial displacements satisfies the vector space axioms<sup>2</sup>. This is not the case for curved geometries. There is no natural way in how to add to points on a sphere for example. The saviour to this bewilderment is called *tangent vectors* which lay the foundation of calculus on manifolds.

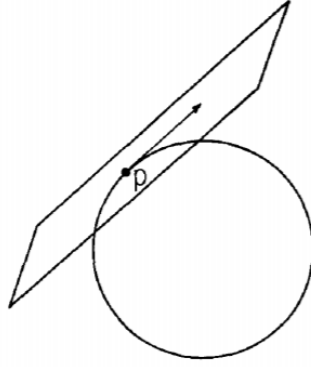


**Figure 2.1:** A tangent plane associated with the point  $p$  of a sphere in  $\mathbb{R}^3$

For a sphere, which arise as a natural embedding in  $\mathbb{R}^n$ , the tangent vector to a point  $p$  is a vector lying in the associated tangent plane, depicted in Figure 2.1. In general relativity however, one often deals with manifolds without an embedding in  $\mathbb{R}^n$ . Thus it is more useful to define a tangent vector related to the intrinsic curvature of the manifold rather than its potential embedding in  $\mathbb{R}^n$ . A more useful way to dealing with calculus on manifolds is to define a tangent vector as a directional derivative and fortunately, such a definition is easily provided.

In  $\mathbb{R}^n$  there is a one-to-one correspondence between tangent vectors and directional derivatives: A vector  $v = (v_1, \dots, v_n)$  defines the directional derivative operator  $\sum_{\mu} v^{\mu} (\partial/\partial x^{\mu})$  and vice versa. Directional derivatives are linear and obeys the Leibnitz rule when acting on functions. Thus, for a manifold  $M$  where  $\mathcal{F}$  is the collection of  $\mathcal{C}^{\infty}$  functions from  $M$  to  $\mathbb{R}$ . The tangent vector  $v$  at a point  $p$  is defined to be the map  $v : \mathcal{F} \rightarrow \mathbb{R}$ , which is linear and obeys the Leibnitz rule. The collection of tangent vectors  $\mathcal{V}_p$ , of vectors at  $p$ , has the structure of a vector space under the (1) addition law and (2) scalar multiplication law.

1.  $(v_1 + v_2)(f) = v_1(f) + v_2(f) \quad \forall f \in \mathcal{F}; v \in \mathcal{V}_p$
2.  $(av)(f) = av(f) \quad \forall f \in \mathcal{F}; v \in \mathcal{V}_p; a \in \mathcal{R}$

## Hypersurfaces

In order to understand the 3+1 formalism we must first define what we mean by a *hypersurface*.

---

<sup>2</sup>See for example [39] for a review on the axioms of vector spaces.

*Definition 3.1:* A hypersurface  $\Sigma$ , of an  $n$ -dimensional manifold  $\mathcal{M}$ , is the image of an  $(n-1)$ -dimensional submanifold  $\tilde{\Sigma}$  by an embedding  $\Phi : \tilde{\Sigma} \rightarrow \Sigma$ ,

$$\Sigma = \Phi(\tilde{\Sigma}). \quad (2.2)$$

Note that an **embedding** implies that  $\Phi : \tilde{\Sigma} \rightarrow \Sigma$  is a homeomorphism i.e. a one-to-one mapping such that  $\Phi$  and  $\Phi^{-1}$  are both continuous. This ensures that  $\Sigma$  doesn't intersect itself. Locally, a hypersurface can be defined with the aid of a scalar field  $t$  on  $\mathcal{M}$ . The hypersurface  $\Sigma$  is the set of points for which  $t$  is constant:

$$\forall p \in \mathcal{M}, p \in \Sigma \iff t(p) = 0. \quad (2.3)$$

In this thesis we will mostly be interested in a continuous set of hypersurfaces that cover the entire manifold  $\mathcal{M}$ . In fact, for most problems in astrophysics and cosmology the class of spacetimes one restricts themselves to is the so-called *globally hyperbolic spacetimes*. In particular, we will be interested in *Cauchy surfaces* which we define next:

*Definition 3.2:* A Cauchy surface is a spacelike hypersurface  $\Sigma$  in  $\mathcal{M}$  s.t. each timelike or spacelike (i.e. causal) curve intersects  $\Sigma$  once and only once. Alternatively,  $\Sigma$  is a Cauchy surface  $\iff$  its domain of dependence is the whole spacetime  $\mathcal{M}$ .

A spacetime  $(\mathcal{M}, \mathbf{g})$  which admits a Cauchy surface is called **globally hyperbolic**. The topology of a globally hyperbolic spacetime is necessarily  $\mathbb{R} \times \Sigma$ . This topology is essential in order to decompose  $\mathcal{M}$  into "space" and "time" as is required for the Hamiltonian formulation.

## 2.3 Foliation kinematics

If  $(\mathcal{M}, \mathbf{g})$  is a globally hyperbolic spacetime, then it can be foliated by a family of hypersurfaces  $(\Sigma_t)_{t \in \mathbb{R}}$ . By *foliation* (or *slicing*) one means that there exists a smooth scalar field  $\hat{t}$  on  $\mathcal{M}$  which is regular i.e. has a non-vanishing gradient. Furthermore, each hypersurface  $\Sigma_t$  is a level surface of  $\hat{t}$ :

$$\forall t \in \mathbb{R}, \Sigma_t := \{p \in \mathcal{M}, \hat{t}(p) = t\}. \quad (2.4)$$

Moreover, because  $\hat{t}$  is regular, this implies that the hypersurfaces are non-intersecting:

$$\Sigma_t \cap \Sigma_{t'} = \emptyset. \quad (2.5)$$

Each hypersurface is called a *leaf* or *slice* of the foliation. Furthermore, we assume that each  $\Sigma_t$  is spacelike and that the foliation covers all of  $\mathcal{M}$ :

$$\mathcal{M} := \bigcup_{t \in \mathbb{R}} \Sigma_t. \quad (2.6)$$

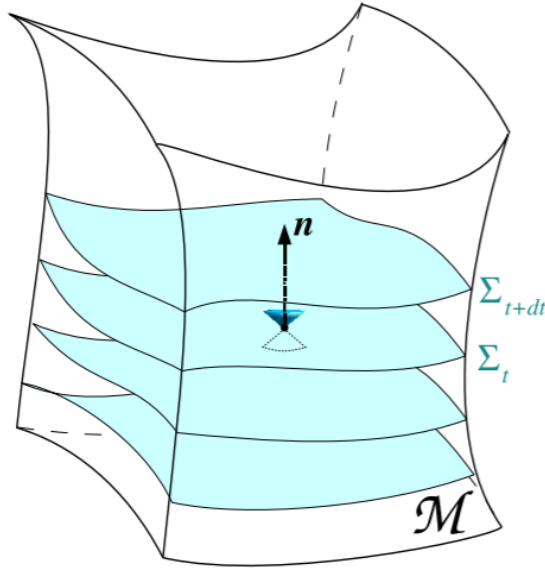


**Figure 2.2:** A foliation of the spacetime  $\mathcal{M}$  by a family of hypersurfaces  $(\Sigma_t)_{t \in \mathbb{R}}$  [27].

### The lapse function

The unit vector  $\mathbf{n}$  normal to  $\Sigma_t$  is timelike, future-directed and necessarily collinear to  $\vec{\nabla} \cdot t$ . One may therefore write:

$$\boxed{\mathbf{n} := -N \vec{\nabla} \cdot t} \quad (2.7)$$

where,

$$N := (-\vec{\nabla} \cdot t \cdot \vec{\nabla} \cdot t)^{-1/2} = (-\langle dt, \vec{\nabla} \cdot t \rangle)^{-1/2}. \quad (2.8)$$

**Remark 1:** The minus sign in 2.7 ensures that  $\mathbf{n}$  is future-directed whenever the scalar field  $t$  is increasing towards the future. The scalar field  $N$  in 4.6 is called the *lapse function*.

**Remark 2:** Note that by the construction of (?? it is ensured that  $N > 0$ . In particular  $N$  never vanishes for a regular foliation.

**Remark 3:** (2.7) also reveals that  $-N$  is the proportionality factor between the gradient 1-form  $dt$  and the 1-form  $\underline{\mathbf{n}}$ :

$$\underline{\mathbf{n}} := -N dt \quad (2.9)$$

### The normal evolution vector

Related to the lapse function is the *normal evolution vector*. It is defined in the following way:

$$\boxed{\mathbf{m} := N \mathbf{n}} \quad (2.10)$$

Because  $\mathbf{n}$  is a unit vector we immediately see that the square of  $\mathbf{m}$  is simply  $-N^2$ . Furthermore, from (2.7) and (2.9) we have:

$$\boxed{\langle \mathbf{d}t, \mathbf{m} \rangle = \nabla_{\mathbf{m}} t = m^\mu \nabla_\mu t = 1}. \quad (2.11)$$

The above relation reveals that  $\mathbf{m}$  is *adapted* to the scalar field  $t$  unlike the normal vector  $\mathbf{n}$ . The geometrical consequence of the above definition is that by a small displacement  $\delta t \mathbf{m}$  of each point of the hypersurface  $\Sigma_t$  one can reach the neighbouring hypersurface  $\Sigma_{t+\delta t}$ . Indeed, it is easy to convince oneself of this fact: Consider a point  $p$  in  $\Sigma_t$  and displace it by some small amount  $\delta t \mathbf{m}$  i.e. to the point  $p' = p + \delta t \mathbf{m}$ . From the definition of the gradient 1-form  $\mathbf{d}t$  we have:

$$t(p') = t(p + \delta t \mathbf{m}) = t(p) + \langle \delta t \mathbf{d}t, \mathbf{m} \rangle = t(p) + \delta \langle t \mathbf{d}t, \mathbf{m} \rangle = t(p) + \delta t. \quad (2.12)$$

Here the last equality shows that indeed  $p' \in \Sigma_{t+\delta t}$ . Therefore,  $\delta t \mathbf{m}$  carries the hypersurface  $\Sigma_t$  into the neighbouring one  $\Sigma_{t+\delta t}$ . Equivalently, one say that the hypersurfaces ( $\Sigma_t$ ) are **Lie dragged** by  $\mathbf{m}$ , justifying the name *normal evolution vector*.

## Eulerian observers

$\mathbf{n}$  is a timelike unit vector and can therefore be regarded as the 4-velocity of some observers. These observers are referred to as **Eulerian observers**. It follows that the worldlines of all Eulerian observers are orthogonal to the hypersurface  $\Sigma_t$ . From *Einstein's simultaneity convention* this means that  $\Sigma_t$  is locally the set of events which are simultaneous to all Eulerian observers.

### 2.3.1 Coordinate adaption to the foliation

In order to transform the Einstein equation's into a system of PDEs we need to introduce coordinates on the spacetime manifold  $\mathcal{M}$ . To this end we will also introduce two important concepts in numerical relativity namely *The lapse function* and *the shift vector*.

To start of, on each hypersurface  $\Sigma_t$  one introduces a coordinate system  $(x^i) = (x^1, x^2, x^3)$ . If the coordinate system varies smoothly between the neighbouring hyper surfaces then  $(x^\alpha) = (t, x^1, x^2, x^3)$  constitutes a well-behaved coordinate system on  $\mathcal{M}$ .  $(x^i) = (x^1, x^2, x^3)$  are referred to as the *spatial coordinates*.

The natural basis for the tangent space  $\mathcal{T}_p(\mathcal{M})$  is denoted by  $(\partial_\alpha) = (\partial_t, \partial_i)$  where:

$$\begin{aligned} \partial_t &:= \frac{\partial}{\partial t} \\ \partial_i &:= \frac{\partial}{\partial x^i}, i \in \{1, 2, 3\} \end{aligned} \quad (2.13)$$

**Remark:** The vector  $\partial_t$  is tangent to the the lines of constant spatial coordinates.  $\partial_t$  is called the *time vector*.

Similarly,  $\forall i \in \{1, 2, 3\}$  the vector  $\partial_i$  is tangent to the lines  $t = K^0, x^j = K^j (j \neq i)$  where  $K^0$  and  $K^j$  are constants. For  $t$  constant the lines belong to the hypersurfaces  $\Sigma_t$ .  $\rightarrow \partial_i$  is tangent

to  $\Sigma_t$ :

$$\partial_i \in \mathcal{T}_p(\Sigma_t), i \in \{1, 2, 3\}. \quad (2.14)$$

The time vector  $\partial_t$  Lie drags the hypersurface  $\Sigma_t$ , as the normal evolution vector 2.10 does. The difference between the two is called the *shift vector* and is denoted as  $\beta$ :

$$\boxed{\partial_t := m + \beta}. \quad (2.15)$$

It is often more convenient to rewrite the above equation with the relation from 2.10:

$$\boxed{\partial_t = N\mathbf{n} + \beta} \quad (2.16)$$

the beauty of the above equation is that because  $\mathbf{n}$  is normal to  $\Sigma_t$  and  $\beta$  tangent to  $\Sigma_t$ , 2.16 can therefore be seen as a 3+1 decomposition of the time vector  $\partial_t$ . From 2.16 one can easily compute the square of the time vector:

$$\partial_t \cdot \partial_t = -N^2 + \beta \cdot \beta \quad (2.17)$$

From which the following conditions emerge:

$$\begin{aligned} \partial_t \text{ is timelike} &\iff \beta \cdot \beta < N^2 \\ \partial_t \text{ is null} &\iff \beta \cdot \beta = N^2 \\ \partial_t \text{ is spacelike} &\iff \beta \cdot \beta > N^2 \end{aligned} \quad (2.18)$$

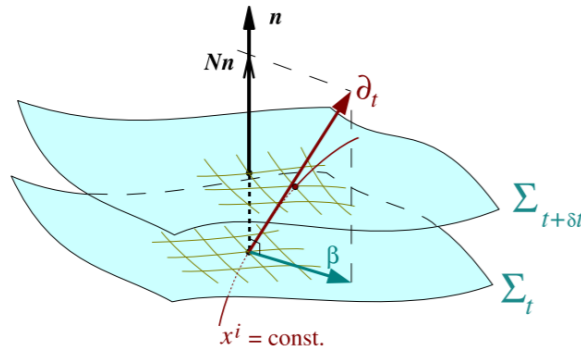


**Figure 2.3:** Coordinates  $(x^i)$  on the hypersurface  $\Sigma_t$ . Each constant line  $x^i = \text{const}$  intersects the foliation  $(\Sigma_t)_{t \in \mathbb{R}}$  thereby defining the time vector  $\partial_t$  and shift vector  $\beta$  of the spacetime coordinate system  $(x^\alpha) = (t, x^i)$ .

## Rewriting the metric in 3+1 form

The spatial 3-metric  $\gamma$  with respect to the  $(x^i)$  coordinates can be written in terms of its  $\gamma_{ij}$  components:

$$\gamma := \gamma_{ij} \mathbf{d}x^i \otimes \mathbf{d}x^j. \quad (2.19)$$

In the same way the metric  $\mathbf{g}$  can be written as:

$$\mathbf{g} := g_{\alpha\beta} \mathbf{d}x^\alpha \otimes \mathbf{d}x^\beta, \quad (2.20)$$

where each component is determined via

$$g_{\alpha\beta} := \mathbf{g}(\partial_\alpha, \partial_\beta). \quad (2.21)$$

Therefore, by means of (2.17) we have the spacetime metric in line element form [27]

$$\boxed{g_{\mu\nu} dx^\mu dx^\nu = -N^2 dt^2 + \gamma_{ij} (dx^i + \beta_i dt)(dx^j + \beta^j dt)}. \quad (2.22)$$

### Coordinates via the lapse and the shift

In this section we have showed that a unique lapse function and shift vector  $\beta$  are determined by introducing a coordinate system  $x^\alpha$  on  $\mathcal{M}$  in such a way that the constant hypersurfaces  $x^0$  are zero. One may also go the opposite way: Giving a hypersurface  $\Sigma_0$  and introducing a scalar field  $N$ , a vector field  $\beta$  and a coordinate system  $(x^i)$  will specify a unique coordinate system  $(x^\alpha)$  in some neighbourhood of  $\Sigma_0$  such that the hypersurface  $x^0 = 0$  is  $\Sigma_0$ . Geometrically, one may think of the lapse as specifying for each point on  $\Sigma_0$  how "far above" is the corresponding point on  $\Sigma_{\delta t}$ . The shift vector then describes how to propagate the coordinate system  $(x^i)$  from  $\Sigma_0$  to  $\Sigma_{\delta t}$  [27].

## 2.4 A introduction to General Relativity

We now turn to General Relativity in form of Einstein's equations. A spacetime is a manifold  $\mathcal{M}$  endowed with a metric  $g_{\mu\nu}$ , where  $g_{\mu\nu}$  measures length and the infinitesimal line element

$$ds^2 = g_{\mu\nu} dx^\mu dx^\nu \equiv \sum_{\mu\nu=0}^n g_{\mu\nu} dx^\mu dx^\nu \quad (2.23)$$

provides a generalization of the Pythagorean theorem. The field equations of General relativity are Einstein's equations. In an  $n$ -dimensional spacetime Einstein's equations form a set of  $\frac{1}{2}n(n+1)$  non-linear partial differential equations for  $\frac{1}{2}n(n+1)$  functions. Analogous to how Maxwell's equations govern the response of electric and magnetic fields to charges and currents, Einstein's equations govern how the spacetime metric  $g_{\mu\nu}$  respond to energy and momentum.

$$\boxed{G_{\mu\nu}(g, \partial g, \partial^2 g) \equiv R_{\mu\nu} - \frac{R}{2} g_{\mu\nu} = 8\pi T_{\mu\nu}(g, \Phi)} \quad (2.24)$$

The geometric quantity of Einstein's equations is contained in the Einstein tensor  $G_{\mu\nu}$  on the left-hand side of equation (2.24) whereas the matter quantity is in the energy-momentum tensor  $T_{\mu\nu}$ .  $R_{\mu\nu}$  is known as *the Ricci tensor* and is the differential operator acting on  $g_{\mu\nu}$

$$R_{\mu\nu} = \partial_\rho \Gamma_{\mu\nu}^\rho - \partial_\mu \Gamma_{\rho\nu}^\rho + \Gamma_{\rho\sigma}^\rho \Gamma_{\mu\nu}^\sigma - \Gamma_{\sigma\mu}^\rho \Gamma_{\rho\nu}^\sigma, \quad (2.25)$$

$$\Gamma_{\mu\nu}^{\rho} = \frac{1}{2}g^{\rho\sigma} (\partial_{\mu}g_{\nu\sigma} + \partial_{\nu}g_{\mu\sigma} - \partial_{\sigma}g_{\mu\nu}). \quad (2.26)$$

Despite the elegance of equation (2.24)-(2.26), the co-variant, four-dimensional form of Einstein's equations is not convenient for a numerical implementation, in which one rather want to describe how gravitational fields evolve from some initial configuration toward the future. It is more intuitive to consider how a foliation with three-dimensional spatial slices evolve in time and where the evolution of each slice is given by Einstein's equations. This is the concept behind the 3+1 formalism to which we turn to next [29].

## 2.5 The 3+1 formalism

At the core of numerical relativity we find the 3+1 formalism. The goal of the formalism is to decompose the four-dimensional manifold into a three-dimensional spatial part and a one-dimensional temporal part. As a consequence, the co-variant form of Einstein's equations are converted into a set of evolution equations for three-dimensional geometric fields. The 3+1 decomposition can be achieved in three steps

1. *Specify the choice of coordinates* - A well known feature of Einstein's equations is that they can be written in the same generic way on any coordinate system, defined by a set of observers. In the decomposed spacetime, the observers are determined by the congruence of time lines which intersect the spatial hypersurfaces  $\Sigma$ . The congruence is parametrized by the vector field  $t^a = Nn^a + \beta^a$  where  $n^a$  is the timelike unit normal vector,  $N$  is the lapse function which measures the proper time of the Eulerian (orthogonal) observers,  $\beta$  is the shift vector which measures the displacement between consecutive hypersurfaces, see Figure 2.2.
2. *Decompose every 4D into 3+1 components* - The choice of coordinates allows for the definition of a spatial projection operator  $\gamma_{\nu}^{\mu} \equiv \delta_{\nu}^{\mu} + n^{\mu}n_{\nu}$ . Any four dimensional tensor can be decomposed into 3+1 pieces by either using the spatial projector to obtain the spatial components or contracted with  $n^a$  for the time components. In the following sections we will introduce the decomposition of well-known tensors such as the metric, stress-energy and Ricci tensor.
3. *Write down Einstein's field equations in their 3+1 components* - With the framework outlined here the 3+1 decomposition of Einstein's equations can be written as a set of constraint and evolution equations. In the end, Einstein's equation will be rewritten as a well-posed initial value problem which is the goal of the 3+1 formalism.

With the method outlined we will derive the 3+1 decomposition of Einstein's equation relative to the foliation introduced in the previous chapter. This eventually give rise to the Cauchy problem with constraints which in turn is the core of the 3+1 formalism. The essence of the 3+1 formalism is to project the above Einstein equation onto a hypersurface  $\Sigma_t$  and perpendicular to  $\Sigma_t$ . To this end, we first consider the projection of the stress-energy tensor.



### 2.5.1 Decomposition of the energy-momentum tensor

First step is to decompose the stress-energy tensor into 3+1 form. By its definition we can define the matter energy density with an Eulerian observer  $n^\mu$  as the strictly time-like component of  $T^{\mu\nu}$

$$\boxed{\rho := n_\mu n_\nu T^{\mu\nu}} \quad (2.27)$$

Similarly we may define the matter density momentum measured by an Eulerian observer as the purely spatial projection of the stress-energy tensor

$$\boxed{S_{ij} := \gamma_i^\mu \gamma_j^\nu T_{\mu\nu}}. \quad (2.28)$$

At this point it may serve to recall the physical interpretation of  $\mathbf{S}$ : In the rest frame of an Eulerian observer, take two, possibly equal, spacelike vectors  $\mathbf{e}$  and  $\mathbf{e}'$ .  $S(\mathbf{e}, \mathbf{e}')$  is the force in  $\mathbf{e}$  direction acting on the unit surface with normal  $\mathbf{e}'$ . Where  $S$  is the trace of the stress tensor

$$S = g^{\mu\nu} S_{\mu\nu} = \gamma^{ij} S_{ij} \quad (2.29)$$

Finally, we will consider the mixed projection of the stress-energy tensor. In other words we project one index of  $T_{\mu\nu}$  with the normal projection operator  $n^\nu$  and one with the spatial projection operator  $\gamma_i^\mu$ . The resulting quantity is known as the *momentum density*

$$\boxed{j_i = -n^\nu \gamma_i^\mu T_{\mu\nu}} \quad (2.30)$$

Armed with the knowledge of  $(\rho, S_{ij}, j_i)$  one can reconstruct the energy-momentum tensor in the 3+1 formalism as:

$$T_{\mu\nu} = n_\mu n_\nu \rho + 2n_{(\mu} j_{\nu)} + S_{\mu\nu} \quad (2.31)$$

Taking the trace of (2.31) yields the trace of the energy-momentum tensor in terms of the 3+1 quantities

$$\boxed{T = \rho + S} \quad (2.32)$$

With the 3+1 decomposition of the energy-momentum tensor obtained, we may consider the remaining projection of the Einstein equation (2.24).

### 2.5.2 Projection of the Einstein equation

In differential geometry it is often customary to define an additional tensor  $K_{ij}$  which has a purely geometrical meaning.  $K_{ij}$  is known as the *extrinsic curvature* and measures the change in the induced metric  $\gamma_{ij}$  along the congruence of the normal observers. It is defined using a *Lie derivative*  $\mathcal{L}_n$ , a generalization of a directional derivative along the vector  $n$  in a manifold.

$$K_{ij} \equiv -\frac{1}{2} \mathcal{L}_n \gamma_{ij} = -\frac{1}{2N} (\partial_t - \mathcal{L}_\beta) \gamma_{ij}, \quad (2.33)$$

$$\mathcal{L}_\beta \gamma_{ij} = \beta^k \partial_k \gamma_{ij} + \gamma_{ik} \partial_j \beta^k + \gamma_{kj} \partial_i \beta^k. \quad (2.34)$$

Equipped with the 3+1 decomposition of the energy-momentum tensor (2.31) and the definition of the extrinsic curvature (2.33) we are ready to fully project the Einstein equation along and onto the hypersurfaces  $\Sigma_t$  [27].

### 1) Projection perpendicular to $\Sigma_t$

Projecting the indices of (2.24) perpendicular to  $\Sigma_t$  is achieved by contracting  $G_{\mu\nu}$  twice with the unit normal vector

$$n^\mu n^{\nu 4} R_{\mu\nu} - \frac{1}{2} R n^\mu n^\nu g_{\mu\nu} = 8\pi n^\mu n^\nu T_{\mu\nu} \quad (2.35)$$

With the spacetime metric written in its spatial and timelike components, one can show that  $n^\mu n^\nu g_{\mu\nu} = -1$ . As a result, the left-hand side is recognized as the scalar Gauss equation, A. From our decomposition of the energy-momentum tensor we recognize the right-hand side from (2.27) and the resulting equation reads

$$\boxed{{}^3R + K^2 - K_{ij}K^{ij} = 16\pi\rho} \quad (2.36)$$

The above equation is known as *the Hamiltonian constraint equation*. (2.36) is the first of two constraint equations that belong to the 3+1 formalism.

### 2) Mixed projection along and perpendicular to $\Sigma_t$

To obtain the second constraint equation we perform a mixed projection of (2.24). Similar to the previous section, we project one index of (2.24) with  $n^\nu$  and one with  $\gamma_i^\mu$  yielding

$$\gamma_i^\mu n^{\nu 4} R_{\mu\nu} - \frac{1}{2} R \gamma_i^\mu n^\nu g_{\mu\nu} = 8\pi \gamma_i^\mu n^\nu T_{\mu\nu} \quad (2.37)$$

The right-hand side is easily recognized as the momentum density in (2.30). The second term on the left-hand side of the equation is easily shown to be vanishing  $\gamma_i^\mu n^\nu g_{\mu\nu} = \gamma_i^\mu n_\mu = 0$ . The first term can be substituted with the extrinsic curvature from the contracted Codazzi equation (A.3)

$$\boxed{D_j K^{ij} - D^i K = 8\pi j^i}. \quad (2.38)$$

The above equation is the second constraint equation known as *the momentum constraint*. In a few sections the word constraint will become clear.

### 3) Projection onto $\Sigma_t$

Finally we perform the last projection, the projection of (2.24) onto the hypersurface  $\Sigma_t$ . To simplify things we rewrite (2.24) in terms of the energy-momentum tensor  $T_{\mu\nu}$  and its trace  $T = g^{\mu\nu} T_{\mu\nu}$ . By contraction the Einstein field equation with the inverse metric we obtain  ${}^4R = -8\pi T$ . Substituting this in (2.24) yields an equivalent form of Einstein field equation

$${}^4R_{\mu\nu} = 8\pi \left( T_{\mu\nu} - \frac{1}{2} T g_{\mu\nu} \right). \quad (2.39)$$

The elegance of (2.39) is that we may express its projection onto  $\Sigma_t$  with the stress-energy tensor and energy density (2.27) by substituting in (2.31) and (2.32)

$$\gamma_i^\mu \gamma_j^{\nu 4} R_{\mu\nu} = 8\pi \left( S_{ij} - \frac{1}{2}(S - \rho)\gamma_{ij} \right). \quad (2.40)$$

The above equation can be rewritten by means of the full projection of the Ricci tensor (2.25)

$$\boxed{(\partial_t - \mathcal{L}_\beta) K_{ij} = -D_i D_j N + N [{}^3R_{ij} + K K_{ij} - 2K_{ik} K_j^k + 4\pi((S - \rho)\gamma_{ij} - 2S_{ij})]} \quad (2.41)$$

This is the last ingredient in the decomposition of the Einstein field equation, it is known as *the Evolution equation*. Unlike the Hamiltonian (2.36) and momentum constraint (2.38) equations which specify the conditions for the data  $\{\gamma_{ij}, K_{ij}\}$  on each hypersurface  $\Sigma_t$ , the evolution equation (2.41) specifies how the data evolve from one hypersurface to the next on the foliation.

**Note I:** In numerical relativity the system (2.36), (2.38), (2.41) is often referred to as the *ADM equations*, contributed to the work of Arnowitt, Deser and Misner. However, the main contribution of ADM is the Hamiltonian formulation of general relativity. This Hamiltonian approach is not used in numerical relativity however, which instead involves integrating (2.36), (2.38), (2.41). The latter was known well before the work by ADM. In particular, the extrinsic curvature  $K_{ij}$  was recognized as a fundamental 3+1 variable due to work by Darmois in 1927 [36].

**Note II:** Important to note is that the (2.36), (2.38), (2.41) system does not contain any time derivative of the lapse  $N$  or of the shift  $\beta$ . Meaning that  $N$  and  $\beta$  are not dynamical variables. This fact is somewhat intuitive since they arise from the choice of coordinates  $(t, x^i)$ . This coordinate freedom allow us to choose the lapse function and shift vector freely without changing the physical solution  $g_{\mu\nu}$  of Einstein's equation <sup>3</sup>.

## Summary

The system (2.36), (2.38), (2.41) is equivalent to the Einstein field equation (??). It is easy to confirm that the new system of equations have the same number of independent components as the original Einstein equation. The Hamiltonian constraint is a scalar equation and therefore has one independent component; the momentum constraint on  $\Sigma_t$  is a vector equation and therefore has three independent components; the evolution is a rank-2 tensorial equation on the three-dimensional hypersurfaces  $\Sigma_t$  and therefore has six independent components. Consequently, the 3+1 system of equations (2.36), (2.38), (2.41) has the same number of components as the four-dimensional Einstein equation (2.24) [27].

<sup>3</sup>Important to keep in mind however, is that an arbitrary choice of  $N$  and  $\beta$  may lead to coordinate singularities.

## 2.6 Scalar field equations in the 3+1 formalism

Recall from chapter 1 that we wish to study dark matter modelled as a scalar field around a black hole. We have already seen the Klein-Gordon equation of a complex scalar field on a black hole background (1.7). In this section we will go through the equations of a complex scalar field in the 3+1 formalism. To this end, we start with defining the *canonical momentum* which is defined as the change of the field along the flow of the normal vector  $\mathbf{n}$

$$\Pi = -\frac{1}{2}\mathcal{L}_n = -\frac{1}{2}n^\mu\partial_\mu\phi = \frac{1}{2N}(\mathcal{L}_\beta\phi - \partial_t\phi), \quad + c.c. \quad (2.42)$$

In the second equality the fact that a Lie derivative of a scalar field reduces to a partial derivative (??) has been utilized and the third equality has been obtained with the substitution of (2.16).

We now turn to the 3+1 decomposition of the Klein-Gordon equation on a hypersurface  $\Sigma_t$ . To this end, we write the spacetime metric and the covariant derivative in terms of their spatial counterparts. Substituting ref yields

$$\begin{aligned} g^{\mu\nu}\nabla_\mu\nabla_\nu\phi &= \nabla_\mu(g^{\mu\nu}\nabla_\nu\phi) \\ &= \nabla_\mu[(\gamma^{\mu\nu} - n^\mu n^\nu)\nabla_\nu\phi] = \nabla_\mu[D^\mu\phi + 2n^\mu\Pi] \\ &= \gamma^{ij}D_iD_j\phi + \frac{1}{N}\gamma^{ij}D_iND_j\phi + 2\mathcal{L}_n\Pi - 2K\Pi. \end{aligned} \quad (2.43)$$

Where the definition of the canonical momentum (2.42) has been substituted in the second equality and the mean curvature has been substituted in the third equality [38].

### 2.6.1 Stationary solution

In this thesis, we aim to solve the stationary system of equation on an initial slice. Therefore, we must eventually set the time-derivatives to zero. However, a vanishing time-derivative in (2.42) would have us lose the quasi-stationary solutions of the cloud. To avoid the time-dependence whilst maintaining the stationary solutions of the cloud we consider the ansatz of the scalar field in Boyer-Lindquist coordinates (1.20). Taking the time-derivative of this ansatz in the canonical momentum leaves us with

$$\Pi = \frac{1}{2N}(\mathcal{L}_\beta\phi + i\omega\phi), \quad \Pi^* = \frac{1}{2N}(\mathcal{L}_\beta\phi^* - i\omega\phi^*). \quad (2.44)$$

We wish to substitute the stationary expression for the canonical momentum into the 3+1 decomposition of the Klein-Gordon equation. Accordingly, one must expand the Lie derivative of the canonical momentum

$$\begin{aligned} \mathcal{L}_n\Pi &= \frac{1}{N}\left[\partial_t\left(\frac{\beta^i\partial_i\phi + i\omega\phi}{2N}\right) - \mathcal{L}_\beta\left(\frac{\beta^i\partial_i\phi + i\omega\phi}{2N}\right)\right] \\ &= \frac{1}{2N^2}\left[-2i\omega\beta^i\partial_i\phi + (\partial_t\beta^i)(\partial_i\phi) + \omega^2\phi - \beta^i\beta^j\partial_i\partial_j\phi - \beta^i(\partial_i\beta^j)\partial_j\phi\right] \\ &\quad - \frac{1}{2N^3}\left[(\beta^i\partial_i\phi + i\omega\phi)\partial_tN - (\beta^i\partial_i\phi + i\omega\phi)\beta^j\partial_j\phi\right], \quad + c.c. \end{aligned} \quad (2.45)$$

In the expansion, the time-derivative of (1.20) has been utilized repeatedly to write  $\partial_t \phi = -i\omega \phi$ . Furthermore, for stationary black hole spacetimes, such as Schwarzschild, time-derivatives of the lapse and shift vanish. Therefore, our resulting Klein-Gordon equation can be expressed in terms of the scalar field  $\phi$ , its mass  $\mu$  as well as the 3+1 quantities; the lapse function  $N$  and the shift vector  $\beta^i$ ,

$$\boxed{D_i D^i \phi + \frac{1}{N} D_i N D^i \phi + 2\mathcal{L}_n \Pi - 2K\Pi - \mu^2 \phi^2 = 0, +c.c.} \quad (2.46)$$

Note that the potential term in is the same as in (1.7). Thus, when adding a quartic self-interaction term to our potential,  $V(\phi) = \frac{1}{2}\mu^2 \phi^2 - \frac{1}{4}\lambda \phi^4$ , the Klein-Gordon equation becomes

$$\boxed{D_i D^i \phi + \frac{1}{N} D_i N D^i \phi + 2\mathcal{L}_n \Pi - 2K\Pi - \mu^2 \phi^2 - \frac{1}{4}\lambda \phi^4 = 0, +c.c.} \quad (2.47)$$

**Note:** Comparing the decomposed Klein-Gordon equation (2.46) with the initial (1.7) we notice that there are three free data variables  $N, \beta^i, K$  that has emerged from the time-component of the four-dimensional Laplacian in the (1.7) Klein-Gordon equation.

## 2.6.2 The energy-momentum tensor

Recall from section (2.5.1) we showed how the energy-momentum tensor in the 3+1 formalism is described in terms of the energy density  $\rho$ , the momentum density  $j^i$  and the stress tensor  $S_{ij}$ . In this section we will present the derivation of these quantities for a complex scalar field.

The energy-momentum tensor of a complex scalar field is [30]

$$T_{\mu\nu} = \nabla_\mu \phi \nabla_\nu \phi^* + \nabla_\nu \phi \nabla_\mu \phi^* - g_{\mu\nu} (g^{\alpha\beta} \nabla_\alpha \phi \nabla_\beta \phi^* + \mu^2 \phi^* \phi). \quad (2.48)$$

Substituting (4.6) in the definition of the energy density (2.27) yields

$$\rho = n_\mu n_\nu T^{\mu\nu} = 4\Pi\Pi^* + \mu^2 \phi\phi^* + \partial_i \phi \partial^i \phi^* \quad (2.49)$$

where once again  $n^\mu n^\nu g_{\mu\nu} = -1$ , the definition of  $\gamma_{ij}$  and  $n^\mu \partial_\mu \phi^{(*)} = \Pi^{(*)}$  from (2.42) was used [38]. Similarly, the momentum density of a complex scalar field is given by

$$j^i = -n_\mu \gamma_\nu^i T^{\mu\nu} = 2(\Pi^* \partial^i \phi + \Pi \partial^i \phi^*), \quad (2.50)$$

recall from section 2.5.1 that  $n_\mu \gamma_\nu^i g^{\mu\nu} = 0$ . Finally we obtain the scalar field stress-energy tensor by projecting with the spatial metric twice along the normal of  $\Sigma_t$

$$S_{ij} = \gamma_i^\mu \gamma_j^\nu T_{\mu\nu} = \partial_i \phi \partial_j \phi^* + \partial_j \phi \partial_i \phi^* + \gamma_{ij} (\Pi\Pi^* - \partial_k \phi \partial^k \phi^* - \mu^2 \phi\phi^*). \quad (2.51)$$

Like previously, we will contract  $S_{ij}$  with the spatial metric and using the fact that  $\gamma^{ik} \gamma_{kj} = \delta_j^i = 3$ , we find the trace  $S$

$$S = \gamma^{ij} S_{ij} = 12\Pi\Pi^* - \partial_i \phi \partial^i \phi^* - 3\mu^2 \phi\phi^*. \quad (2.52)$$

By substituting our results of the energy density and trace of the stress-energy tensor for a complex scalar field we find the trace of the scalar field energy-momentum tensor to be

$$T = S - \rho = 2(4\mu\mu^* - \partial_i\phi\partial^i\phi^* - 2\mu^2\phi\phi^*) \quad (2.53)$$

**Summary:** At this stage we have obtained the 3+1 decomposition of the Einstein field equation, which resulted in two constraint equations and one evolution equation, as well as of the Klein-Gordon of a complex scalar field. We have also presented the matter equations in terms of the 3+1 quantities and scalar field. However, the constraint equations hide most of the physical degrees of freedom one would like to fix in order to solve for a specific configuration. In the next section I will go over a numerical method which allows one to freely specify various quantities.

## 2.7 The initial data problem

After the 3+1 decomposition the equations (2.36), (2.38), (2.41) constitute a *Cauchy problem*. Namely, given some initial data, one can search for a solution. The choosing of initial data is a highly non-trivial task and can in fact be divided into two different problems.

*i) The mathematical problems:* We require that both the Hamiltonian (2.36) and momentum (2.38) constraints are satisfied. Furthermore, the matter distribution  $(\rho, j^i)$  may have some constraints on its own that we shall not discuss here.

*ii) The astrophysical problems:* The solution to the constraint equations should correspond to the physical system one wishes to study.

Note that (2.36) and (2.38) only refer to a single hypersurface  $\Sigma_0$  rather than an entire foliation  $(\Sigma_t)_{t \in \mathbb{R}}$ . Thus, a naive way to proceed would be to choose the metric  $\gamma$  freely, thereby fixing the scalar curvature  $R$ , and solve (2.36) and (2.38) for the components  $K_{ij}$ . However, as shown by Choquet-Bruhat [?] this approach is not solid since there are only four equations for six unknowns and there is no natural way of choosing the last two components of  $K_{ij}$ . Thankfully, there is a much more suitable way of choosing the initial data by a split of  $(\gamma_{ij}, K_{ij})$  into freely specified parts and parts obtain from the solution of (2.36) and (2.38). The method is referred to as *conformal decomposition* and is the most widely spread technique to obtain initial data in the 3+1 formalism. In the following section I will introduce the conformal decomposition of the constraint equations and the numerical method known as *the extended conformal thin sandwich method*.

### 2.7.1 Conformal decomposition of the constraints

A conformal transformation of the induced metric  $\gamma_{ij}$  is defined as:  $\gamma_{ij} = \Psi^a \bar{\gamma}_{ij}$ . Although  $a$  is arbitrary it has been shown that  $a = 4$  is the most suitable choice when solving a 3+1 system of equations on an initial slice [41]. Therefore, the induced metric  $\gamma_{ij}$  on the hypersurface  $\Sigma_t$

can be decomposed as:

$$\gamma_{ij} = \Psi^4 \tilde{\gamma}_{ij} \quad (2.54)$$

where  $\Psi^4$  is some strictly positive scalar field known as the *conformal factor* and  $\tilde{\gamma}_{ij}$  an auxiliary metric on  $\Sigma_t$ . Most numerical methods which try to solve the initial data problem involve a conformal decomposition of the induced metric. However, most methods differ in their handling of the extrinsic curvature. How one chooses to decompose the extrinsic curvature determines the set of free data to be chosen before solving the constraint equations. It is customary to split the extrinsic curvature into a trace and traceless part  $A_{ij}$

$$A^{ij} = K^{ij} - \frac{1}{3}K\gamma^{ij}. \quad (2.55)$$

How one chooses to decompose  $A_{ij}$  is a distinguishing feature of their method to solve the initial value problem. In the approach we have used, which will be discussed in a few sections,  $A_{ij}$  will be expressed in terms of the lapse function, conformal metric and shift vector. This is realized by considering the evolution equation for the conformal factor:

$$\left(\frac{\partial}{\partial t} - \mathcal{L}_\beta\right) \ln \Psi = \frac{1}{6} \left(\tilde{D}_i \beta^i - NK\right). \quad (2.56)$$

Which can be rewritten in terms of the conformal metric:

$$\boxed{\left(\frac{\partial}{\partial t} - \mathcal{L}_\beta\right) \tilde{\gamma}_{ij} = -2N\Psi^{-4}A_{ij} - \frac{2}{3}\tilde{D}_k \beta^k \tilde{\gamma}_{ij}}. \quad (2.57)$$

This encourages one to introduce the following quantity

$$\tilde{A}_{ij} := \Psi^{-4}A_{ij} \quad (2.58)$$

Furthermore, by noticing that  $-\mathcal{L}_\beta \tilde{\gamma}_{ij}$  can be rewritten as [27]

$$-\mathcal{L}_\beta \tilde{\gamma}_{ij} = \left(\tilde{L}\beta\right)^{ij} + \frac{2}{3}\tilde{D}_k \beta^k \tilde{\gamma}_{ij}, \quad (2.59)$$

the equation above for the traceless part of extrinsic curvature,  $\tilde{A}^{ij}$ , can be written like

$$\boxed{\tilde{A}^{ij} = \frac{1}{2N} \left(\dot{\tilde{\gamma}}^{ij} + \left(\tilde{L}\beta\right)^{ij}\right)}. \quad (2.60)$$

If we compare the above decomposition of  $A_{ij}$  with the original one in (2.55) we notice that  $A_{ij}$  is now described by the shift vector, lapse function and conformal metric rather than  $\{K_{ij}, K\}$ .

## 2.7.2 Conformal decomposition of the constraint equations

With the definitions of the decomposed extrinsic curvature and conformal metric we may perform a conformal decomposition of the Hamiltonian and momentum constraint equations. At this stage we do not present the conformal decomposition of the evolution equations, since we only want to solve the constraints on a single slice. However, the evolution part of the system

will come up at a later stage.

The conformal decomposition of the Hamiltonian constraint equation is obtained from the relation between the regular and conformal Ricci scalar (??) and the conformal extrinsic curvature  $A_{ij}$  (2.60) substituted in (2.36). To write  $K_{ij}K^{ij}$  use the fact that  $A_{ij}$  is traceless to obtain

$$K_{ij}K^{ij} = A_{ij}A^{ij} + \frac{1}{3}K^2 \quad (2.61)$$

The above equation together with the conformal Ricci scalar and  $A_{ij}$  yields the conformal Hamiltonian constraint equation

$$\boxed{\tilde{D}_i \tilde{D}^i \Psi - \frac{\tilde{R}}{8} \Psi + \frac{1}{8} A_{ij} A^{ij} \Psi^5 - \frac{K^2}{12} \Psi^5 = -2\pi\rho\Psi^5}. \quad (2.62)$$

The key part of the conformal decomposition is that the constraint equation is now written as a second order partial differential equation.

For the momentum constraint equation (2.38) we substitute the divergence of  $A_{ij}$  which yields

$$D_j A^{ij} - \frac{2}{3} D^i K = 8\pi j^i \quad (2.63)$$

Furthermore, from the relation between the conformal and regular covariant derivative (A.7) and the fact that  $\tilde{\gamma}_{ij} A^{ij}$  gives the divergence of  $A_{ij}$  as

$$D_j A^{ij} = \tilde{D}_j A^{ij} + 10A^{ij} \tilde{D}_j \ln \Psi \quad (2.64)$$

Substituting this into (2.63) and performing the conformal transformation of the derivative of the mean curvature in the second term yields the conformal momentum constraint

$$\boxed{\tilde{D}_j A^{ij} + 10A^{ij} \tilde{D}_j \ln \Psi - \frac{2}{3} \Psi^{-4} \tilde{D}^i K}. \quad (2.65)$$

**Note 1.** In the derivation of the conformal constraint equations (2.62) and (2.65) no specific decomposition of  $A_{ij}$  have been utilized. Meaning that (2.62) and (2.65) are in fact the general conformal constraint equations.

**Note 2.** The method in which  $A^{ij}$  is described by the shift vector  $\beta$ , the lapse  $N$  and the time-derivative of the conformal metric  $\hat{\gamma}^{ij}$  is known as *The conformal thin sandwich method (CTS)*. Because  $\hat{\gamma}^{ij}$  can be obtained from the value of  $\gamma^{ij}$  of the neighbouring hypersurfaces  $\Sigma_t$  and  $\Sigma_{t+\delta t}$  thereby creating a *thin sandwich*.

### 2.7.3 Conformal decomposition of the Klein-Gordon equations

To solve for the boson cloud we must also perform the conformal decomposition of the two first term in the Klein-Gordon equation (2.46). The first term is transformed by noting that the covariant derivative of a scalar field is just a partial derivative whereas the second term is transformed similar to (??) thus we get for the conformal transformation of the Klein-Gordon



equations [38]

$$\frac{\Psi^{-4}}{N} \tilde{D}_i N \tilde{D}^i \phi + \Psi^{-4} \tilde{D}_i \tilde{D}^i \phi + 2\Psi^{-5} \tilde{D}_i \phi \tilde{D}^i \Psi + 2\mathcal{L}_\Pi - 2K\Pi - \mu^2 \phi = 0, \text{ +c.c.} \quad (2.66)$$

where  $\Pi$  and  $\mathcal{L}_\Pi$  are defined as in (2.42) and (2.45). Note that (2.66) is for a scalar field without self-interactions.

Finally we must provide the conformal decomposition of the matter equations presented in section 2.5.1. Luckily, this is rather straightforward. Note that in all of the matter equations (2.27), (2.50) and (2.52) there is a derivative with an upper index. Consequently, we may transform these equations in a similar fashion to (A.7). Therefore, we find for the conformal energy density, momentum density and trace of the stress tensor

$$\rho = 4\Pi\Pi^* + \mu^2 \phi \phi^* + \Psi^{-4} \tilde{D}_i \phi \tilde{D}^i \phi^* \quad (2.67a)$$

$$j^i = 2\Psi^{-4} (\Pi \tilde{D}^i \phi + \Pi \tilde{D}^i \phi^*) \quad (2.67b)$$

$$S = 12\Pi\Pi^* - \Psi^{-4} \tilde{D}_i \phi \tilde{D}^i \phi^* - 3\mu^2 \phi \phi^* \quad (2.67c)$$

$$(2.67d)$$

where  $\Pi^{(*)}$  is defined as in (2.42). The matter equations may be rescaling with different powers of  $\Psi$  if one wishes to linearize the equations of motion.

## 2.8 The extended conformal thin sandwich (XCTS)

At this stage in the chapter we have obtained the conformal Hamiltonian and momentum constraint equations which all depend on the traceless part of the extrinsic curvature,  $A^{ij}$ . What still remains is to choose the conformal method i.e. the decomposition of  $A^{ij}$  which determines the free initial data. In this work we are using a method known as *The extended conformal thin sandwich* (XCTS) which I present below.

The original conformal thin sandwich (CTS) approach was introduced by York in 1999. The name stems from the fact that in the CTS one is concerned with the evolution of the conformal metric between two neighbouring hypersurfaces, which constitute a thin sandwich. In the CTS approach,  $A^{ij}$  is decomposed in terms of the shift vector, lapse function and time-derivative of the conformal metric, which is what we have derived in section 2.7.1. Due to this decomposition of  $A^{ij}$  one must specify  $\{\tilde{\gamma}_{ij}, \dot{\tilde{\gamma}}_{ij}, N, K, \rho, j^i\}$  before solving the Hamiltonian and momentum constraint equations on the initial slice to obtain the conformal factor  $\Psi$  and shift vector  $\beta^i$ . The main advantage of the CTS to other conformal methods is that one have a greater set of initial free data to specify. The free initial data set one specifies is also closer to the actual physical system to be solved.

If we turn our focus to the astrophysical problem described at the beginning of section 2.7 we realize that there is not a straightforward way of choosing the lapse function  $N$  in the CTS method. The suggestion by Pfeiffer and York is this: Instead of introducing an arbitrary value

of the lapse,  $N$  can be determined from the Einstein equation via the time-derivative of the trace of the extrinsic curvature,  $K$ . This equation will then be added to the initial data system such that one solves for  $\{N, \Psi, \beta^i\}$ . This conformal method is what is known as *The extended conformal thin sandwich* (XCTS) method. The XCTS equations have already been derived in [38]

$$\boxed{(\partial_t - \mathcal{L}_\beta)K = -\Psi^{-4} \left( \tilde{D}_i \tilde{D}^i N + 2\tilde{D}_i N \tilde{D}^i \ln \Psi \right) + N \left[ 4\pi(\rho + S) + A_{ij} A^{ij} + \frac{1}{3}K \right]} \quad (2.68)$$

### 2.8.1 XCTS approach to a static black hole

To demonstrate the XCTS method let us look at a simple example of a static Schwarzschild spacetime, see section 2.9 for a review. The simplest choice of the free data is the following

$$\tilde{\gamma}_{ij} = f_{ij}, \quad \dot{\tilde{\gamma}}_{ij} = 0, \quad K = 0, \quad \dot{K} = 0, \quad \tilde{E} = 0, \quad \tilde{S} = 0 \text{ and } \tilde{p}^i = 0. \quad (2.69)$$

In other words, we are looking for vacuum initial data on a maximal and conformally flat hypersurface with all freely specifiable derivatives set to zero. With (2.69) the forementioned XCTS system of equations reduces to

$$D_i D^i \Psi = -\frac{1}{8} \Psi^5 A_{ij} A^{ij}, \quad (2.70a)$$

$$D_i D^i N = -2\Psi^{-1} D_i \Psi D^i N + N A_{ij} A^{ij}, \quad (2.70b)$$

$$D_j D^j \beta^i + \frac{1}{3} D^i D_j \beta^j = 2A^{ij} (D_j N - 6N\Psi^{-1} D_j \Psi). \quad (2.70c)$$

For a spherical coordinate system  $(x^i) = (r, \theta, \phi)$  it has been derived in [27] that for the asymptotically flat end  $r \rightarrow \infty$  the simplest solution of (2.70a)-(2.70c) with  $\beta = 0$  leads to

$$\lim_{r \rightarrow \infty} N = 1 \text{ and } \lim_{r \rightarrow \infty} \Psi = 1. \quad (2.71)$$

The asymptotic limits of  $N$  and  $\Psi$  will show up in Chapter 5 when we discuss the results of backreaction.

**Note:** The equations (2.70) constitute the **extended conformal thin sandwich (XCTS)** system for the initial data problem for a static black hole. In which the free data are: the conformal metric  $\tilde{\gamma}$ , its coordinate time derivative  $\dot{\tilde{\gamma}}$ , the extrinsic curvature trace  $K$ , its coordinate time derivative  $\dot{K}$  and the rescaled matter variables  $\tilde{E}$ ,  $\tilde{S}$  and  $\tilde{p}^i$ . The constraint data are: the conformal factor  $\Psi$ , the conformal lapse  $\tilde{N}$  and the shift vector  $\beta$ .

## 2.9 An introduction to black holes in General Relativity

The most famous full solution of Einstein's equation is called the *Schwarzschild solution*, which describes spherically symmetric vacuum spacetime. Since we are in vacuum, the Einstein's equations become  $R_{\mu\nu} = 0$ . I will not go through the entire derivation of the Schwarzschild

metric but a great resource is [17],

$$ds^2 = - \left(1 - \frac{2GM}{r}\right) dt^2 + \left(1 - \frac{2GM}{r}\right)^{-1} dr^2 + r^2 d\Omega^2 \quad (2.72)$$

Here,  $M$  is interpreted as the conventional Newtonian mass that can be measured by observing the orbits at far distances. As  $M \rightarrow 0$  one recover the Minkowski metric, as expected. The same goes for when  $r \rightarrow 0$ , a property which is known as *Asymptotic flatness*. The Schwarzschild solution is in fact the unique, spherically symmetric, asymptotically flat solution of Einstein's equation. This is called *Birkhoff's theorem*, see [17] for a proof. Birkhoff's theorem tells us that spherically symmetric implies a *static* spacetime. In other words, if its stationary<sup>4</sup> and invariant under  $t \rightarrow -t$ .

As is evident from (2.72), the Schwarzschild metric's components diverges for  $r = 0$  and  $r = 2GM$ . The divergences are of two different natures. The divergence at  $r = 0$  is called the *singularity*. As we approach this point the theory of general relativity breaks down and our description of spacetime is invalid. To make an accurate prediction we must turn to a quantum theory of spacetime.

In contrast, the surface associated to the point  $r = 2GM$  is not as dramatic. The divergence is due to a poor choice of coordinates; the surface is in fact what is referred to as the *event horizon* or just horizon. Indeed, many of the interesting and surprising properties of black holes lie in interpreting the horizon.

In this thesis we are working with the Schwarzschild metric in *isotropic coordinates*. The isotropic coordinates are obtained with the following transformation of the radial coordinate [18]:

$$r = \bar{r} \left(1 + \frac{M}{2\bar{r}}\right)^2 \quad (2.73)$$

From the above transformation one can derive the Schwarzschild metric in isotropic coordinates

$$ds^2 = - \left(\frac{\bar{r} - \frac{M}{2}}{\bar{r} + \frac{M}{2}}\right)^2 dt^2 + \left(\frac{\bar{r} + \frac{M}{2}}{\bar{r}}\right)^4 (d\bar{r}^2 + \bar{r}^2 d\Omega^2). \quad (2.74)$$

It is not hard to see that the spatial part of the above metric have the same form as the Euclidean metric,  $d\Sigma^2 = d\bar{r}^2 + \bar{r}^2(d\theta^2 + \sin^2\theta)$ , unlike the Schwarzschild metric in (2.72). The property of having the spacelike slices being Euclidean is of importance in numerical relativity because one often chooses an ansatz which is conformally flat.

Furthermore, unlike the Schwarzschild metric in (2.72), the metric in isotropic coordinates does not have a singularity at  $r = 2M$ . In other words, it describes spacetime outside of the event horizon which is located at  $r = M/2$ . The fact the isotropic coordinate system is well-behaved at horizon is useful when considering across-horizon phenomenon [18].

<sup>4</sup>A spacetime is called *stationary* if it admits a timelike Killing vector field  $K$  everywhere.

For superradiance, the *Kerr solution* of the Einstein equation's is necessary. So called *Kerr black holes* are rotating, meaning that they have a rotational axis which by definition breaks the rotational symmetry. As a consequence, the Kerr solution more complicated than the Schwarzschild (2.72). For convenience the Kerr metric is often written in the following way,

$$ds^2 = -dt^2 + \frac{\rho^2}{\delta} dr^2 + \rho^2 d\theta^2 + (r^2 + a^2) \sin^2 \theta d\phi^2 + \frac{\Delta}{\rho^2} (a \sin^2 \theta d\phi - dt)^2 \quad (2.75)$$

where,

$$\delta(r) = r^2 - 2GMr + a^2 \quad (2.76)$$

and

$$\rho^2(r, \theta) = r^2 + a^2 \cos^2 \theta. \quad (2.77)$$

In this case  $a$  corresponds to the rotation of the black hole and  $M$  its mass. It is straightforward to see that as  $a \rightarrow 0$  (2.75) reduces to the Schwarzschild metric (2.72). The coordinates  $(t, r, \theta, \phi)$  are known as *Boyer-Lindquist* coordinates.

The most interesting part of black holes is undoubtedly the *event horizon*. The event horizon is the hypersurface that separate the spacetime points connected to infinity<sup>5</sup> by timelike paths from those that are not. The event horizon is a global concept and a statement of the spacetime as a whole meaning that it cannot be determined from knowing the geometry at that location. Therefore, it is not straightforward how to locate the event horizon if one is handed a metric in arbitrary coordinates.

In the coordinates given for the Kerr metric the event horizon is located at  $g^{rr} = 0$ . From (2.75)  $g^{rr} = \Delta/\rho^2$  and  $\rho^2 \geq 0$  meaning that  $g^{rr} = 0$  for

$$\Delta(r) = r^2 - 2GMr + a^2 = 0. \quad (2.78)$$

We end up with three possibilities:  $GM > a$ ,  $GM = a$  and  $GM < a$ . However, the last case implies a naked singularity<sup>6</sup> and the extremal  $GM = a$  case is unstable [17]. Therefore, we focus on the possibility with physical interest  $GM > a$ . Solving (2.78) gives

$$r_{\pm} = GM \pm \sqrt{G^2 M^2 - a^2}. \quad (2.79)$$

Both of these radii are null hypersurfaces and will turn out to be event horizons. To realize this let us turn our attention back to the Kerr metric in (2.75). It is not to hard to realize that there are two Killing vectors<sup>7</sup> in the metric (2.75), namely  $K = \partial_t$  and  $KR = \partial_\phi$  since the metric coefficients are independent of both  $t$  and  $\phi$ . Furthermore,  $K^\mu$  is not orthogonal to any hypersurfaces at all implying that the metric is stationary but not static. This is

<sup>5</sup>By 'infinity' I mean 'spacetime sufficiently far away from the black hole can be approximated by Minkowski space.

<sup>6</sup>Naked singularity is a singularity which is not hidden behind an event horizon.

<sup>7</sup>Killing vectors are vectors that satisfy Killing's equation. They are in a one-to-one correspondence with the symmetry of the metric on that manifold. If the metric coefficients are independent of some coordinate  $x^{\sigma^*}$  then  $K = \partial_{\sigma^*}$  is a Killing vector.

understandable since the black hole is spinning it cannot be static however, it is spinning exactly the same way at all times so it is stationary. The norm of  $K^\mu$  is given by

$$K^\mu K_\mu = -\frac{1}{\rho^2}(\Delta - a^2 \sin^2 \theta). \quad (2.80)$$

This norm does not vanish at the outer event horizon  $r_+$  but is equal to

$$K^\mu K_\mu = -\frac{a^2 \sin^2 \theta}{\rho^2} \geq 0. \quad (2.81)$$

In other words the Killing vector is spacelike at the outer horizon except at the north and south-poles ( $\theta = 0, \pi$ ) where it is null. The locus of points where  $K^\mu K_\mu = 0$  is known as the *stationary limit surface* given by

$$(r - GM)^2 = G^2 M^2 - a^2 \cos^2 \theta. \quad (2.82)$$

However, note that the outer event horizon is given by

$$(r_+ - GM)^2 = G^2 M^2 - a^2. \quad (2.83)$$

Hence there is a region between the stationary limit surface and the outer horizon and this is what is known as an *ergosphere*. Whatever enters the ergosphere cannot remain stationary but must move with the rotation of the black hole (the  $\phi$  direction). However, you may still move toward or away from the event horizon and have no trouble exiting the ergosphere. It is within the ergosphere where the Penrose process may occur and where one could exit the ergosphere with more energy that they entered it with. It is this dissipative energy property of Kerr black holes which lay the foundation for superradiance and other interesting phenomena.

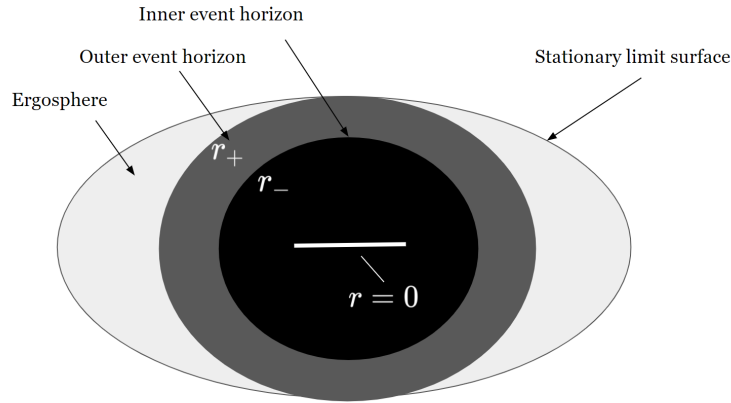


**Figure 2.4:** An illustration of the event horizons and ergosphere of a Kerr black hole.

## 2.10 Gauge invariant quantities

In this work we focus on a single black hole in asymptotically flat spacetimes i.e. spacetimes that becomes flat sufficiently far away from the black hole horizon<sup>8</sup>. With an asymptotically flat spacetimes there are several approaches to define globally conserved quantities at spatial infinity. The Hamiltonian approach to General Relativity provides a natural framework to discuss physical quantities in asymptotically flat spacetimes. In this section I will go over the quantities associated with the 3+1 formalism such as the notion of mass, linear and angular momentum. The derivation of these quantities may be found in [27] and [31]

The first quantity that can be described with the 3+1 decomposition is the *ADM mass*. We will define it in the *quasi-isotropic gauge* to which the isotropic Schwarzschild solution in (2.74) also belongs to namely

$$\frac{\partial \tilde{\gamma}_{ij}}{\partial x^j} = \mathcal{O}(r^{-3}). \quad (2.84)$$

The flat divergence of the conformal metric is what is called the *quasi-isotropic gauge*. The condition (2.84) restricts the choice of coordinates rather than the nature of spacetime at spatial infinity. In the quasi-isotropic gauge we may define the ADM mass as the flux at infinity of the gradient of the conformal factor  $\Psi$

$$M_{ADM} = -\frac{1}{2\pi} \oint_{\infty} D_i \Psi dS^i. \quad (2.85)$$

The ADM mass may also be referred to as the total energy of a gravitational system and is therefore always positive. The total angular momentum is in turn defined by a similar integral taken at infinity

$$J = \frac{1}{8\pi} \oint_{\infty} A_{ij} m^i dS^j \quad (2.86)$$

where  $m^i$  is the rotational vector normal to the system's center of mass. Finally, if the spacetime  $(\mathcal{M}, \mathbf{g})$  admits a time symmetry (i.e. is stationary) we may define a global quantity known as the Komar mass

$$M_K := -\frac{1}{4\pi} \oint_{\infty} D^i N dS^i \quad (2.87)$$

The ADM mass, total angular momentum and Komar mass can be used to define quantities for a binary system such as its binding energy. For a single black hole analysis these quantities are helpful in determining the effect of superradiance. For example, in a physical case of superradiance one would expect the ADM mass to have increased by 1% – 30%. We will get back to this quantity when discussing the results of backreaction in Chapter 5.

---

<sup>8</sup>There are different approaches to achieve asymptotic flatness. The desire to explain asymptotic flatness without relying on specific coordinates have led to the *conformal compactification picture* in which infinity is transformed to a finite distance by means of an appropriate spacetime conformal transformation.

## Chapter 3

# Kadath

In this project a spectral solver known as **Kadath** is used. As the name suggest, spectral solvers implements spectral methods: a class of numerical methods that have been shown to be efficient when solving numerical problems in General Relativity. In simple terms, spectral methods solves partial differential equations by first describing the field as a linear combination of known functions such as *Legendre* or *Chebyshev*. We consistently utilize the Chebyshev spectral expansion with **Kadath** since they have been shown to converge slightly faster than Legendre polynomials. We shall attempt to outline the method of working with Kadath in this chapter. In the first section I will explain the basics of spectral methods before moving on the setup of **KADATH** in section 3.2.

### 3.1 Spectral methods

When simulating and solving PDEs numerically one runs into the trouble of how to represent and take the derivative of functions when your computer only deals with finite integers. The straightforward strategy is to utilize *finite-difference methods*, in which one sets up a grid of  $N + 1$  points and represent a function  $f$  by its value on these  $N + 1$  points. In those cases the error in the approximation for the derivative  $f'$  will decay as  $1/N$ , assuming an equidistant grid.

Spectral methods offers an alternative way, instead of representing  $f$  on a grid it is represented in terms of its coefficients  $\{c_i\}_{i=0,\dots,N}$  from a finite basis of known functions  $\{\Phi_i\}_{i=0,\dots,N}$

$$f(x) \approx \sum_{i=0}^N c_i \Phi_i(x). \quad (3.1)$$

As an example, if  $f$  is a periodic function with period two, the basis functions would be  $\Phi_{2i} = \cos(\pi i x)$ ,  $\Phi_{2i+1} = \sin(\pi i x)$ . In this case Eq. (3.1) is simply the truncated Fourier decomposition of  $f$ . From the  $c_i$ 's one can in general compute the derivatives with the knowledge of the expression for  $\Phi_i$  as a function of  $\{\Phi\}_{i=0,\dots,N}$ . Because  $\{\Phi\}_{i=0,\dots,N}$  corresponds to a complete basis in some finite-dimensional space, whereas  $f$  generally belongs to some infinite-dimensional space, the expression in (3.1) is approximate. Regardless, one of the major advantages for spectral methods is the rapid decay of errors, faster than powers of  $1/N$  and

most often exponential  $e^{-N}$ , for well-behaved functions.

In physics, spectral methods were initially applied in numerical fluid dynamics, preferred for their high accuracy. From fluid dynamics, one of the first published results of solving Einstein's equations using spectral methods was in 1991 by Gourgoulhon, the spherical collapse of a neutron star to a black hole [35]. A decade later, in 2001, spectral methods had grown in complexity with Kidder et. al. being the first to fully evolve the three-dimensional Einstein equation's. Nowadays, numerical relativity is mainly associated with modelling gravitational sources by simulating the last stages of a binary coalescence.

## 3.2 An introduction to KADATH

### Multi-domain decomposition

`Kadath` works with a multi-domain composition which, as the name suggests, decompose the space into different domains. The main advantage of this approach is that discontinuities in the fields can be put at the surface of each domain. This leads to all functions being  $C^\infty$  within each domain thereby recovering the spectral convergence. Furthermore, with the domain decomposition one has the freedom to specify the resolution in each domain thereby increasing accuracy in domains where needed. For each domain there is a mapping of the set of physical coordinates and the set of numerical coordinates. The spectral expansion is performed for the numerical ones and the mapping between the two sets of coordinates ensures that the numerical ones lie in an appropriate range for the expansion. For example, using the Chebyshev polynomials a coordinate must lie in the range  $[-1, 1]$ .

There are different classes of decomposition depending on which system one is concerned with. For the stationary, Schwarzschild black hole one uses the class `Space_spheric` where the domains are implemented as spherical shells. The coordinates are, as one might expect, the usual spherical ones  $(r, \theta, \phi)$ :

$$\begin{aligned} x &= r \sin \theta \cos \phi \\ y &= r \sin \theta \sin \phi \\ z &= r \cos \theta \end{aligned} \tag{3.2}$$

For all domains in this space, the numerical angular coordinates  $(\theta^*, \phi^*)$  are identical to their physical counterparts. In this setup the fields are assumed to be either symmetric or anti-symmetric with respect to the  $z = 0$  plane. Therefore,  $\theta$  is restricted to lie in the interval  $[0, \pi/2]$ . For the  $\phi$  coordinate, no symmetry is assumed and it lays in the interval of  $[0, 2\pi[$ . For the radial coordinate  $r$  the domains used in this work are called `Domain_nucleus` and `Domain_shell`. The class `Domain_nucleus` represent a spherical domain that encloses the origin of the coordinate system up to a finite radius, in our work this is denoted as  $r_1$  in Figure 3.1. The class `Domain_shell` represents a spherical shell in which the radius  $r$  lies between finite values, this is denoted as  $r_2$  and  $r_3$  in our domains in Figure 3.1.



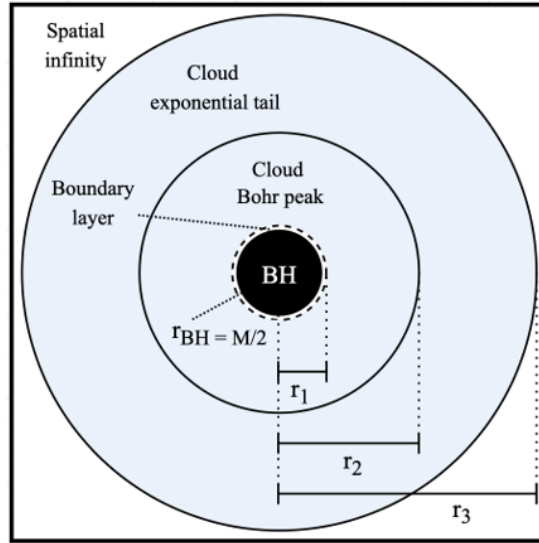


**Figure 3.1:** All the domains used in the setup of our KADATH code. Credit: Christoffel Doorman.

### Setting the equations

There are several derived classes for setting the equations for the fields. In Appendix C one may see many examples of the class `Eq_bc` in which the boundary conditions are encoded. The class must be supplied with the domain and type of boundary. Needless to say, the setting of the correct boundary conditions is extremely important and may be the main source of errors in many cases.

Because we are dealing with multiple domains, the class `Eq_matching` aids in imposing the matching of equations across the boundary of two domains. This must be done when the basis relative to the surface is the same in each domain, which is the case for the spherical space.

### Solving the system

In general the equations that are solved for are non-linear and KADATH relies on the well-known *Newton-Raphson iteration technique* to find a solution. To understand this technique let us consider a set of unknowns that we denote by the vector  $\vec{u}$ . The system of equations can then be described by  $\vec{f}(\vec{u}) = 0$ . Starting from an initial guess  $\vec{u}^0$  the solution is found by iteration. We denote the approximation of the solution found by the  $n$ th iteration as  $\vec{u}^n$ . The Newton-Raphson iteration proceeds as follows: Firstly the vector  $\vec{f}^n = \vec{f}(\vec{u}^n)$  is computed. If  $\vec{f}^n$  is small enough then  $\vec{u}^n$  is an appropriate solution. If not, one computes the Jacobian matrix  $\mathbf{J}^n$  of the system

$$J_{ij}^n = \frac{\partial f_i}{\partial u_j}(\vec{u}^n) \quad (3.3)$$

One row of the Jacobian corresponds to one equation and one column to the derivation with respect to the one of the unknowns. The Jacobian is calculated at the current position  $\vec{u}^n$  and must be recalculated for each iteration. The system that must be solved is then the linear

system

$$\mathbf{J}^n \vec{X}^n = \vec{f}^n \quad (3.4)$$

and the next approximation of the solution is given by  $\vec{u}^{n+1} = \vec{u}^n - \vec{X}^n$ . If the initial guess is good, the method is famous for converging rapidly.

The size of the linear system in (3.4) is equal to the total number of unknowns. Therefore, if there are  $N_f$  fields, to be solved in  $N_d$  domains of dimension  $d$ , where  $N$  is the number of coefficients in the spectral expansion in each dimension. The resulting Jacobian is an  $(m \times m)$  matrix where  $m \approx N_f N_d N^d$ .  $m$  can thereby end up being rather large, especially in three dimensions. For instance if  $N_f = 5$ ,  $N_d = 6$ ,  $d = 3$  and  $N = 21$  one ends up with  $m \geq 250\,000$ . The matrix one is left with corresponds to more than 500 GB of data which is well over the amount of data one would be able to store on a single processor. Thankfully, it is straightforward to parallelize<sup>1</sup> KADATH. In general each processor only have knowledge of some parts of the matrix. In other words, the Jacobian will be computed column by column, each computation is independent resulting in each processor computing and storing a manageable amount of columns.

## User interface

The first step when using KADATH is to specify the geometry of space. As mentioned previously, we call the constructor `Space_spheric`. Several parameters are needed to specify the space such as the number of shells. The constructor must also be supplied with the required resolution i.e. number of numerical points per domain and if Legendre or Chebyshev polynomials are to be used (Chebyshev in our case).

On the desired geometry one must then define the fields of interest, in our case we are interested in scalar fields and their equations and definitions can be found in Appendix B and C. The result is sought out by iteration and the objects are therefore often set to some initial guess. The initial guess could come from data from another code or some analytical values. A crucial point in this process is to associate each field with the correct spectral basis of decomposition. Thankfully, KADATH provides a function which does this automatically but one might still need to control that the functions provided are appropriate for the problem.

The information necessary to solve the system is contained in the class `System_of_equations`. The class is constructed from the space of interest and one supplies in which domains the system is to be solved, for cases when the fields are not to be solved for the entire space. One must then pass a list of variables and constants to the system. Variables are unknowns and must be solved for whereas constants are quantities that may appear in the equations and have fixed values. Both variables and constants can be fields or numbers and both types of quantities must be initialized beforehand. Each quantity is labeled by a character string which is the name that will be recognized by the equations. See how this is done in Appendix C.

---

<sup>1</sup>Parallell computing is, as the name suggest, a type of computation in which many calculations or processes are performed simultaneously.

The equations are passed as character strings to `System_of_equations` and those strings are then passed to `KADATH` to generate appropriate computation rules. The way indices are handled is inspired by LaTeX, where Einstein's summation convention is used. When setting the equations one must make sure they produce to the same amount of conditions as unknowns, in order to have an invertible system.

# Chapter 4

## Numerical results

In this chapter I will present the numerical results that have been conducted during my thesis work. I will begin by explaining the numerical setup of our `KADATH` code as well as some initial obstacles and their solutions. The first few results will also include several tests of the code's robustness including a convergence study of the resolution in the domains. The complexity of the study will increase as the chapter progress. In section 4.3 I present the free bosonic field profile and thereafter the new effects from the inclusion of self-interactions. In the last two section I considering the effects of backreaction for the free and self-interacting boson field.

### 4.1 Numerical setup

As mentioned in the previous chapter, we use the spectral solver `KADATH` to study the effect of boson clouds around a single black hole. The static Schwarzschild spacetime is characterized by the XCTS quantities:

1. The lapse function  $N$ .
2. The conformal factor  $\Psi$ .
3. The shift vector  $\beta$ .

Because we are in quasi-isotropic coordinates we are free to choose a gauge in which  $\beta = 0$ , this choice reduces the size of the system and increases the likelihood of convergence. In the first few sections we are assuming no backreaction. Therefore, we may solve the system in two steps. Firstly, we solve for the background fields  $N$  and  $\Psi$  with the equations introduced for a static Schwarzschild black hole in the XCTS method, (2.70), only now we exclude the third equation involving  $\beta$ . Secondly, we fix the black hole background and solve the equations for the field given the spacetime, i.e. (B.11)-(B.13). Before we were able to obtain any results for a non-self-interacting boson cloud we had first to solve a few initial obstacles to which the next section is dedicated to.

## 4.2 Initial obstacles

### 4.2.1 Degeneracy problems at the horizon

One of the first obstacles to overcome was the degeneracy problem at the horizon. A thorough description of this phenomenon is already covered in [38] but I will nonetheless describe the issue here. The degeneracy problem arises as one attempts to obtain numerical results of the bosonic 2p field profile. Accordingly one must add the decomposed Klein-Gordon equation and the boundary conditions for the field as well as the boundary conditions for the background fields, i.e.  $N, \Psi$  and  $\beta_i$ . The boundary conditions for the background fields at the horizon are the following [20]

$$4s^i\Psi^{-1}D_i\Psi + D_i s^i|_{\mathcal{S}} = -\Psi^2 A_{ij}s^i s^j, \quad (4.1a)$$

$$N|_{\mathcal{S}} = n_0, \quad (4.1b)$$

$$\beta^i|_{\mathcal{S}} = n_0\Psi^{-2}s^i + \Omega m^i. \quad (4.1c)$$

In this case,  $s^i$  is the normalized unit vector to the black hole horizon,  $\Omega$  is the black hole spin parameter and  $m^i$  the associated rotation vector. Now consider the decomposed Klein-Gordon equation in (B.1) and in particular zoom in on the 2<sup>nd</sup> order radial derivative term in the decomposed equation and the Lie derivative of the conjugate momentum

$$(\Psi^{-4} - (\beta^r/N)^2) D_r^2 \phi \quad (4.2)$$

From the boundary conditions of a non-rotating black hole,  $\Omega = 0$ , we have  $\beta^r|_{\mathcal{S}} = n_0/\Psi^2$  and  $N|_{\mathcal{S}} = n_0$ . Indeed, the 2<sup>nd</sup> order derivative terms vanish and the decomposed Klein-Gordon equation is thereby linear at the horizon. In other words the decomposed Klein-Gordon equation is degenerate at the horizon. Furthermore, one cannot put the equation as a boundary condition itself because the linearity of the equation would only result in the trivial solution  $\phi = 0$ .

The way to circumvent this problem is the goal of the aforementioned  $r_1$  domain depicted in Figure 3.1. With the small  $r_1$  domain we are able to demand  $\phi = 0$  everywhere inside  $r_1$  and consequently impose the boundary conditions a distance  $r_1$  away from the horizon. As a result, the 2<sup>nd</sup>-order derivative terms no longer vanish and the degeneracy problem at the horizon is evaded. In order to determine the size of  $r_1$ , I have performed a systematic study with the largest mass value<sup>1</sup> of  $\mu$  that can be achieved with the numerical code. One must also keep in mind not to make  $r_1$  too large, since that would cut off most of the field profile. I depict the systematic study in Figure 4.1.

From Figure 4.1 it is evident that for  $r_1 \in (2.1, 2.4)$  a physical 2p field profile that agrees well with the analytical solution (1.20) can be achieved. For lower values one may obtain nonphysical profiles with zero crossings. For this thesis,  $r_1 = 2.2$  became a 'working' domain size that was shown to produce valid results for all mass values and therefore all of the following results will have  $r_1 = 2.2$  unless otherwise stated.

<sup>1</sup>The largest mass value is considered because the peak moves closer to the horizon for larger  $\mu$ .

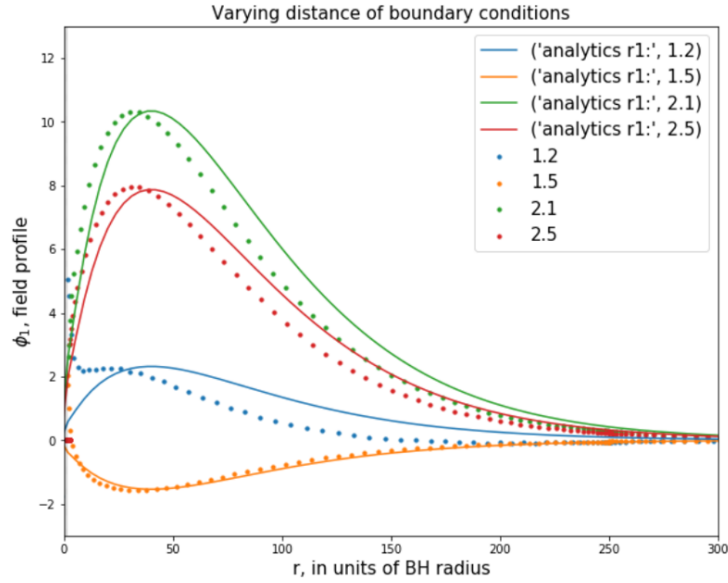


**Figure 4.1:** A systematic study for the size of  $r_1$  with a fixed mass value of  $\mu = 0.15$ ,  $r_2 = 250$ ,  $r_3 = 600$ .

#### 4.2.2 A resolution study

In numerical studies, one must ensure that the results produced are accurate and trustworthy. In the last section I showed a comparison between the numerical and analytical solution however, we must still convince ourselves that an appropriate resolution is used in each domain of the KADATH code. The following section is therefore dedicated to determining for which resolutions a convergent result is visible. In other words, for which resolutions do we obtain a physical  $2p$  field profile that does not change when increasing the resolution and consequently, which resolution is too low to obtain accurate results. The results are depicted in Figure 4.2. The rest of the results in this chapter have been obtained for  $r_2 = 65$  and  $r_3 = 55$  which as is evident from Figure 4.2 are sufficient domain resolutions.

As mentioned in the previous chapters, an advantage of spectral methods is their exponential convergence. Therefore, as an additional test of code robustness I consider the *mean absolute error* (MAE) of the conformal factor and the lapse function. The MAE is defined as the average of all absolute errors

$$\text{MAE} = \frac{1}{n} \sum_{i=1}^n |x_i - x| \quad (4.3)$$

where  $n$  is the number of errors and  $|x_i - x|$  the absolute error. The resolution in the  $r_2$  domain is key and I therefore only consider the MAE for the quantities in this domain. The MAE vs resolution in  $r_2$  is depicted for the lapse and conformal factor in Figure E.1 and E.2 respectively in Appendix E.

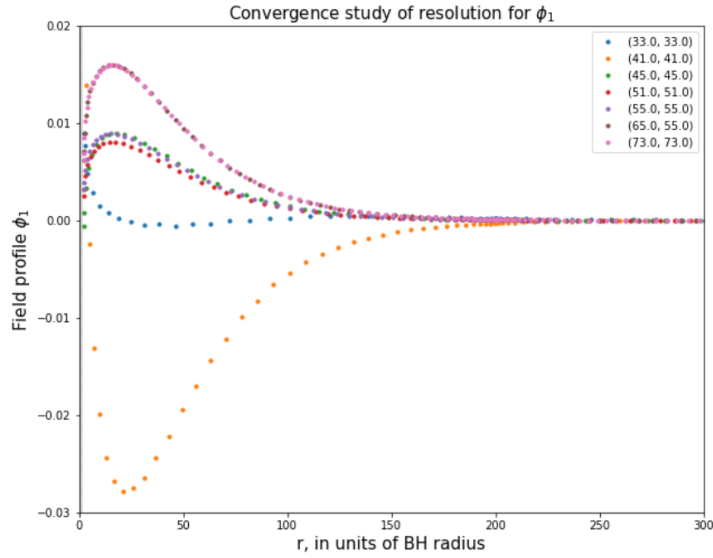


**Figure 4.2:** A convergence study of the resolution in the  $r_2$  and  $r_3$  domains which host most the cloud.

### 4.3 Bosonic field profile for a non-interacting scalar field

With the initial obstacles solved I will finally present the field profile of a free bosonic scalar field. All of the numerical solutions are for consistency obtained from the same domain sizes,  $r_1 = 2.2$ ,  $r_2 = 200$ ,  $r_3 = 450$ . Smaller mass values of the field require larger domain sizes since the cloud is less gravitationally bound to the black hole. Moreover, we know from previous work [11] that only  $\alpha \lesssim 0.4$  are physical. In our dimensionless units with  $R_{bh} = 2.0$  we thereby know that our largest mass value should be  $\mu = 0.20$ .

In Figure 4.3 I present the final results for the field profile of a free scalar field. These results are obtained for a systematically motivated  $r_1$  and an appropriate resolution as shown in the last section. The numerical solutions (dotted) are plotted with the analytical ones (solid), see Eq. (1.20). Note that asymptotically all the analytical and numerical solutions agree, which is to be expected since the cloud should asymptotically vanish far away from the black hole. Furthermore, note that for the small mass values, the analytical and numerical curves agree better at small  $r$ . This can be attributed to the fact that the analytical solutions were derived for a much smaller mass value,  $\alpha \lesssim 0.1$ , whereas the numerical solutions are for an arbitrary but physical mass value.

#### 4.3.1 Sensitivity to changes in the eigenfrequency

Before introducing self-interactions for the scalar field, we should examine how sensitive the eigenstate is to variations of the eigenfrequency. This will be helpful when introducing a self-interacting term in the scalar field equations since we will be aware of to which extent the eigenstate can be linearly perturbed. To this end, I fix a mass value, in this case  $\mu = 0.15$ , then add and subtract different percentage points of the eigenfrequency. In other words the perturbed eigenfrequency used for the numerical run is given by  $\omega_{per} = \omega + \Delta\omega$ .

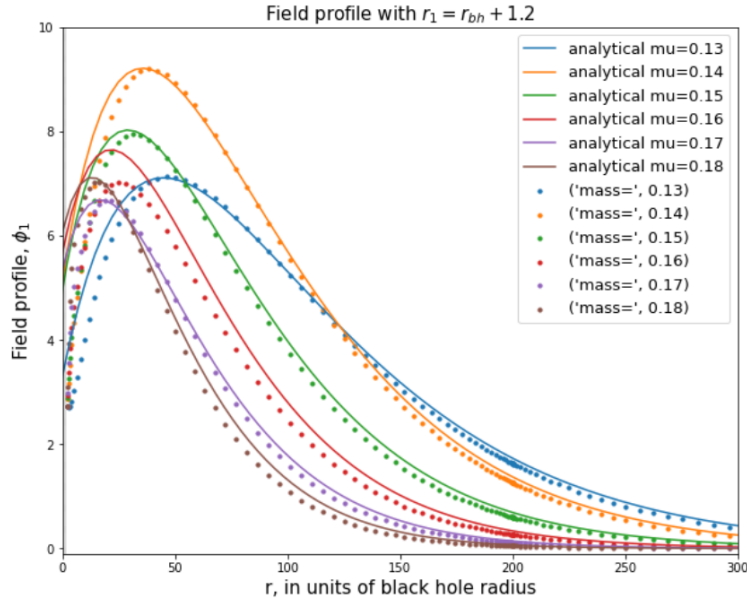


**Figure 4.3:** A comparison of the numerical solutions (dotted) with the analytical ones (solid) for different values of  $\mu$ . The domain used is of size  $r_1 = 1.2$ ,  $r_2 = 200$ ,  $r_3 = 450$ .

The result of the field profile with a perturbed eigenfrequency is shown in Fig. 4.4. It is evident that the eigenstate is indeed extremely sensitive to perturbations. Only for  $|\Delta\omega| = 10^{-5}$  does the profile resemble the unperturbed  $|\Delta\omega| = 0$  2p field profile. For  $\mu = 0.15$  we have the eigenfrequency  $\omega = 0.148096$  [?]. Therefore,  $|\Delta\omega| = 10^{-5}$  corresponds to only 0.7% of the eigenfrequency. We keep this sensitive in mind as we move on to consider self-interactions for the field.

#### 4.4 Boson field with self-interactions

With the numerical solution of a free field obtained, we may now take the next step in complexity and introduce a quartic self-interaction to the scalar field. The self-interaction for a scalar field was discussed in chapter 2 where our Lagrangian is now

$$\mathcal{L} = -\frac{1}{2}(D_\mu\varphi)(D^\mu\varphi) - \frac{1}{2}\mu^2\varphi^2 + \frac{1}{4!}\lambda\varphi^4. \quad (4.4)$$

resulting in the equation of motion

$$(D^2 - \mu^2)\varphi = -\frac{\lambda}{6}\varphi^3. \quad (4.5)$$

Adding the  $\lambda\varphi^3$  term to our Klein-Gordon equations (B.11)-(B.13) results in the code script in Appendix C.

The numerical setup is the same as in the previous sections. We utilize the same data for the Schwarzschild background and solve the field equations but now with the addition of  $\lambda\varphi^3$



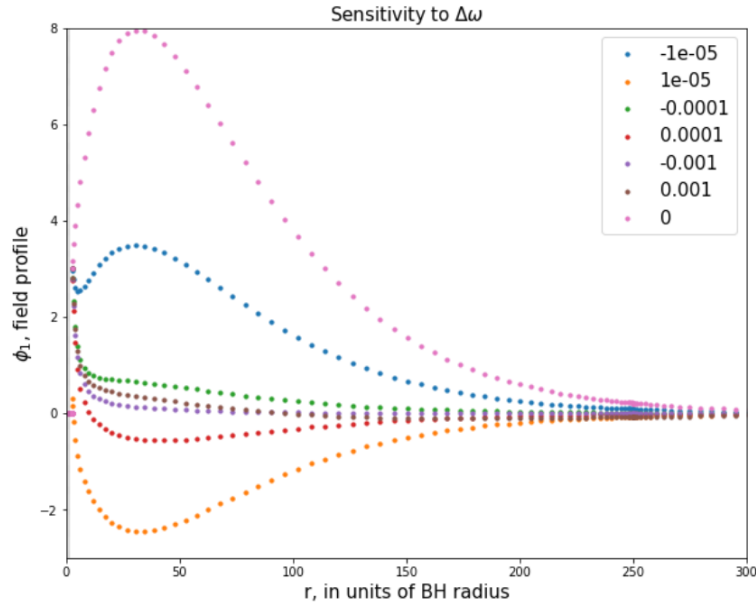


**Figure 4.4:** A study of the sensitivity to variations of the eigenfrequency  $\omega$ . The domain used is of size  $r_1 = 1.2$ ,  $r_2 = 200$ ,  $r_3 = 450$  and the boson mass fixed to  $\mu = 0.15$ .

in our equations of motion. From our previous study with variations of the eigenfrequency we expect the profile to be rather sensitive to the value of  $\lambda$ . Therefore, we vary  $\lambda$  from rather small values,  $|\lambda| = 10^{-5}$ , and look for a trend.

In Figure 4.5 I present the normalized energy density of the cloud. The reason for considering the energy density is simply because it is a gauge invariant quantity, see section 2.10. The field and thereby the energy density is normalized to make the results more well-defined. The black curve represents the non-interacting  $\lambda = 0$  case and the bluish points represent attractive self-interaction,  $|\lambda| < 0$ , whereas the yellowish points represent repulsive self-interactions,  $|\lambda| > 0$ . Note that the colour becomes darker for increasing  $|\lambda|$ . The new effect of self-interactions is clearly visible in Fig. 4.5. For the repulsive self-interactions,  $\lambda > 0$ , the curves are shifted to the right of the black curve, the larger the  $\lambda$  the greater the shift. For  $\lambda < 0$  the effect is the opposite, namely the curves are shifted to the left of the  $\lambda = 0$  curve and thereby closer to the black hole horizon. These new effects are rather intuitive. When the boson field is allowed attractive self-interactions, the cloud becomes more compact and as a consequence more gravitationally bound to the black hole. Therefore, the shift is directed towards the black hole horizon. When the boson field experiences repulsive self-interactions, the cloud is allowed to disperse to a greater extent and is thereby less gravitationally bound to the black hole. Therefore, the shift is directed away from the black hole horizon.

A clear deviation from the aforementioned trend is the  $\lambda = -0.001$  case. The dark blue  $\lambda = -0.001$  curve have shifted far above the black  $\lambda = 0$  curve. Similarly, the  $\lambda = 0.001$  also shows a great shift compared to the other repulsive cases. These great deviations indicate that we have reached a non-perturbative limit of our inclusion of self-interactions. As was shown

in the previous study, the eigenstate is sensitive even to small perturbations and for this non-perturbative limit of  $\lambda$  we cannot quantify the self-interaction effects. Nonetheless, the new effects visible in Figure 4.5 still have implications for small self-interactions.

At this stage the eigenfrequency is calculated outside of the KADATH code with the Mathematica notebook from [15]. A way to circumvent our computational limitations would be to include a code script that solves the eigenvalue problem and thereby computes the eigenfrequency itself. An investigation of how to include an eigenvalue solver in KADATH would be the next obvious step to probe a greater part of the parameter space.

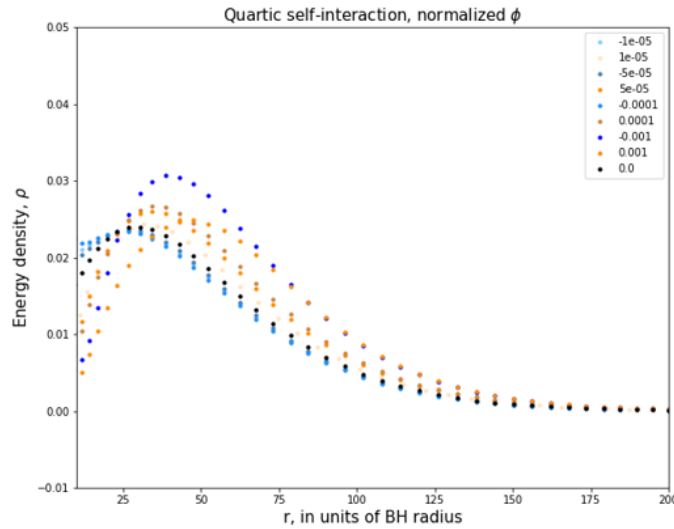


**Figure 4.5:** Normalized energy density for various values of  $\lambda$ . The mass has been fixed to  $\mu = 0.15$ .

## 4.5 Preliminary results of the backreaction

In the previous sections, the results have been computed assuming zero backreaction. In other words, we have solved for the black hole background and the boson cloud neglecting the effect of their mutual interaction. Thus in this section we will consider  $T_{\mu\nu} \neq 0$  and solve for the matter equations (B.3)-(B.7) in Appendix B.

Preferably, one would like to solve for the full backreaction. In that case, one would solve all of the field (B.11)-(B.13) and matter equations (B.3)-(B.7) simultaneously. However, as was discussed in Chapter 3, the size of the parameter space is strongly dependent on the number of fields that are solved for. When solving the full backreaction code one is solving for 4 fields (or 7 if  $\beta \neq 0$ ) rather than 2. Needless to say, the size of the system grows to be very large and even with a good initial guess the code would diverge.

To circumvent this problem we solve an effective and iterative version of the backreaction

by solving the equations in two steps:

1. Use the data of the background and free scalar field code and solve for the background given a fixed cloud.
2. Given the updated background solve for the scalar field.

From step 2, one can repeat step 1 with the updated field and background. However, one often finds that another iteration is unnecessary since the code was found to converge after step 2.

One last obstacle that must be discussed is the size of the cloud. Whether the code converges or not is dependent on what amplitude one inputs for the field. This effect is rather intuitive, the size of the cloud is dependent on the amplitude and mass of the boson field. A larger cloud should affect the background spacetime to a greater extent making it more difficult for the code to converge to a solution with the unperturbed background as initial data.

### 4.5.1 Results step 1: Solving for the background

In this first subsection I will present the result of backreaction for step 1 in the iteration process. I consider the backreaction of the background fields  $N$  and  $\Psi$  in (B.3)-(B.7) with a fixed non-self-interacting boson cloud surrounding the black hole. The mass of the boson is fixed to  $\mu = 0.18$  with an amplitude of  $A = 10^{-4}$  which was been found to be largest amplitude for which the code converges.

In Figure 4.6 I show the effect of backreaction on the lapse function,  $N$ . The effect of the backreaction on the lapse function has a physical and intuitive explanation. The lapse is the redshift factor [16], for  $N = 1$  one has zero redshift and the smaller the lapse, the greater the redshift. Because we are constrained to use a small amplitude of the scalar field, the effect of backreaction is small and mainly visible in the  $\Delta N = N_{after} - N_{before}$  plot. It is evident that the lapse is smaller for the backreaction case and  $\Delta N$  asymptotically vanishes, which is exactly what one would expect. The cloud increases the gravitational potential around the black hole and thereby the redshift. Hence the large dip in the plot of  $\Delta N$  for smaller  $r$ . Note that near the horizon the effect is not as large which can be attributed to the  $r_1$  domain where the cloud is zero everywhere. The cloud asymptotically approaches zero hence the vanishing  $\Delta N$  for large  $r$ , recall 2.71.

The effect of the backreaction on the conformal factor  $\Psi$  follows a similar pattern as the lapse and is visible in Figure 4.7. Here one would expect the backreaction to increase the value of  $\Psi$  since it asymptotically decreases to  $\Psi = 1$ , recall (2.71). This is exactly what is observed in the  $\Delta\Psi = \Psi_{after} - \Psi_{before}$  part of Figure 4.7. Naturally, due to the fact that we are restricted to small amplitudes, the effect of backreaction is rather small.

Recall from Section 2.10 that the ADM mass is a gauge invariant quantity which corresponds to the total energy of the system. When considering the effects of backreaction one would expect it to increase. In particular, for superradiance we know that the cloud should have a mass of 1% – 30% of the initial black hole mass. For the amplitude of  $A = 10^{-4}$  we find

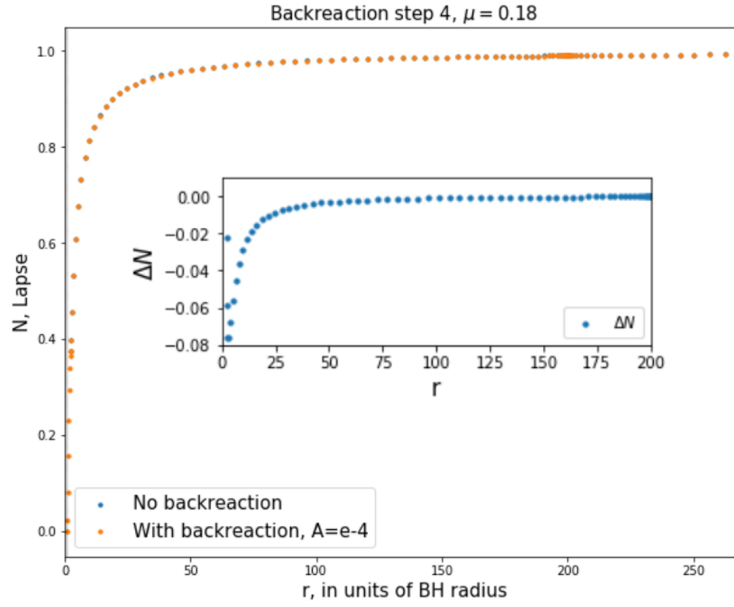


**Figure 4.6:** The lapse function with and without backreaction. The boson mass has been fixed to  $\mu = 0.18$  and the amplitude to  $A = 10^{-4}$ .

Amplitude	ADM before	ADM after	ADM after/ADM before
$1 \times 10^{-4}$	2.00364	2.01332	1.0048

In other words the mass of the cloud is 0.5% of the initial black hole mass which is on the borderline for what one would expect from superradiance growth.

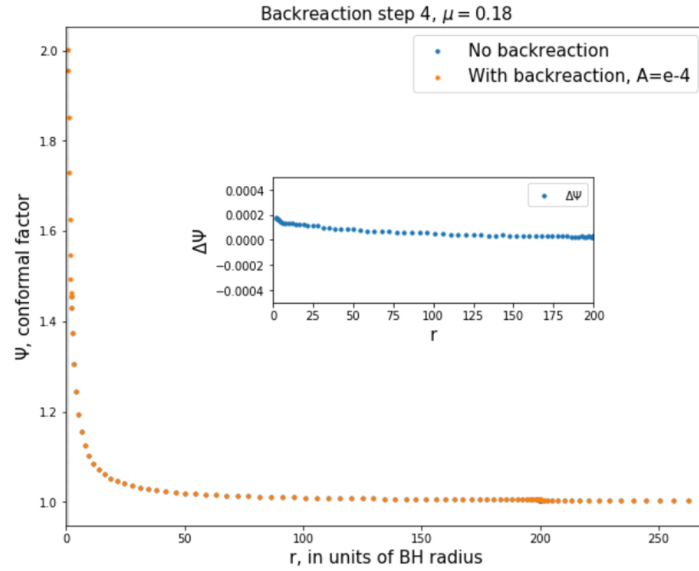


**Figure 4.7:** The conformal factor with and without backreaction. The boson mass has been fixed to  $\mu = 0.18$  and the amplitude to  $A = 10^{-4}$ .

### 4.5.2 Results step 2: Solving for the field

With the results for the backreaction on the spacetime quantities, we may now solve the scalar field on the updated background. In this section I will provide several results for backreaction with different field amplitudes. Note that each field have been solved on an updated background with the same field amplitude.

Figure 4.8 clearly illustrates how the amplitude of the field will affect the physical valid-

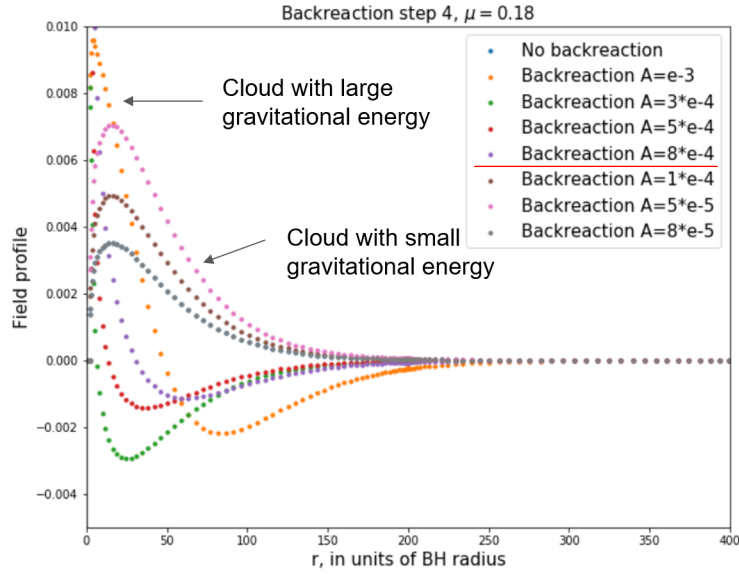


**Figure 4.8:** Normalized energy density for various values of  $\lambda$ . The mass has been fixed to  $\mu = 0.15$ .

ity of our result of the field profile. The red line in the legend separates the physical field profiles from the unphysical ones i.e. the ones that do not represent a 2p field profile. The fact that the field profile does not change significantly from the case of without backreaction is a reflection of the small gravitational energy of the cloud in these cases. This was also evident from the previous section where the  $A=e-4$  amplitude did not affect the background fields significantly.

If we turn to the larger amplitudes above the red line in the legend of Figure 4.8 it is evident that the field profile is altered. For these amplitudes a physical 2p state cannot be obtained with the backreacted background. The most notable result is the orange  $A=e-3$  curve. For this amplitude it seems as though the field has entered another eigenstate, namely a 3p state which is characterized by the two peaks visible in Fig. 4.8. Could it be that when backreaction is included, the effect is large enough to make the field go into a higher energy state? To understand this we must first discuss some limitations of this study.

The caveat of the results in Figure 4.8 is similar to what was found in section 4.3.1 and 4.4. The eigenstate is extremely sensitive to perturbations in the eigenfrequency and the eigenfrequency is not solved for in the KADATH code but rather calculated outside and used as input. Therefore,

what we see for the larger amplitudes in Fig. 4.8 does not reflect the actual physical state that the backreaction gives rise to. The deviation from the 2p state in these cases may simply be due to the fact that the eigenfrequency is too far off from the actual perturbed eigenstate. This sensitivity to perturbations may actually indicate that these systems are more complicated than what was first assumed and needless to say more work is needed to fully understand the effect of backreaction on boson clouds around black holes.

## 4.6 Preliminary results of backreaction with a self-interacting field

The results of backreaction with a self-interacting field are still ongoing and will be part of a published paper after the deadline of this thesis have passed. Nonetheless, I will present some preliminary results of this investigation and explain the subtleties that are still being analyzed.

From backreaction with self-interactions one would expect that attractive interactions ( $\lambda < 0$ ) should break down before repulsive interactions ( $\lambda > 0$ ). Since attractive interactions would shift the energy density towards the black hole horizon, as we saw in section 4.4, they affect the cloud in a similar fashion as the backreaction i.e. provide a greater gravitational potential. Therefore, one would expect the repulsive interactions ( $\lambda > 0$ ) to provide an 'antidote' to the backreaction since it will shift the energy density away from the black hole horizon. Hopefully, the repulsive interactions may even provide us with an opportunity to obtain a convergent backreaction code with a larger field amplitude than  $A = 10^{-4}$ .

The setup for the numerical runs are the same as in the previous section. We fix the mass to

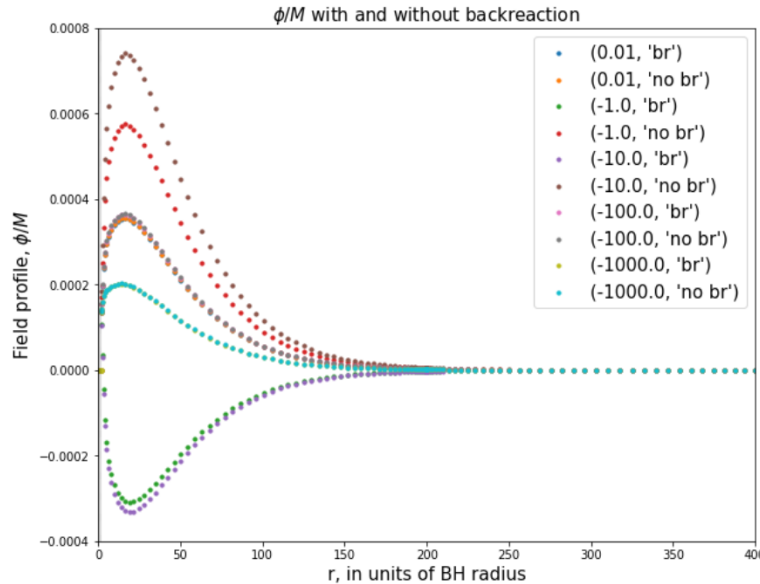


**Figure 4.9:** Field profiles of  $\phi/M$  for backreaction and without backreaction for various values  $\lambda$ . The mass has been fixed to  $\mu = 0.18$  and amplitude  $A = 10^{-4}$ .

$\mu = 0.18$  and amplitude to  $A = 10^{-4}$ . In Figure 4.9 I present the results the field profiles with

backreaction effects (i.e. step 4) and compare them to the field profiles without backreaction for various values of  $\lambda$ . In contradiction to what one would expect, the repulsive interactions break down earlier than the attractive ones. The largest repulsive  $\lambda$  that could be obtained was  $\lambda = 0.01$ . In Figure 4.9 the field profiles of  $\lambda = 0.01$  with and without backreaction overlap i.e. the effect of backreaction is very small and I do not present any results of lower values of repulsive  $\lambda$ . On the other hand, we are able to produce several higher order of magnitudes for  $\lambda < 0$ <sup>2</sup>. Even more contradictory is that larger values seem to be less affected by backreaction effects. Furthermore, for  $\lambda = -1, -10$  the field profiles will flip their sign and even cross zero, see Fig. 4.9.

The contradictory results of Figure 4.9 must be thoroughly investigated before we are able to compare the changes to the lapse  $N$  and conformal factor  $\Psi$ , as was done in the previous section. Perhaps the most obvious source of error come from the definition of the matter equations (2.67). When obtaining the results in Figure 4.9 only the Klein-Gordon equations were altered to their self-interacting counterpart. The matter equations were kept in the same form as in equation (2.67). However, the energy-momentum tensor for a self-interacting scalar field should be along the lines of

$$T_{\mu\nu} = \nabla_\mu\phi\nabla_\nu\phi^* + \nabla_\nu\phi\nabla_\mu\phi^* - g_{\mu\nu} \left( g^{\alpha\beta}\nabla_\alpha\phi\nabla_\beta\phi^* + \mu^2\phi^*\phi + \frac{1}{2}\lambda(\phi^*\phi)^4 \right). \quad (4.6)$$

Thus, we expect the matter variables to also reflect the presence of a self-interaction term. The results of backreaction with self-interactions with the altered matter variables have yet to be conducted. They are part of an ongoing paper and will be produced after the deadline of this thesis have passed.

---

<sup>2</sup>The reason we can probe values as large as  $\lambda = -1000$  is because the amplitude is very small in these studies.

## Chapter 5

# Conclusions

The purpose of this thesis was to study the effect of boson clouds around black holes with numerical relativity. Consequently, the work also serves as a stepping stone to future studies on binary black holes and boson clouds. We have identified and solved obstacles such as the degeneracy problem at the horizon in order to achieve numerical solutions of the free boson field profile. To this end we have also investigated the necessary resolution in each domain and the robustness of our code. Step by step we have increased the complexity of our studies by the inclusion of self-interactions and possibility of backreaction effects.

In all of our studies we have utilized the spectral solver `KADATH` to numerically solve the decomposed Einstein field equations and the Klein-Gordon equations. In order to obtain a numerical solution of the bosonic  $2p$  field profile we had first to solve the degeneracy problem at the horizon. To avoid a degenerate wave function we put the field to zero inside a small domain around the black hole and impose the boundary conditions outside of this small domain. From a systematic study, we found an appropriate size of the small domain which solves the degeneracy problem and produces an accurate  $2p$  field profile. In the same fashion, we performed a convergence study to ensure that the correct resolution was implemented in each domain. With the solution of the degeneracy problem and tests of the code robustness, we could finally obtain a proper numerical result of the bosonic  $2p$  field profile for masses in the range of  $\mu \in \{0.13, 0.20\}$ .

With the results of a free field, we considered the effect of adding self-interactions. For small values of the coupling constant  $\lambda$  there was an intuitive effect of the inclusion of self-interactions. For attractive interactions, the cloud experienced a shift towards the black hole horizon and a shift away from the horizon for repulsive ones. The influence of the self-interactions seem natural since attractive interactions would make the cloud more compact and gravitationally bound to the black hole horizon and vice versa for repulsive interactions. In addition, we also noticed a break down in the aforementioned trend for  $|\lambda| = 0.001$ . For these values and higher of  $\lambda$  the eigenstate is no longer linearly perturbed and we are limited in our knowledge of eigenfrequency. Nonetheless, the results presented in this thesis are still valid for small values of  $\lambda$  and with more work could be useful for continuous gravitational wave searches.



Finally, we show some preliminary results of boson clouds around black holes when considering backreaction effects for both free and self-interacting boson fields. The finalized results of the effect of backreaction for self-interacting fields are still in the making. They will be in a paper published after the deadline of this thesis has passed and due to the size of the parameter space that is to be explored will not be included.

The next natural step would be to try and include an eigenvalue problem solver in our current KADATH code. With this in place one would be able to obtain the physically accurate field profile for inclusions of self-interaction and backreaction effects. Secondly, even with our current limitations one could still use our results as initial data and perform a full numerical relativity simulations. With the time-dependence involved, one could perhaps see effects of the Bosenova in the case of attractive self-interactions. Hopefully, these results would provide an approach to more accurately determine the size of the continuous gravitational waves emitted from the cloud.

A final investigation that is yet to be conducted is a numerical run of the backreaction but with  $\beta \neq 0$ . When backreaction is allowed for one would expect to see an effect of frame-dragging in the  $\phi$  component of  $\beta$ . Frame-dragging is a predicted phenomena in General Relativity in which a rotating object *drags* space around it such that a smaller orbiting object will align its rotational axis towards the larger rotating object, hence the effect of a non-zero shift vector  $\beta$ . A few runs with  $\beta$  allowed as a variable have been tested for here however, since  $\beta$  is a vector it contributes to the parameter space as three fields which greatly increases the size of the system. A solution may be to only solve for one of the components whilst keeping two fixed but this is rather non-trivial and the final results of frame-dragging effects for  $\beta$  have yet to be obtained.

In the work presented here we have only considered *scalar* bosons and an extension of this project could very well involve a numerical investigation of *vector* bosons. A numerical study of the superradiant growth and saturation was done in [40] but excluded self-interactions and backreaction effects. Vector bosons would be of interested numerically since the  $1s$  energy state would be physically motivated. The  $1s$  state is simpler to obtain numerically and we may therefore avoid some of the numerical subtleties and limitations that we have encountered in the scalar case.

In addition to investigations of boson clouds around *single* black holes the ultimate goal would be to study boson clouds around binary black holes. The work conducted in this thesis can be seen as a stepping stone towards a numerical investigation of the binary case. In particular, it would be interesting to study the level transitions induced by the gravitational perturbation of a binary black hole companion, as discussed in [11]. The numerical relativity investigation of these systems would be crucial to make predictions about the gravitational wave signals from the cloud which would in turn provide constraints on ultralight bosons and probe physics beyond the standard model.

# Appendices

## Appendix A

## Appendix A

In this appendix some of the geometric equations relevant for the 3+1 formalism will be derived. An important part of the formalism that we left out is the decomposition of the spacetime Riemann tensor,  ${}^4R$ . The first equation we will cite is the **Gauss equation** which is the fully projected part of the Riemann tensor in other words  $\gamma_{\mu\nu}{}^4R$ :

$$\gamma_{\alpha}^{\mu}\gamma_{\beta}^{\nu}\gamma_{\rho}^{\gamma}\gamma_{\delta}^{\sigma}{}^4R_{\sigma\mu\nu}^{\rho} = R_{\delta\alpha\beta}^{\gamma} + K_{\alpha}^{\gamma}K_{\delta\beta} - K_{\beta}^{\gamma}K_{\alpha\delta}.$$

(A.1)

For future use we shall also present the **contracted Gauss equation**. It's obtained by contracting (A) with the indices  $\gamma$  and  $\alpha$  and use the fact that  $\gamma_{\alpha}^{\mu}\gamma_{\rho}^{\alpha} = \gamma_{\rho}^{\mu} = \delta_{\rho}^{\mu} + n^{\nu}n_{\rho}$ . This results in an expression in which the Ricci tensors  ${}^4\mathbf{R}$  and  $\mathbf{R}$ , associated with  $\mathbf{g}$  and  $\gamma$  respectively, appears:

$$\gamma_{\alpha}^{\mu}\gamma_{\beta}^{\nu}{}^4R_{\mu\nu} + \gamma_{\mu\alpha}n^{\nu}\gamma_{\beta}^{\rho}n^{\sigma}{}^4R_{\nu\rho\sigma}^{\mu} = R_{\alpha\beta} + KK_{\alpha\beta} - K_{\alpha\mu}K_{\beta}^{\mu}.$$

(A.2)

The second important result we need is the **Codazzi equation** which stems from the projection of the Riemann tensor three times onto  $\Sigma_t$  and once along the normal  $\mathbf{n}$ , yielding

$$\gamma_{\rho}^{\mu}n^{\sigma}\gamma_{\alpha}^{\mu}\gamma_{\beta}^{\nu}{}^4R_{\sigma\mu\nu}^{\rho} = D_{\beta}K_{\alpha}^{\gamma} - D_{\alpha}K_{\beta}^{\gamma}.$$

(A.3)

The final puzzle piece in our 3+1 decomposition of the Riemann tensor is the so called the **Ricci equation** which we present below:

$$\gamma_{\mu\alpha}n^{\rho}\gamma_{\sigma}^{\nu}{}^4R_{\rho\nu\sigma}^{\mu} = \frac{1}{N}\mathcal{L}_{\mathbf{m}}K_{\alpha\beta} + \frac{1}{N}D_{\alpha}D_{\beta}N + K_{\alpha\mu}K_{\beta}^{\mu}.$$

(A.4)

Eq. (A.4), together with the Gauss (A) and Codazzi (A.3) equation, complete the 3+1 decomposition of the spacetime Riemann tensor.

Notice that the left-hand side of the Ricci equation contains a term found in the contracted

Gauss equation (A.2). By combining the two one ends up with a formula which only contains the Ricci tensor and not the spacetime Riemann tensor,

$$\boxed{\gamma_{\alpha}^{\mu}\gamma_{\beta}^{\nu}R_{\mu\nu} = -\frac{1}{N}\mathcal{L}_{\mathbf{m}}K_{\alpha\beta} + \frac{1}{N}D_{\alpha}D_{\beta}N + R_{\alpha\beta} + KK_{\alpha\beta} + 2K_{\alpha\mu}K_{\beta}^{\mu}} \quad (\text{A.5})$$

alternatively in index-free notation,

$$\boxed{\tilde{\gamma}^{*4}\mathbf{R} = -\frac{1}{N}\mathcal{L}_{\mathbf{m}}\mathbf{K} - \frac{1}{N}\mathbf{D}\mathbf{D}N + \mathbf{R} + K\mathbf{K} - 2\mathbf{K} \cdot \vec{\mathbf{K}}} \quad (\text{A.6})$$

### A.0.1 Conformal decomposition of various quantities

For covariant derivatives with lower indices, the conformal decomposition is equal to the regular derivative i.e.  $D_i\chi = \tilde{D}_i\chi$ , where  $\chi$  is some arbitrary scalar field. For upper indices however we have

$$\tilde{D}^i\chi = \gamma^{ki}\tilde{D}_k\chi = \Psi^{-4}\tilde{D}^i\chi \quad (\text{A.7})$$

The relation between the regular and conformal Ricci scalar is given by

$${}^3R = {}^3\tilde{R}\Psi^{-4} - 8\Psi^{-5}\tilde{\gamma}^{ij}\tilde{D}_i\tilde{D}_j\Psi \quad (\text{A.8})$$

### A.0.2 Lie derivatives

The Lie derivative of a vector  $v^{\mu}$  along another vector  $X^{\mu}$ , reads

$$\mathcal{L}_X v^{\mu} = [X, v^{\mu}] \quad (\text{A.9})$$

# Appendix B

## Appendix B

In this appendix I summarize the relevant field equations that are solved in the Kadath code. They will be referred to in other parts of the thesis, most notably in Chapter 5. Although it might be used as a reference for future work. All of this can be found in [38].

### B.1 Scalar field equations

#### Klein-Gordon equations

$$\frac{\Psi^{-4}}{N} \tilde{D}_i N \tilde{D}^i \phi + \Psi^{-4} \tilde{D}_i \tilde{D}^i \phi + 2\Psi^{-5} \tilde{D}_i \phi \tilde{D}^i \Psi + 2\mathcal{L}_n \Pi - \mu^2 \phi = 0, \quad +c.c \quad (\text{B.1})$$

where,

$$\mathcal{L}_n \Pi = \frac{1}{2N^2} [2\Pi\beta^j \partial_j N - 2i\omega\beta^i \partial_i \phi + \omega^2 \phi - \beta^i \beta^j \partial_i \partial_j \phi - \beta^i (\partial_i \beta^j) \partial_j \phi]. \quad (\text{B.2})$$

### B.2 Background

#### The Hamiltonian constraint

$$\tilde{D}_i \tilde{D}^i \Psi + \frac{1}{8} A_{ij} A^{ij} \Psi^5 = 2\pi\rho\Psi^5 \quad (\text{B.3})$$

with  $\rho$  being the energy density

$$\rho = 4\Pi\Pi^* + \mu^2 \phi\phi^* + \Psi^{-4} \partial_i \phi \partial \phi^*. \quad (\text{B.4})$$

#### The momentum constraint

$$\tilde{D}_j A^{ij} + 10A^{ij} \tilde{D}_j \ln\Psi = 8\pi j^i \quad (\text{B.5})$$

where

$$j^i = 2\Psi^{-4} (\Pi^* \partial^i \phi + \Pi \partial \phi^*). \quad (\text{B.6})$$

#### The XCTS equation

$$\tilde{D}_i \tilde{D}^i N = N\Psi^4 [4\pi(\rho + S) + A_{ij} A^{ij}] - 2\tilde{D}_i N \tilde{D}^i \ln\Psi \quad (\text{B.7})$$

where

$$(\rho + S) = 16\Pi\Pi^* - 2\mu^2\phi\phi^* \quad (\text{B.8})$$

### B.3 Imaginary fields

From quantum mechanics, we know that an arbitrary complex scalar field  $\psi$  may be written in terms of two real scalar fields

$$\psi = \frac{1}{\sqrt{2}}(\psi_1 + i\psi_2), \quad \psi^* = \frac{1}{\sqrt{2}}(\psi_1 - i\psi_2) \quad (\text{B.9})$$

and equivalently

$$\psi_1 = \frac{\sqrt{2}}{2}(\psi + i\psi^*), \quad \psi_2 = -\frac{i\sqrt{2}}{2}(\psi - i\psi^*) \quad (\text{B.10})$$

Therefore, we may also write our complex scalar field in terms of two real fields and by means of adding and subtracting the Klein-Gordon equation (B.1) and its complex conjugate. When adding (B.1) and its complex conjugate one finds [38]

$$\frac{\Psi^{-4}}{N}\tilde{D}_i N \tilde{D}^i \phi_1 + \Psi^{-4}\tilde{D}_i \tilde{D}^i \phi_1 + 2\Psi^{-5}\tilde{D}_i \phi_1 \tilde{D}^i \Psi + 2\mathcal{L}_n \Pi_1 - \mu^2 \phi_1 = 0 \quad (\text{B.11})$$

where

$$\mathcal{L}_n \Pi_1 = \frac{1}{2N^2} [2\Pi_1 \beta^j \partial_j N - 2i\omega \beta^i \partial_i \phi_1 + \omega^2 \phi_1 - \beta^i \beta^j \partial_i \partial_j \phi_1 - \beta^i (\partial_i \beta^j) \partial_j \phi_1]. \quad (\text{B.12})$$

Similarly, when subtracting (B.1) and its complex conjugate one finds

$$\frac{\Psi^{-4}}{N}\tilde{D}_i N \tilde{D}^i \phi_2 + \Psi^{-4}\tilde{D}_i \tilde{D}^i \phi_2 + 2\Psi^{-5}\tilde{D}_i \phi_2 \tilde{D}^i \Psi + 2\mathcal{L}_n \Pi_2 - \mu^2 \phi_2 = 0 \quad (\text{B.13})$$

where

$$\mathcal{L}_n \Pi_2 = \frac{1}{2N^2} [2\Pi_2 \beta^j \partial_j N - 2i\omega \beta^i \partial_i \phi_2 + \omega^2 \phi_2 - \beta^i \beta^j \partial_i \partial_j \phi_2 - \beta^i (\partial_i \beta^j) \partial_j \phi_2]. \quad (\text{B.14})$$

The real parts of the canonical momentum,  $\Pi_1$  and  $\Pi_2$ , are obtained from the canonical momentum  $\Pi$  via (B.10). Recall the expression for the canonical momentum in (??). The expression for  $\Pi_1$  and  $\Pi_2$  have already been derived in [38] and I only present their final form here

$$\Pi_1 = \frac{1}{2N}(\beta^i \partial_i \phi_1 - \omega \phi_2), \quad \Pi_2 = -\frac{1}{2N}(\beta^i \partial_i \phi_2 - \omega \phi_1). \quad (\text{B.15})$$

#### B.3.1 Matter equations

With the introduction of the real fields  $\phi_1, \phi_2$  and  $\Pi_1, \Pi_2$  the energy density defined in (??) can be written in terms of real fields

$$\begin{aligned} \rho &= 4\Pi\Pi^* + \mu^2\phi\phi^* + \partial_i \phi \partial^i \phi^* \\ &= 2(\Pi_1 \Pi_1 + \Pi_2 \Pi_2) + \frac{\mu^2}{2}(\phi_1 \phi_1 + \phi_2 \phi_2) + \frac{1}{2}(\partial_i \phi_1 \partial^i \phi_1 + \partial_i \phi_2 \partial^i \phi_2) \end{aligned} \quad (\text{B.16})$$

Similarly one can find the momentum density (B.6) in terms of real fields as

$$\boxed{j^i = \frac{1}{N}(\beta^k \partial_k \phi_1 \partial_i \phi_1 - \omega \phi_2 \partial_i \phi_1 + \beta^k \partial_k \phi_2 \partial_i \phi_1 - \omega \phi_1 \partial_i \phi_2)}. \quad (\text{B.17})$$

Lastly,  $(\rho + S)$  in the XCTS equation (B.7) as

$$\boxed{(\rho + S) = 8 (\Pi_1^2 \Pi_2^2) - \mu^2 (\phi_1^2 + \phi_2^2)}. \quad (\text{B.18})$$

## Appendix C

# Appendix C

### Numerical code for a scalar field with self-interactions

```
#include "kadath_spheric.hpp"
#include "mpi.h"

using namespace Kadath ;
int main (int argc, char** argv) {

    int rc = MPI_Init(&argc, &argv) ;
    int rank = 0 ;
    MPI_Comm_rank(MPI_COMM_WORLD, &rank) ;

    if (argc <2) {
        cout <<"File_missing..." << endl ;
        abort() ;
    }

    // scalar field amplitude
    double A = 0.0001 ; //0.0003 ;

    int r2_res, r3_res ;
    double r0, r1, r2, r3 ;
    double t, ome ;

    double mu = 0.18 ;
    double freq = 0.1764379644998751 ; // mu = 0.18

    char* name_fich = argv[1] ;
    FILE* fich = fopen(name_fich, "r") ;
```



```

Space_spheric space (fich) ;
fread_be (&r2_res, sizeof(int), 1, fich) ;
fread_be (&r3_res, sizeof(int), 1, fich) ;
fread_be (&r0, sizeof(double), 1, fich) ;
fread_be (&r1, sizeof(double), 1, fich) ;
fread_be (&r2, sizeof(double), 1, fich) ;
fread_be (&r3, sizeof(double), 1, fich) ;
fread_be (&t, sizeof(double), 1, fich) ;
fread_be (&ome, sizeof(double), 1, fich) ;

Scalar conf (space, fich) ;
Scalar lapse (space, fich) ;
Vector shift (space, fich) ;
fclose(fich) ;

if (rank==0) {
  cout << "cloud_2p" << endl ;
  cout << "reading_success" << endl ;
  cout << "r2_res=" << r2_res << endl ;
  cout << "r3_res=" << r3_res << endl ;
  cout << "r0=" << r0 << endl ;
  cout << "r1=" << r1 << endl ;
  cout << "r2=" << r2 << endl ;
  cout << "t=" << t << endl ;
  cout << "ome=" << ome << endl ;
  cout << "mu=" << mu << endl ;
  cout << "freq=" << freq << endl ;
  cout << "A=" << A << endl ;
  cout << "lambda=" << lambda << endl ;

  int ndom = space.get_nbr_domains() ;
  if (rank==0) { cout << "ndom=" << ndom << endl ; }

  // Computation adm mass :
  Val_domain integ_adm (conf(ndom-1).der_r()) ;
  double adm = -space.get_domain(ndom-1)->integ(integ_adm, OUTER_BC)/2/M_PI ;
  if (rank==0) { cout << "adm_mass=" << adm << endl ; }

  double a = adm * mu ;
  if (rank==0) {
    cout << "alpha=" << a << endl ;
    cout << "freq=" << freq << endl ;
  }
}

```

```

int r = r0 ;

Scalar field1 (space) ;
field1.set_domain(0) = 0 ;

Scalar field2 (space) ;
field2.set_domain(0) = 0 ;

for (int d=1; d<=(ndom-1) ; d++) {
    Val_domain rr = space.get_domain(d)->get_radius() ;
    rr.std_base_r_spher() ;
    // convert to harmonic coordinates
    Val_domain rh = rr + 1/(16*rr) + 0.5 ;
    field1.set_domain(d) = A*rh.mult_cos_phi().mult_sin_theta() ;
    field2.set_domain(d) = A*rh.mult_sin_phi().mult_sin_theta() ;
}
field1.set_domain(ndom-1) = 0. ;
field1.set_domain(ndom-1) = 0. ;
field1.std_base() ;
field2.std_base() ;

Scalar p1 = field1 ;
Scalar p2 = field2 ;

Base_tensor basis (shift.get_basis()) ;
Metric_flat fmet (space, basis) ;
System_of_eqs syst (space, 2, 3) ;

// Unknown
syst.add_var ("ph1", field1) ;
syst.add_var ("ph2", field2) ;

syst.add_cst ("p1", p1) ;
syst.add_cst ("p2", p2) ;

// constants
syst.add_cst ("lam", lambda) ;
syst.add_cst ("mu", mu) ;
syst.add_cst ("Psi", conf) ;
syst.add_cst ("N", lapse) ;
syst.add_cst ("bet", shift) ;
syst.add_cst ("freq", freq) ;

```

```

// Metric :
fmet.set_system (syst , "f" ) ;

// Defenitions of momenta for n_0 = 0.0
syst.add_def ("LP1=(N*freq*bet^i*D_i_ph2)+(N*freq*freq*ph1)/2") ;

// Inner BC sphere minus
space.add_inner_bc (syst , "ph1=p1" ) ;
space.add_inner_bc (syst , "ph2=p2" ) ;

// Outer BC
space.add_outer_bc (syst , "ph1=0." ) ;
space.add_outer_bc (syst , "ph2=0." ) ;

// for n_0 = 0.0
space.add_eq (syst , "N^2*D_i*N*D^i_ph1/Psi^4+N^3*D_i*D^i_ph1/Psi^4") ;
bool endloop = false ;
int ite = 1 ;
double conv ;

while (!endloop) {
    endloop = syst.do_newton(1e-8, conv) ;
    if (rank==0) {
        cout << "Newton_iteration_" << ite << "_" << conv << endl ;
    }
    ite++ ;
}

// Output
if (rank==0) {
    char name[100] ;
    sprintf (name, "schwField_2p_smallA4_%d_%d_%.1f_%.0f_%.0f_%.2f_lam%.",
    FILE* fich = fopen(name, "w") ;
    space.save(fich) ;
    fwrite_be (&r2_res, sizeof(int), 1, fich) ;
    fwrite_be (&r3_res, sizeof(int), 1, fich) ;
    fwrite_be (&r0, sizeof(double), 1, fich) ;
    fwrite_be (&r1, sizeof(double), 1, fich) ;
    fwrite_be (&r2, sizeof(double), 1, fich) ;
    fwrite_be (&r3, sizeof(double), 1, fich) ;
    fwrite_be (&t, sizeof(double), 1, fich) ;
    fwrite_be (&ome, sizeof(double), 1, fich) ;
    fwrite_be (&freq, sizeof(double), 1, fich) ;
}

```

```

        fwrite_be (&mu, sizeof(double), 1, fich) ;
        fwrite_be (&lambda, sizeof(double), 1, fich);
        conf.save(fich) ;
        lapse.save(fich) ;
        shift.save(fich) ;
        field1.save(fich) ;
        field2.save(fich) ;
        fclose(fich) ;
    }

    MPI_Finalize() ;

    return EXIT_SUCCESS ;
}

```

## The full backreaction code for a free field

```

#include "kadath_spheric.hpp"
#include "mpi.h"

using namespace Kadath ;
int main (int argc, char** argv) {

    int rc = MPI_Init(&argc, &argv) ;
    int rank = 0 ;
    MPI_Comm_rank(MPI_COMM_WORLD, &rank) ;

    if (argc <2) {
        cout <<"File_missing..." << endl ;
        abort() ;
    }

    int r2_res, r3_res ;
    double r0, r1, r2, r3 ;
    double t, ome ;

    // field values
    double mu, freq ;

    char* name_fich = argv[1] ;
    FILE* fich = fopen(name_fich, "r") ;

    Space_spheric space (fich) ;

```

```

fread_be (&r2_res, sizeof(int), 1, fich) ;
fread_be (&r3_res, sizeof(int), 1, fich) ;
fread_be (&r0, sizeof(double), 1, fich) ;
fread_be (&r1, sizeof(double), 1, fich) ;
fread_be (&r2, sizeof(double), 1, fich) ;
fread_be (&r3, sizeof(double), 1, fich) ;
fread_be (&t, sizeof(double), 1, fich) ;
fread_be (&ome, sizeof(double), 1, fich) ;
fread_be (&freq, sizeof(double), 1, fich) ;
fread_be (&mu, sizeof(double), 1, fich) ;

```

```

Scalar lapse (space, fich) ;
Vector shift (space, fich) ;
Scalar field1 (space, fich) ;
Scalar field2 (space, fich) ;
fclose(fich) ;

```

```

if (rank==0) {
    cout << "Backreaction_for_cloud_2p_with_variable_shift" << endl ;
    cout << "reading_success" << endl ;
    cout << "r2_res=" << r2_res << endl ;
    cout << "r3_res=" << r3_res << endl ;
    cout << "r0=" << r0 << endl ;
    cout << "r1=" << r1 << endl ;
    cout << "r2=" << r2 << endl ;
    cout << "t=" << t << endl ;
    cout << "ome=" << ome << endl ;
    cout << "mu=" << mu << endl ;
    cout << "freq=" << freq << endl ;
}

```

```

int ndom = space.get_nbr_domains() ;
Base_tensor basis (shift.get_basis()) ;
Metric_flat fmet (space, basis) ;

```

```

// Computation adm mass before backreaction :

```

```

Val_domain integ_adm_init (conf(ndom-1).der_r()) ;

```

```

double adm_init = -space.get_domain(ndom-1)->integ(integ_adm_init, OUTER_BC)/2/M

```

```

// Vector parallel to the sphere (needed only for inner BC)

```

```

Vector mm (space, CON, basis) ;

```

```

for (int i=1 ; i<=3 ; i++)

```

```

    mm.set(i) = 0. ;

```

```

Val_domain xx (space.get_domain(1)->get_cart(1)) ;

```

```

Val_domain yy (space.get_domain(1)->get_cart(2)) ;
mm.set(3).set_domain(1) = sqrt(xx*xx + yy*yy) ;
mm.std_base() ;

```

```

// Normal to sphere BH1 :
Vector n (space, COV, basis) ;
n.set(1) = 1. ;
n.set(2) = 0. ;
n.set(3) = 0. ;
n.std_base() ;

```

```

// copy fields for inner boundary values
Scalar p1 = field1 ;
Scalar p2 = field2 ;

```

```

field1.set_domain(1).annule_hard() ;
field2.set_domain(1).annule_hard() ;

```

```

System_of_eqs syst (space, 1, ndom-1) ;

```

```

// Metric :
fmet.set_system (syst, "f") ;

```

```

// fields to solve
syst.add_var("Psi", conf) ;
syst.add_var("N", lapse) ;
syst.add_var("ph1", field1) ;
syst.add_var("ph2", field2) ;

```

```

// One user defined constant
syst.add_cst("ph1", field1) ;
syst.add_cst("ph2", field2) ;
syst.add_cst("bet", shift) ;
syst.add_cst("r", r0) ;
syst.add_cst("t", t) ;
syst.add_cst("n", n) ;
syst.add_cst("ome", ome) ;
syst.add_cst("m", mm) ;
syst.add_cst("mu", mu) ;
syst.add_cst("frq", freq) ;
syst.add_cst("pi", M_PI) ;
// inner boundary values (double)
syst.add_cst("p1", p1) ;
syst.add_cst("p2", p2) ;

```

```

// Definition of the extrinsic curvature
syst.add_def("A^ij=(D^i_beta^j+D^j_beta^i-(2./3.)*D_kbet^k*f^ij)/(2.*N)");
syst.add_def ("nn^i=nn^i/sqrt(n_i*nn^i)");

// definitions of momenta
syst.add_def ("LP1=(N*frq*bet^i*D_i_ph2)+(N*frq*frq*ph1)/2
- (N*bet^i*bet^j*D_i_D_j_ph1)/2-(N*bet^i*bet^j*D_j_ph1)/2
+ (bet^i*D_i_ph1*bet^j*D_j_N)/2-(frq*ph2*bet^i*D_i_N)/2" );
syst.add_def ("LP2=(N*frq*bet^i*D_i_ph1)+(N*frq*frq*ph2)/2
- (N*bet^i*bet^j*D_i_D_j_ph2)/2-(N*bet^i*bet^j*D_j_ph2)/2
+ (bet^i*D_i_ph2*bet^j*D_j_N)/2-(frq*ph1*bet^i*D_i_N)/2" );

// definitions of the matter equations
syst.add_def ("rho=(frq^2/N^2+mu^2)*(ph1^2+ph2^2)/2
+(D_i_ph1*D^i_ph1+D_i_ph2*D^i_ph2)/2" );
syst.add_def ("mom^i=frq*(ph2*D^i_ph1-ph1*D^i_ph2)/N" );
syst.add_def ("RpS=(2*frq^2/N^2-mu^2)*(ph1^2+ph2^2)");

// KG equations
syst.add_def ("KG1=N^2*D_i_N*D^i_ph1/Psi^4-N^3*D_i_D^i_ph1/Psi^4
+2*N^3*D_i_ph1*D^i_Psi/Psi^5+2*LP1-N^3*mu*mu*ph1" );
syst.add_def ("KG2=N^2*D_i_N*D^i_ph2/Psi^4+N^3*D_i_D^i_ph2/Psi^4
+2*N^3*D_i_ph2*D^i_Psi/Psi^5+2*LP2-N^3*mu*mu*ph2" );

// Field equations
for (int d=1 ; d<ndom ; d++) {
    if ((d!=2) && (d!=3)) {
        syst.add_def (d,"eqN=D_iD^iN+2*D_iPsi*D^iN/Psi-N*Psi^4*A_ij*A^ij");
        syst.add_def (d,"eqP=D_iD^iPsi+Psi^5*A_ij*A^ij/8");
//      syst.add_def (d,"eqB^i = D_j A^ij + 10 * A^ij * D_j Psi / Psi");
    }
    else {
        syst.add_def (d, "eqN=D_iD^iN+2*D_iPsi*D^iN/Psi-N*Psi^4");
        syst.add_def (d, "eqP=D_iD^iPsi+Psi^5*A_ij*A^ij/8+2*pi");
//      syst.add_def (d, "eqB^i = D_j A^ij + 10 * A^ij * D_j Psi / Psi- 8 *");
    }
}

// inner BC metric
space.add_inner_bc(syst, "N=t");
//   space.add_inner_bc(syst, "bet^i = t / Psi^2 * nn^i + ome * m^i * r");
space.add_inner_bc(syst, "4*nn^i*D_iPsi/Psi+D_i nn^i+Psi^2*A_ij*nn^j");

```

```

// outer BC metric
space.add_outer_bc(syst , "N=1");
space.add_outer_bc(syst , "Psi=1");
//   space.add_outer_bc(syst , "bet^i=0");

// Einstein Equations
space.add_eq(syst , "eqN_=_0" , "N" , "dn(N)" ) ;
space.add_eq(syst , "eqP_=_0" , "Psi" , "dn(Psi)" ) ;
//   space.add_eq(syst , "eqB^i= 0" , "bet^i" , "dn(bet^i)" ) ;

// For the fields :
// O near the horizon
syst.add_eq_full (1 , "ph1=0" ) ;
syst.add_eq_full (1 , "ph2=0" ) ;

// Inner BC cst value
syst.add_eq_bc (2 , INNER_BC , "ph1_=_p1" ) ;
syst.add_eq_bc (2 , INNER_BC , "ph2_=_p2" ) ;

//   for (int d=2 ; d<=3 ; d++) {
syst.add_eq_inside (d , "KG1=0" ) ;
syst.add_eq_inside (d , "KG2=0" ) ;

// Matching
if (d!=3) {
    syst.add_eq_matching(2 , OUTER_BC , "ph1" ) ;
    syst.add_eq_matching(2 , OUTER_BC , "dn(ph1)" ) ;
    syst.add_eq_matching(2 , OUTER_BC , "ph2" ) ;
    syst.add_eq_matching(2 , OUTER_BC , "dn(ph2)" ) ;
}
}

//Outer BC
syst.add_eq_bc (3 , OUTER_BC , "ph1_=_0." ) ;// 3 ->2
syst.add_eq_bc (3 , OUTER_BC , "ph2_=_0." ) ;

// 0 elsewhere
for (int d=4 ; d<ndom ; d++) { // 4 -> 3
    syst.add_eq_full (d , "ph1=0" ) ;
    syst.add_eq_full (d , "ph2=0" ) ;
}

if (rank==0){
Array<double> errors (syst.check_equations()) ;

```



```

for (int i=0 ; i<errors.get_size(0) ; i++)
    if (errors(i)>1)
        cout << i << "_" << errors(i) << endl ;
}

// Newton-Raphson
double conv;
bool endloop = false;
int ite = 1;
if (rank == 0)
    cout << "Solve_all_fields_simultaneously" << endl ;
while (!endloop) {
    endloop = syst.do_newton(1e-8, conv);
    cout << "Solve_all_fields_simultaneously" << endl ;
while (!endloop) {
    endloop = syst.do_newton(1e-8, conv);
    if (rank == 0) {
        cout << "Newton_iteration_" << ite << "_" << conv << endl;
        ite++;
    }
}

// Computation adm mass after backreaction :
Val_domain integ_adm (conf(ndom-1).der_r()) ;
double adm = -space.get_domain(ndom-1)->integ(integ_adm, OUTER_BC)/2/M_PI ;
if (rank==0) {
    cout << "ADM_mass_before_backreaction:_" << adm_init << endl ;
    cout << "ADM_mass_after_backreaction:_" << adm << endl ;
}

// Output final results
if (rank==0) {
    char name[100];
    sprintf(name, "BR_1s_brcheck_%d_%d%.0f_%.1f%.0f%.0f%.1f%.2f.dat", r2_re
    FILE *fich = fopen(name, "w");
    space.save(fich);
    fwrite_be(&r2_res, sizeof(int), 1, fich);
    fwrite_be(&r3_res, sizeof(int), 1, fich);
    fwrite_be(&r0, sizeof(double), 1, fich);
    fwrite_be(&r1, sizeof(double), 1, fich);
    fwrite_be(&r2, sizeof(double), 1, fich);
    fwrite_be(&r3, sizeof(double), 1, fich);
    fwrite_be(&t, sizeof(double), 1, fich);
    fwrite_be(&ome, sizeof(double), 1, fich);
    fwrite_be(&freq, sizeof(double), 1, fich);
    fwrite_be(&mu, sizeof(double), 1, fich);
}

```

```
        conf.save(fich);
        lapse.save(fich);
        shift.save(fich);
        field1.save(fich);
        field2.save(fich);
        fclose(fich) ;
    }
    MPI_Finalize() ;
}
```

## Appendix D

## Appendix D

The level mixing more well-defined in terms of (1.26)

$$\langle \psi_i | V_* | \psi_j \rangle = -M_* \mu \sum_{l_* \geq 2} \sum_{|m_*| \leq l_*} \frac{4\pi}{2l_* + 1} \frac{Y_{l_* m_*}^*(\Theta_*, \Phi_*)}{R_*^{l_*+1}} \times I_r \times I_\Omega \quad (\text{D.1})$$

where

$$I_r \equiv \int_0^\infty dr r^{2+l_*} R_{n_j l_j}(r) R_{n_i l_i}(r) \quad (\text{D.2})$$

$$I_\Omega \equiv \int_0^\infty d\Omega r^{2+l_*} Y_{n_j l_j}^*(\theta, \phi) Y_{n_i l_i}^*(\theta, \phi). \quad (\text{D.3})$$

The angular integral  $\Omega$  lead to the following selection rules<sup>1</sup>:

1.  $-m_j + m_i + m_* = 0$ ,
2.  $|l_j - l_i| \leq l_* \leq l_i + l_j$ ,
3.  $l_i + l_j + l_* = 2p$ , for  $p \in \mathbb{Z}$ .

Recall from before that the fastest growing mode is  $|211\rangle$  i.e.  $l_g = m_g = 1$  whereas the fastest decaying mode is  $|100\rangle$  i.e.  $l_d = m_d = 0$ . For the latter case, the above selection rules would imply that  $l_* = m_* = 0$ . This corresponds to a dipole coupling which is not present in 1.27. For the quadrupole coupling on the other hand, the selection rules imply that for  $l_g = m_g = 1$ , the fastest decaying modes are  $l_d = 1, m_d = -1$  and  $l_d = 1, m_d = 0$ .

### Resonances and level mixing

As has been shown in [11], when considering orbits along the equatorial plane, the  $|201\rangle$  mode decouples and the problem reduces to the dynamics of a two-state system which can be solved exactly. In this case the growing mode  $|\psi_g\rangle = |211\rangle$  couples to the decaying mode,  $|\psi_d\rangle = |21-1\rangle$ . In fact, the occupation density of the decaying mode can be expressed as,

$$|c_d^{(h)}(t)|^2 = \left[ 1 - \left( \frac{\epsilon_h \mp \Omega}{\Delta_R^{(h)}} \right)^2 \right] \sin^2 \left[ \int_{t_0}^t dt' \Delta_R^{(h)}(t') \right], \quad (\text{D.4})$$

<sup>1</sup>Because the selection rules are obtained solely from the angular dependence of the wavefunctions they apply to both the fundamental mode,  $n = 2$ , as well as the overtones,  $n \geq 3$ .

where  $\epsilon_h$  is the *hyperfine splitting* and  $\Delta_R^{(h)}$  is known as the *Rabi frequency*, analogous to the quantum mechanical problem. The Rabi frequency is not constant during the inspiral, as is evident by the integral inclusion, and as the name suggests it controls the frequency of oscillations between the growing and decaying modes.

We may now define an important phenomenon known as *Hyperfine resonance*. Whenever the orbital frequency  $\Omega$  matches the hyperfine splitting  $\epsilon_h$  the system will experience a resonance and start oscillating between the decaying and growing modes. Because  $\epsilon_h > 0$  the resonance can only occur for co-rotating orbits and at a certain binary separation,  $R_{res}^{(h)} = 144^{(1/3)}\alpha^{-4}(1+q)^{(1/3)}\tilde{a}^{-2/3}r_g^2$ .

Yet another important phenomenon in a binary system is *Bohr mixing*. To this end we must consider that the growing mode  $|211\rangle$  may also mix with the decaying modes  $|n10\rangle$  and  $|n1-1\rangle$ , for  $n \geq 3$ . Similar to the hyperfine case, the system reduces to a mixing between two modes, the growing mode  $|211\rangle$  and the decaying one,  $|31-1\rangle$ . One ends up with a similar occupation density,

$$|c_d^{(b)}(t)|^2 = \left[ 1 - \left( \frac{\epsilon_b \mp \Omega}{\Delta_R^{(b)}} \right)^2 \right] \sin^2 \left[ \int_{t_0}^t dt' \Delta_R^{(b)}(t') \right]. \quad (\text{D.5})$$

As for the hyperfine case, the system will undergo a resonance once the orbital frequency matches the energy split between the overtones. As one would expect, this resonance is referred to as *Bohr resonance*. Unlike the hyperfine resonance, in which  $\omega_{21-1} < \omega_{211}$ , we have for the Bohr resonance that  $\omega_{31-1} > \omega_{211}$ . Which implies that Bohr resonances occur for counter-rotating orbits with a binary separation of

$$R_{res}^b = \left( \frac{144}{5} \right)^{2/3} \alpha^{-2}(1+q)^{(1/3)}r_g. \quad (\text{D.6})$$

Note that  $R_{res}^b \propto \alpha^{-2}$  whereas  $R_{res}^h \propto \alpha^{-4}$ , implying that for  $\alpha \ll 1$ , Bohr resonance occur at a smaller separation than hyperfine resonance [11].

---

<sup>2</sup> $q = m_1/m_2 \geq 1$  is the mass ratio of the two black holes in the binary.

## Appendix E

## Appendix E

In this appendix I present the results of the MAE for the lapse and conformal factor since they were too big to add in Chapter 4. Furthermore, I compare our numerical data to the analytical expressions derived in [38].

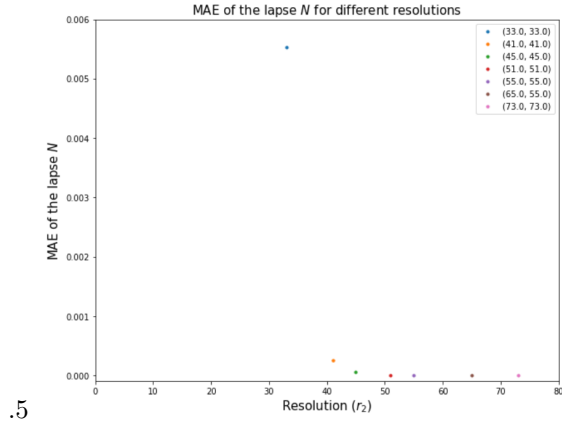


Figure E.1: The MAE of the lapse function  $N$  for various resolutions of  $r_2$ .

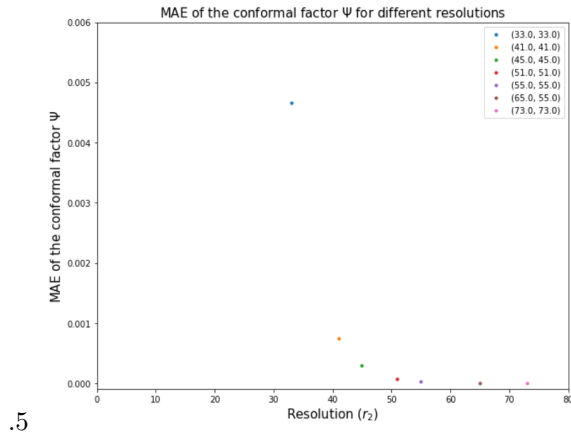


Figure E.2: The MAE of the conformal factor  $\Psi$  for various resolutions of  $r_2$

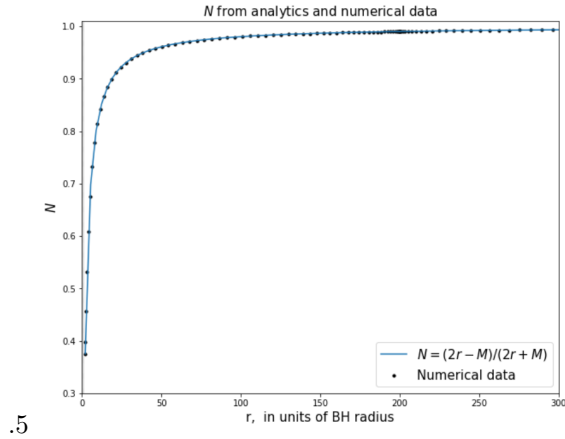


Figure E.3: The comparison of analytics and numerical data for the conformal factor  $\Psi$  for our resolution  $\{65, 55\}$ .

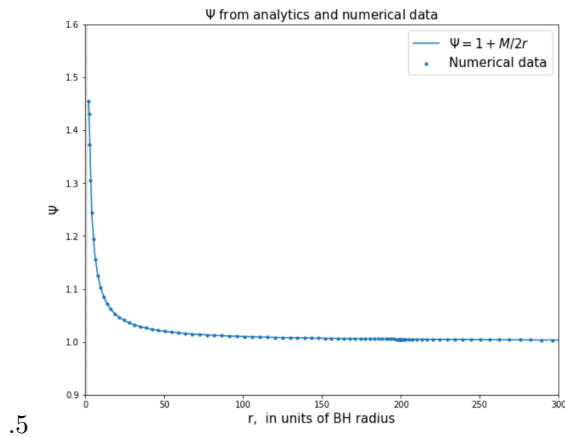


Figure E.4: The comparison of analytics and numerical data for the conformal factor  $\Psi$  for our resolution  $\{65, 55\}$ .

# Bibliography

- [1] Nikita Blinov, Matthew J. Dolan, Patrick Draper, and Jonathan Kozaczu *Dark Matter Targets for Axion-like Particle Searches*. <https://arxiv.org/pdf/1905.06952.pdf>
- [2] R. Essig, J. A. Jaros, W. Wester, et. al. *Dark Sectors and New, Light, Weakly-Coupled Particles*. <https://arxiv.org/pdf/1311.0029.pdf>
- [3] Asimina Arvanitaki and Sergei Dubovsky *Exploring the String Axiverse with Precision Black Hole Physics*. (2010) <https://arxiv.org/pdf/1004.3558.pdf>
- [4] Mehmet Demirtas, Cody Long, Liam McAllister, and Mike Stillman *The Kreuzer-Skarke Axiverse* <https://arxiv.org/pdf/1808.01282.pdf>
- [5] Peter Svrcek and Edward Witten *Axions In String Theory* <https://arxiv.org/pdf/hep-th/0605206.pdf>
- [6] The LIGO Scientific Collaboration, the Virgo Collaboration *Observation of Gravitational Waves from a Binary Black Hole Merger* <https://arxiv.org/abs/1602.03837>
- [7] R. Abbott et al *Observation of Gravitational Waves from Two Neutron Star–Black Hole Coalescences* <https://iopscience.iop.org/article/10.3847/2041-8213/ac082e>
- [8] LIGO Caltech website <https://www.ligo.caltech.edu/page/gw-sources>  
<https://www.ligo.caltech.edu/page/gw-sources>
- [9] C. Palomba et al *Direct constraints on ultra-light boson mass from searches for continuous gravitational waves* <https://arxiv.org/pdf/1909.08854.pdf>
- [10] C. A. Baker et al., Phys. Rev. Lett. 97, 131801 (2006) [arXiv:hep-ex/0602020].
- [11] D. Baumann, H.S. Chia, R. A. Porto *Probing Ultralight Bosons with Binary Black Holes* (2018).
- [12] C. Amsler et al. [Particle Data Group], Phys. Lett. B 667, 1 (2008)
- [13] Mehmet Demirtas, Cody Long, Liam McAllister, and Mike Stillman *The Kreuzer-Skarke Axiverse* <https://arxiv.org/pdf/1808.01282.pdf>
- [14] W. Press and S. Teukolsky “*Floating Orbits, Superradiant Scattering and the Black Hole Bomb*” <https://www.nature.com/articles/238211a0>
- [15] D. Baumann, H.S. Chia, R. A. Porto *The Spectra of Gravitational Atoms* (2019).

- [16] Robert M. Wald. *General Relativity*. The University of Chicago press, 1984.
- [17] Sean M. Carroll. *An Introduction to General Relativity SPACETIME and GEOMETRY*. Cambridge University Press, 2019
- [18] FuJun Wang, YuanXing Gui, ChunRui Ma *Isotropic coordinates for Schwarzschild black hole radiation*. Cambridge University Press, 2019
- [19] Domenico Giulini, *Dynamical and Hamiltonian formulation of General Relativity*. <http://philsci-archive.pitt.edu/11446/1/Giulini.pdf> Institute for Theoretical Physics, Leibniz University Hannover.
- [20] Ericourgoulhon and Jos e Luis Jaramillo *A 3+1 perspective on null hypersurfaces and isolated horizons*. <https://arxiv.org/pdf/gr-qc/0503113.pdf> Laboratoire de l'Univers et de ses Th ories, UMR 8102 du C.N.R.S., Observatoire de Paris, F-92195 Meudon Cedex, France
- [21] Masha Baryakhtar et. al. *Black hole superradiance of self-interacting scalar fields*. <https://arxiv.org/pdf/2011.11646.pdf> Center for Cosmology and Particle Physics, Department of Physics, New York University.
- [22] Chen Yuan, Richard Brito, Vitor Cardoso *Probing ultralight dark matter with future ground-based gravitational-wave detectors* . <https://arxiv.org/pdf/2106.00021.pdf>
- [23] Leo Tsukada, Richard Brito, William E. East, and Nils Siemonsen *Modeling and searching for a stochastic gravitational-wave background from ultralight vector bosons*. <https://journals.aps.org/prd/abstract/10.1103/PhysRevD.103.083005>
- [24] Neil J. Cornish *What is a Lagrange Point?*. <https://solarsystem.nasa.gov/resources/754/what-is-a-lagrange-point/>
- [25] Ken K. Y. Ng, Maximiliano Isi, Carl-Johan Haster, Salvatore Vitale *Multiband gravitational-wave searches for ultralight bosons*. <https://arxiv.org/pdf/2007.12793.pdf>
- [26] Domenico Giulini *Dynamical and Hamiltonian formulation of General Relativity*
- [27] Ericourgoulhon. *3+1 formalism and bases of numerical relativity*. Laboratoire Univers et Th ories, UMR 8102 du C.N.R.S., Observatoire de Paris, Universit e Paris 7 F-92195 Meudon Cedex, France .
- [28] Domenico Giulini *Dynamical and Hamiltonian formulation of General Relativity* <http://philsci-archive.pitt.edu/11446/1/Giulini.pdf>
- [29] Carlos Palenzuela *Introduction to Numerical Relativity* (2020) <https://arxiv.org/pdf/2008.12931.pdf>
- [30] Baumgarte, T. W. and Shapiro, S. L. (2010) *Numerical relativity : solving einstein's equations on the computer*. Cambridge, UK: Cambridge University Press. Available at: ANGE-SAKNAD-URL (Accessed: 2021).
- [31] Jos e Luis Jaramillo and Ericourgoulhon. *Mass and Angular Momentum in General Relativity* (2010).



- [32] Albert Einstein. *Zur Elektrodynamik bewegter Körper*. (German) [*On the electrodynamics of moving bodies*]. *Annalen der Physik*, 322(10):891–921, 1905.
- [33] R. Brito, S. Ghosh, E. Barausse, E. Berti, V. Cardoso, I. Dvorkin, A. Klein, and P. Pani, *Stochastic and resolvable gravitational waves from ultralight bosons*, *Phys. Rev. Lett.* 119, 131101 (2017), arXiv:1706.05097 [gr-qc].
- [34] R. Brito, V. Cardoso, and P. Pani, *Superradiance* *Lect. Notes Phys.* 906 (2015) 1, arXiv:1501.06570 [gr-qc].
- [35] Eric Gourgoulhon. “*Simple equations for general relativistic hydrodynamics in spherical symmetry applied to neutron star collapse*.” *Astron. Astrophys.*, 252, 651–663, (1991)
- [36] G. Darmon. *Les ´equations de la gravitation einsteinienne*, M´emorial des Sciences Math´ematiques 25, Gauthier-Villars, Paris (1927).
- [37] Carlos Palenzuela, *Introduction to Numerical Relativity*. *Front. Astron. Space Sci.*, 10 September 2020
- [38] Christoffel Doorman, *Axion Dark Matter around Black Holes*. FNWI MSc Physics and Astronomy, University of Amsterdam (2020).
- [39] Gilbert Strang *Introduction to Linear Algebra, Fifth Edition*, (2016)
- [40] William E. East and Frans Pretorius *Superradiant Instability and Backreaction of Massive Vector Fields around Kerr Black Holes* (2017)
- [41] A. Lichnerowicz. *L’integration des equations de la gravitation relativiste et le probleme des n corps*. In: *Journal de Mathematiques Pures et Appliquees* 23 (1944), pp. 37-62.
- [42] R. Brito, V. Cardoso, and P. Pani, “*Superradiance*,” *Lect. Notes Phys.* 906 (2015) 1, arXiv:1501.06570 [gr-qc].